# Modelling and Simulation of Marine Cables with Dynamic Winch and Sheave Contact

by

Cassidy Westin

A thesis submitted to the Faculty of Graduate and Postdoctoral Affairs in partial fulfillment of the requirements for the degree of

Master of Applied Science
in
Mechanical Engineering

Department of Mechanical and Aerospace Engineering
Carleton University
Ottawa, Ontario

# Abstract

Cable-sheave systems are commonly used on marine vessels for lifting and towing applications. As a result of the motion of the vessel, the cable can detach from the surface of the sheave. This thesis presents a simulation of a towed cable system which includes the interaction of the cable with the sheave surface in order to examine variations in the contact between the cable and the sheave. A three-dimensional description of the sheave geometry is implemented in order to accurately model the contact forces as the vessel undergoes six degree-of-freedom motion. To assess the performance of the model, the simulated cable behavior is compared to small scale experimental measurements. Experiments were carried out with a pulley supporting a cable and a swinging load. Good agreement with the measured cable tension and wrap angle of the cable around the pulley was shown. Using existing experimental data, the motion of a small towbody in a flume tank was compared with the simulated motion. The simulation demonstrated good agreement with the experimental towbody motion, predicting the volume of the enclosing ellipsoid to within 27%. Finally, a case study was performed to demonstrate the usage of the simulation to examine variations in cable tension and contact forces for a full scale system. The method demonstrated can be used in future studies to examine cable detachment behavior.

# Contents

# List of Tables

# List of Figures

# Nomenclature

| | |
|---|---|
| $A$ | Cable cross-sectional area ($\mathrm{m}^2$) |
| $a_1, a_2$ | Constraint stabilization constants |
| $\mathbf{B}$ | Embedding matrix |
| $\mathbf{C}$ | Damping matrix (Ns) |
| $\mathbf{C}_{D,b}$ | Vector of towbody drag coefficients along coordinate axes |
| $\mathbf{C}_{m,b}$ | Vector of towbody inertia coefficients along coordinate axes |
| $c$ | Damping coefficient (Ns) |
| $C_m$ | Added mass coefficient |
| $C_D$ | Drag coefficient |
| $D$ | Contact damping coefficient (Ns/m) |
| $d$ | Cable diameter (m) |
| $E$ | Young's modulus (Pa) |
| $\mathbf{f}$ | Distributed force vector (N/m) |
| $\mathbf{f}_B$ | Buoyancy force per unit length (N/m) |
| $\mathbf{f}_D$ | Drag force per unit length (N/m) |
| $\mathbf{f}_H$ | Hydrodynamic force per unit length (N/m) |
| $\mathbf{f}_I$ | Inertia force per unit length (N/m) |
| $\mathbf{f}_N$ | Normal contact force per unit length (N/m) |
| $f_n$ | Normal loading function |
| $f_t$ | Tangential loading function |
| $\mathbf{F}_b$ | Net force acting on towbody (N) |
| $\mathbf{F}_{b,D}$ | Drag force acting on towbody (N) |
| $\mathbf{F}_{b,g}$ | Gravitational and buoyancy force acting on towbody (N) |
| $\mathbf{F}_{b,I}$ | Inertia force acting on towbody (N) |
| $\mathbf{F}_{b,m}$ | Added mass and d'Alembert force acting on towbody (N) |

| | |
|---|---|
| $g$ | Gravitaional acceleration (m/s$^2$) |
| $h_g$ | Groove depth (m) |
| $\mathbf{I}$ | Identity matrix |
| $I$ | Second moment of area (m$^4$) |
| $K$ | Kinetic Energy (J) |
| $k_1$ | Winch proportional gain |
| $k_2$ | Winch derivative gain |
| $k_N$ | Contact stiffness constant (N/m) |
| $L$ | Unstretched element length (m) |
| $L_S$ | Sheave algorithm cable extension setpoint (m) |
| $L_W$ | Waterline algorithm cable extension setpoint (m) |
| $L_{nom}$ | Nominal cable length from top of sheave (m) |
| $\mathbf{M}$ | Mass matrix (kg) |
| $\mathbf{M}_b$ | Mass matrix of towed body (kg) |
| $\mathbf{M}_a$ | Added mass matrix (kg) |
| $m_b$ | Mass of towed body (kg) |
| $\mathbf{n}$ | Contact surface normal vector |
| $N_E$ | Number of elements |
| $N_I$ | Number of integration points |
| $p$ | Arc parameter (m) |
| $\mathbf{Q}$ | Generalized force (N) |
| $\mathbf{q}$ | Generalized coordinate vector |
| $\mathbf{Q}_c$ | Generalized constraint force (N) |
| $\mathbf{Q}_{\text{ext}}$ | Generalized external force (N) |
| $\mathbf{Q}_{\text{int}}$ | Generalized internal force (N) |
| $\mathbf{Q}_a$ | Generalized added mass force (N) |
| $\mathbf{Q}_b$ | Generalized towbody force (N) |

| | |
|---|---|
| $\mathbf{Q}_g$ | Generalized gravitational force (N) |
| $\mathbf{Q}_H$ | Generalized hydrodynamic force (N) |
| $\mathbf{Q}_l$ | Generalized longitudinal elastic force (N) |
| $\mathbf{Q}_N$ | Generalized contact force (N) |
| $\mathbf{Q}_t$ | Generalized transverse elastic force (N) |
| $\mathbf{r}$ | Absolute position vector (m) |
| $\mathbf{R}_B^I$ | Rotation matrix between ship body frame and inertial frame |
| $\mathbf{R}_x$ | Rotation matrix about $x$ axis |
| $\mathbf{R}_y$ | Rotation matrix about $y$ axis |
| $\mathbf{R}_z$ | Rotation matrix about $z$ axis |
| $R$ | Rayleigh dissipation function (J/s) |
| $Re$ | Reynold's number |
| $\mathbf{S}$ | Shape function matrix |
| $\mathbf{s}$ | Position vector in ship body frame (m) |
| $\mathbf{s}_s$ | Position vector in sheave centroid in ship body frame (m) |
| $\mathbf{s}_w$ | Position vector of winch centroid in ship body frame (m) |
| $s$ | Arc length (m) |
| $T$ | Tension (N) |
| $t$ | Time (s) |
| $\mathbf{u}_N$ | Surface normal vector |
| $\mathbf{u}_t$ | Tangent vector along cable centerline |
| $U_l$ | Longitudinal strain energy (J) |
| $U_t$ | Transverse strain energy (J) |
| $\mathbf{V}$ | Cable velocity vector relative to flow (m/s) |
| $\mathbf{V}_f$ | Flow velocity vector (m/s) |
| $\mathbf{V}_{f,n}$ | Component of flow velocity vector normal to cable (m/s) |
| $\mathbf{V}_{f,n}$ | Component of flow velocity vector tangential to cable (m/s) |

| | |
|---|---|
| $\mathbf{V}_n$ | Component of relative flow velocity vector normal to cable (m/s) |
| $\mathbf{V}_t$ | Component of relative flow velocity vector tangential to cable (m/s) |
| $V$ | Volume of submerged body (m$^3$) |
| $X, Y, Z$ | Body-fixed coordinates (m) |
| $x, y, z$ | Cartesian coordinates (m) |
| $\mathbf{\Phi}$ | Kinematic constraint equation |
| $\alpha$ | Yaw (rad) |
| $\beta$ | Pitch (rad) |
| $\delta$ | Contact penetration (m) |
| $\eta$ | Angle of incidence between flow and cable (rad) |
| $\gamma$ | Roll (rad) |
| $\kappa$ | Geometric curvature |
| $\mu$ | Fluid viscosity (Pa$\cdot s$) |
| $\phi$ | Winch rotation (rad) |
| $\phi_{nom}$ | Nominal winch rotation (rad) |
| $\phi_{SP}$ | Winch rotation set point (rad) |
| $\rho$ | Cable density (kg/m$^2$) |
| $\rho_f$ | Fluid density (kg/m$^3$) |
| $\theta_g$ | Groove throat angle (rad) |
| $\varepsilon$ | Longitudinal strain |
| $\xi$ | Arc parameter normalized by element length |
| $\mathbf{0}$ | Null matrix |

# 1 Introduction

Cable-pulley systems are commonly used in marine lifting applications and towing of sensor bodies for oceanographic research. Figure 1 illustrates a vessel towing a submerged sensor with a cable. A sheave is used to position the cable over the stern of the vessel, while a winch is used to pay-out and reel-in the cable. The cable experiences hydrodynamic drag, forming a catenary as shown in the figure, as well as forces transmitted through the sheave due to the motion of the ship. It is often desirable to keep the sensor body at a constant depth such that the collected data is not affected by the motion. Active Heave Compensation (AHC) may be used to decouple the motions of the ship and the sensor body and minimize the displacement of the sensor. Measurements of the ship motion determined from an Inertial Measurement Unit (IMU) can be used to determine the displacement of the sheave throughout the motion. The cable can then be reeled in or out to compensate for the disturbance. As a result of the ship motion and heave compensation, the cable can experience large variations in tension and is susceptible to loss of contact with the sheave surface if the tension becomes small. For many systems it may not be possible to constrain the cable in the sheave mechanically. It is thus desirable to model the cable dynamics and interactions with the sheave and winch surfaces in order to predict cable detachment and avoid unsafe conditions.

Various modelling methods have been used to simulate the dynamics of cables and most can be categorized as either Finite Difference Methods (FDM) or Finite Element Methods (FEM). In the Finite Difference Method, the cable is treated as continuous and the governing equations of the system are then approximated using difference equations. The governing equations, however, tend to be problem specific and the incorporation of nonlinear boundary conditions can be complex [1]. In the Finite Element Method the cable is first divided into a number of discrete elements, then

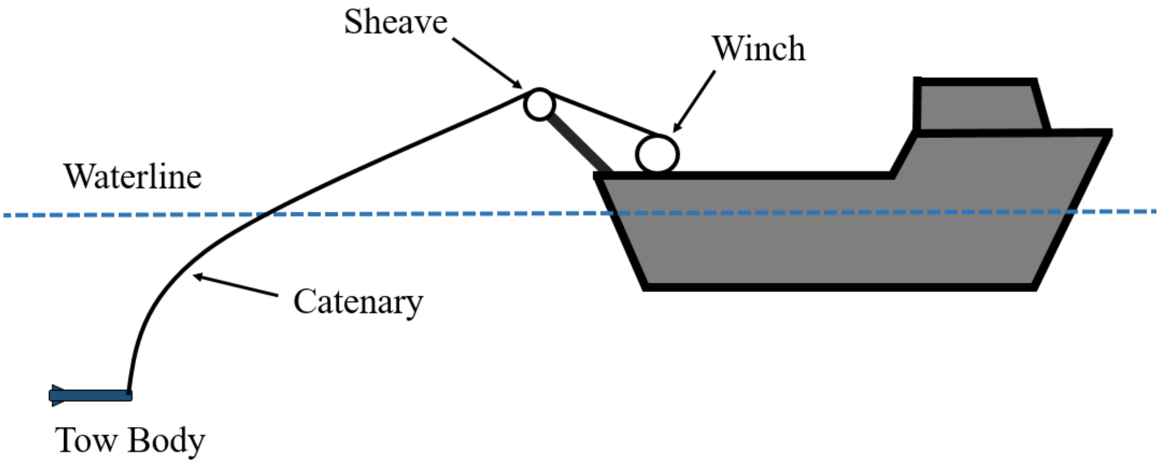

**Figure 1:** Diagram of ship and towed cable

each element is treated as one body in a a multibody system. Finite Element Methods are much more versatile than Finite Difference Methods and nonlinear boundary conditions and external loads can be applied easily [1].

Figure 2 illustrates the various modelling methods. Linear finite element models utilize straight elastic elements elements shown as dotted lines to connect discrete particles or lumped masses shown as black circles, while finite segment models consist of rigid elements connected by spherical joints. These models generally neglect the bending stiffness of the cable, with the exception of finite segment models with torsional springs at the joints [2]. Nonlinear methods utilize curved elements with the advantage of inherent bending stiffness and can be constrained such that the slope is continuous along the length of the cable. The continuous definition of the cable profile allows for external forces to be distributed along the length of the element, rather than concentrated at the nodes or centroids as with the lumped-mass and finite segment formulations, respectively. For systems with highly dynamic motion and slack cables, the effects of the bending stiffness become prominent and nonlinear curved-element formulations demonstrate better accuracy [3].

Models of submerged cables using finite elements typically use a revolute joint

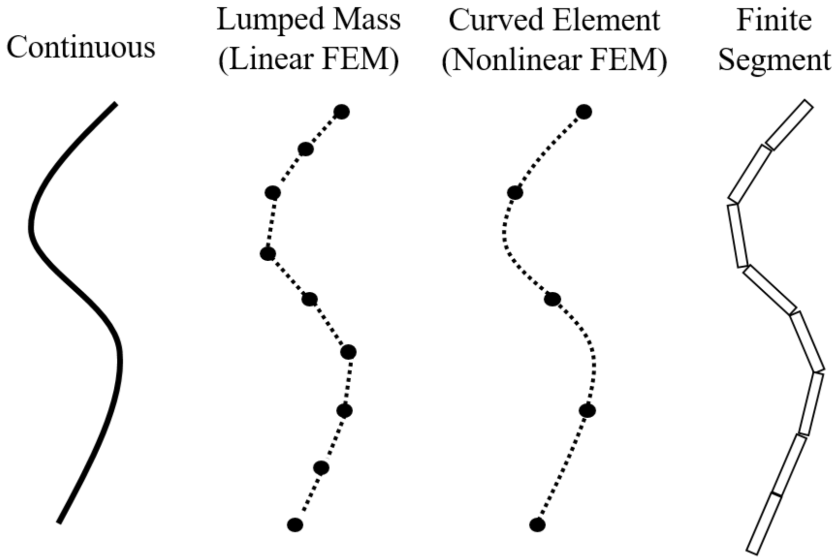

**Figure 2:** Illustration of cable modelling methods

to model the attachment of the cable to the ship. A model of a submerged cable that includes the interaction of the cable with the winch and sheave has not been found in the literature. However, a number of systems consisting of a cable with surface contact have been examined including belt-drives [4, 5], catenary-pantograph interactions [6] and loaded cable-pulley systems [7–9]. These studies usually only consider static loads or simple, planar cable motions. Also, the cable motion in these systems is often purely reciprocal and the area of contact between the cable and the surface remains constant. A small number of studies have examined cable-pulley interactions with dynamic contact [9, 10].

There are two main formulations that are used to model the normal contact forces between a flexible body and a rigid surface, Lagrange multiplier methods and penalty methods [11]. Lagrange multiplier methods use a discrete set of contact points defined on each body. The relative positions of matching points on the two bodies are governed by a kinematic constraint and the contact force is equal to the force required to satisfy the constraint exactly. Alternately, contact penalty methods allow the surfaces of the bodies to intersect. The normal contact force is then given as a function of the relative “penetration”. The contact penalty method is convenient for problems involving cable pulley systems as a continuous contact distribution can be described. Additionally, unilateral contact, where the contact force opposes penetration of the bodies but not separation, has a simple implementation using the penalty method.

Nonlinear finite element models are prevalent for modeling cable-pulley systems. The continuous nature of curved element formulations is advantageous, as the contact forces can be defined as continuous functions of the cable position and velocity. Thus, only a small number of elements are required to accurately model the surface interaction. The Absolute Nodal Coordinate Formulation (ANCF) is common in the current literature for modeling both submerged cables [12, 13] and cable-pulley interactions [7–9].

A model of a towed cable system which includes both the dynamics of the submerged cable and towbody and the normal contact between the cable and the sheave could be used to examine dynamic contact behavior and cable detachment during towing operations. *The first objective of this thesis is to develop a three-dimensional finite element model of a flexible cable with winch and sheave surface interactions to simulate the cable dynamics of a towed-body system with active heave compensation.* The nonlinear ANCF approach will be used, in order to accurately model both the contact force distribution imparted on the cable by the sheave and the behavior of the cable for low tension conditions. Both the sheave and winch interactions are to be modeled using a contact penalty formulation. The resulting model will be capable of exhibiting detachment of the cable from the sheave surface.

In previous literature, experimental validation of cable-pulley systems is limited to simple cable motions or focused solely on the sliding contact behavior as with belt drives and catenary pantograph models. Validation of the normal contact behavior and cable tension for dynamic excitations is sparse. *The second objective of this thesis* *is to assess the performance of the model by comparing the simulated cable behavior of small-scale systems with experimental measurements.* Fidelity of the model in simulating the towbody motion, cable tension and the contact between the cable and sheave is important to predicting cable detachment during slack conditions. Small scale tests of a towed body system with excitation at the tow point and active heave compensation will be used to verify the accuracy of the simulated towed body motion. Additionally, experimental measurements of a cable-pulley system with a moving load will be used to quantify the accuracy of the simulated cable tension and wrap angle of the cable around the pulley.

*The final objective of this thesis is to demonstrate the capability of the simulation to exhibit variations in cable tension and contact between the cable and sheave during towing operations.* A case study of a full scale towed cable system will be performed using experimental ship motion data. The effect of active heave compensation on the cable tension and contact distribution will then be examined. In future work, the method developed can be used to examine cable detachment behavior.

The key contributions of the research shown in this thesis are:

1. The inclusion of winch and sheave contact in a model of a marine cable system.
2. A three-dimensional formulation of the contact forces between the cable and the sheave groove, which enables accurate modelling of the contact forces during six degree-of-freedom ship motion.
3. Experimental validation of the cable-sheave model for cases where the wrap angle of the cable around the sheave undergoes significant variation.
4. A method outlined to examine dynamic contact behavior during towing operations.

This thesis consists of six chapters. Chapter 2 contains a review of existing literature related to numerical modeling of cables, submerged cables and cable-pulley interactions. Chapter 3 describes the modelling and numerical simulation of the system. Chapter 4 presents validation of the model based on towed-body motion of a small-scale cable-winch system. In Chapter 5, a case study of a full scale system is shown to demonstrate the simulated cable behavior. Finally, the results and conclusions of this thesis are given in Chapter 6.

# 2 Background and Literature Review

## 2.1 Background

Heave compensation systems can be categorized as either passive or active [2]. Passive compensation utilizes a damping element in the towline or overboarding system to attenuate motion of the body, while active compensation systems are actuated based on measurements of the ship motion using an Inertial Measurement Unit (IMU). For a straight line tow, Calnan et al. [14] developed and examined a number "set-point algorithms" for a winch-based AHC system. The set point algorithm estimates the amount of cable required to be reeled in or out by the winch in order to maintain the depth of the towed body.

Figure 3 illustrate Calnan's *waterline* algorithm that aims to keep the same point on the cable located at the waterline for the duration of the motion. The desired cable extension $L_w$ is determined by estimating the change in the length of cable between the sheave and the waterline.

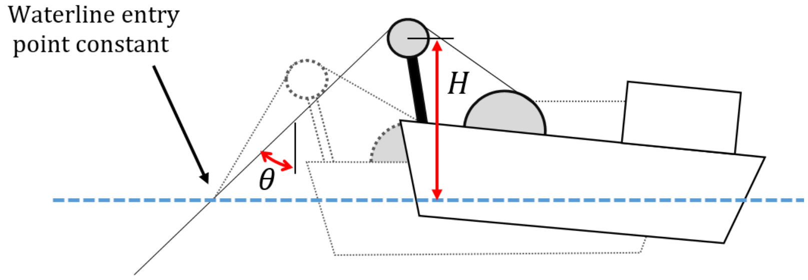

**Figure 3:** Waterline set point algorithm.

The waterline set-point $L_W$ is given by

$$L_W = \frac{H}{\cos(\theta)} - \frac{H_{nom}}{\cos(\theta_{nom})} \tag{1}$$

where $H_{nom}$ is the sheave height in steady conditions, $\theta$ is the angle of the cable as it leaves the sheave and $\theta_{nom}$ is the nominal value of $\theta$. If $\theta$ can be measured directly, then the algorithm is referred to as *rigorous*. If the sheave angle is not measured, then it is referred to as *simplified* and the sheave angle is assumed to have a constant value $\theta_{nom}$.

Figure 4 illustrates the *sheave* algorithm projects the displacement of the sheave from its nominal position onto the cable to determine the length of cable required to be reeled out $L_S$.

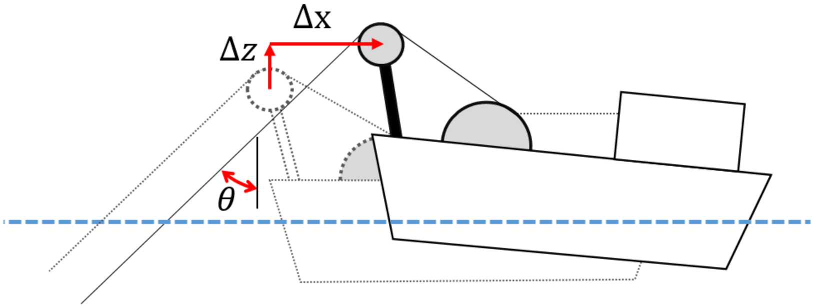

**Figure 4:** Sheave set point algorithm.

The sheave set point $L_S$ is computed by

$$L_S = (\Delta x)\sin(\theta) + (\Delta z)\cos(\theta) \tag{2}$$

where $\Delta x$ and $\Delta z$ are the displacements of the sheave along the $x$ and $z$ axes.

In order to examine the efficacy of these algorithms, Calnan implemented the algorithms both in small scale experiments performed in a flume tank and in a computer simulation. The small-scale experiment consisted of a cable, with a small-sphere as a towbody, and a winch. The winch could translate in three directions and the rotation about its axis was controlled by a feedback loop. The towbody motion was captured by two cameras and the position was converted into Cartesian coordinates. An ellipsoid fitting algorithm was then used to determine a volume which contained

95% of the towbody position data points. In the experiments, the Rigorous Sheave algorithms performed best with an 86% reduction in ellipsoid volume. The Simplified Sheave and Simplified Waterline algorithm performed similarly, however the Rigorous Waterline method was found to be unreliable [15].

The computer simulation consisted of rigid rods connected by universal joints with torsional springs to provide bending stiffness. The sheave and winch contact was not considered. Instead, a prismatic joint was translated to effect the reeling in and out of the cable. The simulator was validated using the experimental flume tank data. The simulator underestimated the ellipsoid volume by as much as 56 percent, but showed good agreement with the reduction in ellipsoid volume exhibited in the experiments. The model was also used to simulate a full scale system, wherein the Sheave algorithms demonstrated comparable performance to the small scale tests. The Simplified Waterline algorithm performed significantly worse at full scale than at small scale, while the Rigorous Waterline method was again unreliable. As the Waterline algorithms demonstrated poor performance and instability in the full-scale computer simulations, only the Sheave algorithms will be examined in this thesis.

The cable simulation developed by Calnan could potentially be improved by using an alternative method for modelling the cable, which better captures the dynamic cable behavior. In the next section, various methods for modelling flexible cables are compared. Additionally, inclusion of the contact between the cable and the sheave may improve the accuracy of the simulation. Section 2.4 discusses two methods for modelling contact between two bodies and their application to flexible cable models.

## 2.2 Cable Modelling Methods

Various methods of modelling flexible cables and ropes have been explored in the literature. In general, cable models can be categorized as either Finite Difference Methods (FDM) or Finite Element Methods (FEM). In the FDM, the cable is modelled as a continuum and the governing equations are derived as Partial Differential equations (PDEs). Finite difference approximations are used to spatially discretize the governing equations. When using a finite element method, the cable is *initially* discretized into a series of segments. Each element is treated as one body in a multibody system and the governing equations are formulated as coupled ordinary differential equations.

Ablow and Shechter [16] developed a three-dimensional model of a towed cable using the Finite Difference Method. To develop the governing equations they began by defining the balance of forces on a differential cable segment as

$$\frac{\partial}{\partial S}\mathbf{T} + \mathbf{W} + \mathbf{F} + \mathbf{B} = 0 \tag{3}$$

where S is the distance along the cable, $\mathbf{T}$ is the tension, $\mathbf{W}$ is the cable's self weight per unit length, $\mathbf{F}$ is the external hydrodynamic force per unit length and $\mathbf{B}$ is the d'Alembert force per unit length. Equation 3 can be written as three dynamic equations by taking the components in each of three body-fixed axes $\mathbf{t}, \mathbf{n}$ and $\mathbf{b}$, where $\mathbf{t}$ is tangent to the cable and $\mathbf{n}$ and $\mathbf{b}$ are normal to the cable. Figure 5 illustrates the body-fixed axes for a differential cable segment and the Cartesian coordinate frame with unit vectors $\mathbf{i}, \mathbf{j}$ and $\mathbf{k}$.

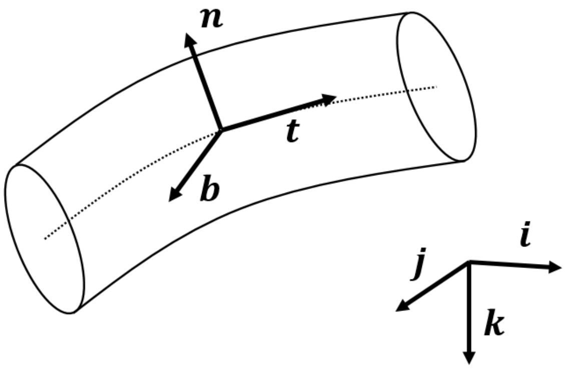

**Figure 5:** Differential cable segment with body-fixed coordinate axes and inertial coordinate axes.

The orientation of the body-fixed frame is defined relative to the inertial coordinate frame as

$$[\mathbf{t} \quad \mathbf{n} \quad \mathbf{b}] = [\mathbf{i} \quad \mathbf{j} \quad \mathbf{k}]\, \mathbf{R}_z(-\theta)\mathbf{R}_x(-\psi)\mathbf{R}_z(\phi) \tag{4}$$

where $\theta, \phi$ and $\psi$ are Euler angles and $\mathbf{R}_x$ and $\mathbf{R}_z$ are rotation matrices about the $x$ and $z$ axes, respectively. The form of the rotation matrices will be shown in Section 3.1.

Additionally, three compatibility equations which relate the cable velocities to the strain $\varepsilon$ and the rotational rates $\dot{\phi}, \dot{\psi}$ and $\dot{\theta}$ were derived by taking the components of the equation

$$\frac{d}{dt}\left(\frac{\partial \mathbf{r}}{\partial S}\right) = \frac{\partial}{\partial S}\left(\frac{d\mathbf{r}}{dt}\right), \tag{5}$$

where $\mathbf{r}$ is the cable position, along each of the body fixed axes $\mathbf{t}, \mathbf{n}$ and $\mathbf{b}$. The state vector has seven components: the tension $T$, the tangential velocity component $V_t$, the normal velocity components $V_n$ and $V_b$, and the Euler angles $\theta, \phi$ and $\psi$. An additional condition is needed to fully define the body-fixed coordinate frame relative to the inertial frame, thus the Euler angle $\psi$ was given a constant value of $\pi/2$. Ablow and Schechter [16] note the system becomes singular at zero tension, however Triantafyllou and Howell [17] have shown that including the cable's bending stiffness in the governing equations, even if the stiffness is minimal, prevents the singularity.

Although FDM cable models are computationally efficient and demonstrate reasonable accuracy for towed-body simulations [16], they are less versatile than finite element methods and it can be difficult to include complex boundary conditions [1]. The inclusion of towed-body dynamics and sheave and winch contact dynamics may therefore be challenging. Finite Element Methods, on the other hand, are modular which simplifies the insertion of additional elements, such as towed bodies, depressors or faired cable sections [1]. Complex boundary conditions are also simple to implement using kinematic constraints. Finite Element Methods can be categorized by the type of element used. The lumped-mass method consists of concentrating the cable mass into a finite number of particles which are connected by massless, linear springs. Alternatively, finite segment methods consist of rigid links that are connected by kinematic joints [18].

The governing equations for finite element models have a general form of [19]

$$\mathbf{M}\ddot{\mathbf{q}} + \mathbf{C}\dot{\mathbf{q}} + \mathbf{P}(\mathbf{q}) = \mathbf{Q} \tag{6}$$

where $\mathbf{q}$ is the vector of generalized coordinates, $\mathbf{M}$ is the mass matrix, $\mathbf{C}$ is the damping matrix, $\mathbf{P}(\mathbf{q})$ represents a general nonlinear elastic force and $\mathbf{Q}$ is the vector of generalized external forces.

For lumped-mass models, the mass and external forces are concentrated at the nodes. In Driscoll and Nahon's model of a mooring cable [20], the mass concentrated at each node is equivalent to one-half of the mass of the adjacent segments. Similarly one half of the forces acting on the adjacent segments is concentrated at the nodes. The mass matrix, in this case, is diagonal which leads to very good computational efficiency over other methods, however this type of mass lumping neglects the rotational inertia of the element. In finite segment models, the mass and external loads are often concentrated at the center of gravity of the segment. Kamman and Huston [21] use the orientations of the cable segment as generalized coordinates, thus the rotational inertia of the segment and external torques can be included. In a later work, Kamman and Huston lump the mass at the joints in order to reduce the computational requirements of the model [22].

In both lumped mass and finite segment models, the bending stiffness can be incorporated. Buckham and Nahon [12] developed a three-dimensional model a slack ROV tether using a lumped approach and linear elastic elements. However, they note the inaccuracy of the model during low tension due to bending effects being neglected. The researchers developed a discrete definition of the internal bending forces at each node using the positions of the adjacent nodes to estimate the cable curvature. The model was validated for static bending loads and is shown to provide a good approximation of the flexural stiffness. In Calnan's finite segment model [2], the bending stiffness is approximated using rotational springs at the joints.

For deformable elements, the inertia and distributed external forces can be more accurately represented using "shape functions" [23]. The shape function $\mathbf{S}$ interpolates the position of an arbitrary point on the element $\mathbf{r}$ from the generalized coordinates $\mathbf{q}$ as

$$\mathbf{r}(p) = \mathbf{S}(p)\mathbf{q}, \tag{7}$$

where $p$ is a parameter representing the position of the point in material coordinates. The shape function can then be used to formulate the mass matrix using the variational or Lagrangian approach. Given the kinetic energy of the element $K$, defined as

$$K = \int_0^L \dot{\mathbf{r}}^T \mu \dot{\mathbf{r}} dp \tag{8}$$

where $\mu$ is the cable density per unit length, the mass matrix is given by the Hessian of $K$ [24]:

$$\mathbf{M} = \frac{\partial K}{\partial \dot{\mathbf{q}} \partial \dot{\mathbf{q}}} = \int_0^L \mathbf{S}^T \mu \mathbf{S} dp. \tag{9}$$

A common FEM formulation utilizing curved elements is known as the Absolute Nodal Coordinate Formulation (ANCF) [23]. The element is parameterized by the arc coordinate $p \in [0, L]$ and the shape is determined by a cubic Hermite spline; in other words, the path of the element $\mathbf{r}(p)$ is defined by the positions $\mathbf{r}$ and the slopes

$\mathbf{r}' = \partial\mathbf{r}/\partial p$ at each of the nodal endpoints. The generalized coordinate vector is thus

$$\mathbf{q} = \left[\mathbf{r}(0) \quad \mathbf{r}'(0) \quad \mathbf{r}(L) \quad \mathbf{r}'(L)\right]^T, \tag{10}$$

where $p = 0$ and $p = L$ represent the nodes at each end of the element. The cubic shape function is given by

$$\mathbf{S}(p) = \left[(1 - 3\xi^2 + 2\xi^3)\mathbf{I}_3 \quad (\xi - 2\xi^2 + \xi^3)\mathbf{I}_3 \quad (3\xi^2 - 2\xi^3)\mathbf{I}_3 \quad (\xi^2 - \xi^3)\mathbf{I}_3\right], \tag{11}$$

where $\mathbf{I}_3$ is a $3 \times 3$ identity matrix and $\xi = p/L$ is the parameter $p$ normalized by the unstretched length. The mass matrix $\mathbf{M}$ in Equation 9 can be written as a constant matrix:

$$\mathbf{M} = \frac{\mu L}{420}\begin{bmatrix} 156\mathbf{I}_3 & 22L\mathbf{I}_3 & 54\mathbf{I}_3 & -13L\mathbf{I}_3 \\ & 4L^2\mathbf{I}_3 & 13L\mathbf{I}_3 & -3L^2\mathbf{I}_3 \\ & & 156\mathbf{I}_3 & -22L\mathbf{I}_3 \\ sym. & & & 4L^2\mathbf{I}_3 \end{bmatrix}. \tag{12}$$

The off-diagonal terms in the above matrix represent the coupling between the nodes which results from the rotational inertia of the element.

Finite element methods can be further classified as linear or nonlinear formulations. The lumped-mass method, in general, is linear in that the elastic forces are linearly proportional to the nodal displacement. For problems where the bending or tensile deformations are large, the change in geometry is taken into account when formulating the elastic forces, thus giving rise to geometric nonlinearity. The nonlinear elastic forces can be formulated using standard continuum mechanics approaches such as the Euler-Bernoulli or Timoshenko beam theories [25].

In the definition of the ANCF shown above each node has one gradient vector

$\mathbf{r}_p$, which is a special case of the general ANCF method and is often referred to as the "gradient-deficient" ANCF [26]. The gradient-deficient formulation follows the Euler-Bernoulli beam theory and thus the cable cross-section is always perpendicular to the neutral axis. Shear and torsional deformations can by introduced by including additional gradient vectors at each node [27].

Figure 6 compares the gradient-deficient and shear-deformable elements. In the gradient-deficient case, the cross-section is always perpendicular to the cable-centerline. In the shear-deformable case, the parameter $q$ defines the position of a point on the element across the cross-section. The gradient vector $\mathbf{r}_q$ defines the orientation of the cable cross-section.

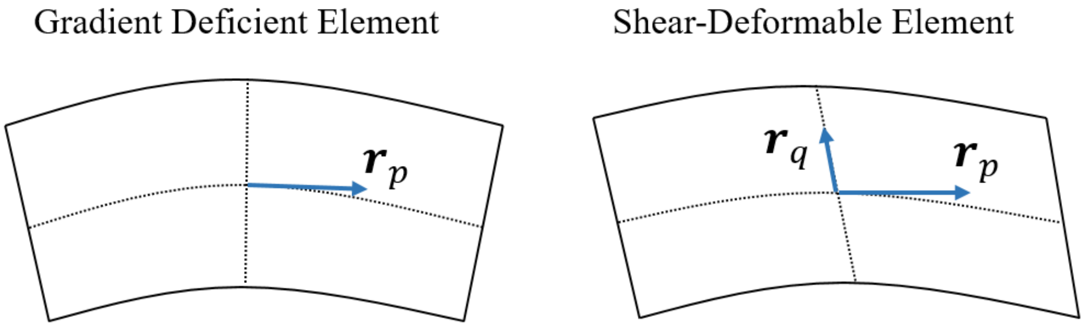

**Figure 6:** Comparison of gradient deficient and shear deformable cable elements.

In the current study, the cable is made of strands of steel wire. Since the strands can slide relative to one another, the shear-deformable method may be more applicable. However, as a result of the slenderness of the cable, the Euler-Bernoulli beam is likely a sufficient approximation [28] and has half of the required degrees of freedom as the fully-parameterized beam element [27]. Torsional deformations are not expected to be significant.

The ANCF method has several advantages over linear methods. The continuum-mechanics approach allows for simple and accurate definitions the cable elastic forces. Several models of the longitudinal and tangential elastic forces using the Absolute

Nodal Coordinate Formulation are shown by Berzeri and Shabana [29]. The importance of accurately modelling the bending stiffness will be discussed in the following sections. Furthermore, in the current study the hydrodynamic loads and contact forces are expected to vary significantly along the length of the cable and are discontinuous at the waterline and contact transitions. The curved elements can be constrained such that the cable has a smooth and continuous profile and the nonlinear external forces can be evaluated at any arbitrary point on the cable. The number of elements required to obtain an accurate solution is thus much smaller than with linear models, which is a significant advantage for modeling long submerged cables.

## 2.3 Submerged Cable Dynamics

In Calnan's computer simulation [2], the hydrodynamic forces acting on the cable follow the Morison equation. The Morison equation is frequently used to model the forces acting on a body in a normal, non-uniform flow, as it can efficiently predict the force acting on the body without numerical modeling of the flow field. It comprises three force components: drag, hydrodynamic mass and the Froude-Krylov force. For a non-stationary body in a flow normal to the body surface, the total hydrodynamic force is [30]

$$\mathbf{f}_H = \frac{1}{2}\rho_f C_D A_f |\mathbf{V}_f - \mathbf{V}_b|(\mathbf{V}_f - \mathbf{V}_b) + \rho_f C_m V(\dot{\mathbf{V}}_f - \dot{\mathbf{V}}_b) + \rho_f V \dot{\mathbf{V}}_f \tag{13}$$

where $\rho_f$ is the fluid density, $C_D$ is the normal drag coefficient, $C_m$ is the hydrodynamic mass coefficient, $\mathbf{V}_f$ is the flow velocity, $\mathbf{V}_b$ is the body velocity, $A_f$ is the frontal area of the body, and $V$ is the volume of the body. The first term in Equation 13 is the viscous drag force, the second term is the hydrodynamic added mass force and the third term is the Froude-Krylov force. The hydrodynamic mass force accounts for the inertia of the fluid in the immediate vicinity of the body [30]. When the body accelerates relative to the fluid it must also accelerate the surrounding fluid. Conversely, the Froude-Krylov force occurs as a result of the pressure-gradient created by the absolute acceleration of the fluid in the outer-flow region. In a steady-flow, the Froude-Krylov force becomes zero.

For a cylinder that is inclined to the flow, the Morison equation can be applied by replacing the velocity vectors in Equation 13 with their normal components [31]. Accordingly, it is often assumed that the drag coefficient $C_D$ is independent of the angle between the flow and the cylinder. This assumption is referred to as the "independence principle" [31]. Equation 13 can be written as

$$\mathbf{f}_{H,n} = \frac{1}{2}\rho_f C_{D,n} A_f |\mathbf{V}_n| \mathbf{V}_n + \rho_f C_m V \dot{\mathbf{V}}_n + \rho_f V \dot{\mathbf{V}}_n \tag{14}$$

where $C_{D,n}$ is the normal drag coefficient, $\mathbf{V}_n$ is the normal component of the relative velocity $\mathbf{V}_f - \mathbf{V}_b$ given by

$$\mathbf{V}_n = (\mathbf{V}_f - \mathbf{V}_b) - |\mathbf{V}_f - \mathbf{V}_b| \cos(\eta) \mathbf{u}_t, \tag{15}$$

where $\eta$ is the angle of attack between the relative flow vector and the cable centerline and $\mathbf{u}_t$ is the unit vector tangent to the cable centerline as shown in Figure 7.

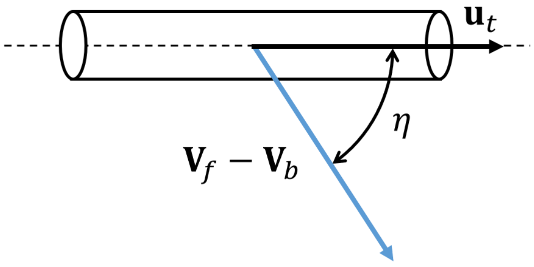

**Figure 7:** Flow velocity vector and angle of attack.

Additionally, it is common to consider the drag force acting tangential to the cylinder due to skin friction, which will be referred to as the tangential drag force.

Calnan defines the drag given as

$$\mathbf{f}_{H,t} = \frac{1}{2}\rho_f d C_{D,t} |\mathbf{V}_t| \mathbf{V}_t \tag{16}$$

where $C_{D,t}$ is the tangential drag coefficient and $\mathbf{V}_t$ is the tangential component of the relative velocity.

In Calnan's simulations, the flow vector is decomposed into the cable segment's body-fixed coordinate frame, where one axis is aligned with the cable longitudinal axis and the other axes are normal to the cable. The independence principal is applied and constant normal and tangential drag coefficients are assumed to be constant. Calnan expresses the cable's added mass as

$$m_a = \rho_f \pi r^2 l. \tag{17}$$

where $r$ is the cable radius and $l$ is the length of the cable segment. The added mass value corresponds to the mass of the fluid displaced by the body and is added to the inertial mass of the cable segment.

Calnan's implementation of the drag and added mass forces has several aspects which may contribute to simulation error:

1. The values of drag coefficients are assumed which introduces large amount of uncertainty in the simulation as it relies on prior knowledge of the fluid dynamics.

2. The dependence of the drag coefficient on flow velocity and body orientation is neglected;

3. The added mass definition neglects the variation of added mass with respect to the direction of the relative acceleration. For example, if the direction of the cable acceleration is purely axial, minimal fluid will be displaced and thus the

added mass force should be neglected.

4. The hydrodynamic forces are calculated based on the velocity and acceleration of the center of gravity of the cable segment. The variation of hydrodynamic forces along the length of each element is neglected. Furthermore, the hydrodynamic forces are applied only if the center of gravity of the cable segment is below the waterline, otherwise they are set to zero. This will produce impulses on the cable as elements enter and leave the fluid.

This thesis seeks to improve upon these shortcomings of Calnan's cable model.

The standard Morison equation can be improved by incorporating a dynamic drag coefficient that depends on the Reynold's of the flow. For example, Choo and Casarella [32] define the normal drag coefficient for a circular cable as

$$C_D = \begin{cases} 1.45 + 8.55 Re^{-0.9}, & 1 \leq Re < 30 \\ 1.1 + 4 Re^{-0.5}, & 30 \leq Re \leq 10^5 \end{cases} \tag{18}$$

based on experimental data collected by Goldstein [33]. Furthermore, by visualizing the flow around an inclined cylinder Kozakiewicz et al. [34] identified a critical angle of attack of approximately 35 degrees below which the independence principle does not hold. For systems with arbitrary orientations of the cable relative to the flow, alternative formulations of the drag forces can be used. In particular, several researchers such as Driscoll and Nahon [20] have developed empirical "loading functions" that describe the nonlinear breakup of the flow into normal and tangential components. The normal and tangential drag forces are then typically defined [20]

$$F_{D,n} = \frac{1}{2}\rho_f d C_D |V|^2 f_n(\eta) \tag{19a}$$

$$F_{D,t} = \frac{1}{2}\rho_f d C_D |V|^2 f_t(\eta) \tag{19b}$$

where $C_D$ is a common drag coefficient, $V$ is the total relative velocity vector, $f_n$ and $f_t$ are the normal and tangential loading functions.

For modelling submerged and towed cables, many cable modeling approaches have been employed. Early towed cable models utilizing the finite difference method, such as Choo and Casarella's model of a towcable with ship motion along a circular path [35], were restricted to limited towing scenarios. Ablow and Schechter [16] used a finite difference method to model a towed cable array, defined the boundary conditions such that any arbitrary maneuver could be implemented as long as the tow-point position and velocity are known.

In Choo and Casarella's model, the towed body is spherical. The cable is treated as inextensible and has zero bending stiffness. The model incorporates the fluid drag with variable drag coefficients as defined in Equation 18. The model demonstrated good agreement with experimental measurements of the steady-state behavior of the system for stranded wire cables, but poor performance for nylon cables which experience significant vortex shedding effects. Ablow and Schechter's model was used to predict the change in towbody depth during a circular maneuver to within 2% of the measured value. The main limitations of these models are that they utilize various simplifications, including neglecting the bending stiffness of the cable, and have simple boundary conditions.

Driscoll et al. [20] utilized their lumped finite element model to simulate a vertical cable connecting a ship to a caged ROV system. The top node was constrained based on measurements of the ship motion. Only vertical motion and deformations were considered. The drag coefficient of the cage was calibrated based on empirical measurements. The position of the cage was predicted by the model with a standard deviation of 0.07 m or 8% of the RMS value of the measured data. The cable tension was also predicted with a standard deviation of 4 kN or 16% of the RMS value.

Buckham et al. [36] developed a lumped finite element model of a system consisting of a semi-submersible vehicle, a towcable and an actively controlled towbody. The dynamics of both the towing vehicle and the towbody were included in the model. Additionally, nonlinear loading functions were used to describe the drag forces acting on the cable. The model was later validated by Lambert et al. [37]. During a steady tow, the cable tension at the towing vehicle was under-predicted by about 10% compared to sea trial data. They note that 90% of the cable tension results from the drag on the cable, thus the error can be largely attributed to uncertainty in the drag forces.

Nonlinear formulations have also been used to model submerged cables. Sun et al. [38] use a nonlinear finite element method with straight elements to model a towed body system during a turning maneuver. The model includes the rigid body dynamics of the towed body and cable drag correlations based on the angle of incidence. The towed body depth differs from the empirical values by up to 12m and the cable tension is over estimated by about 10 kN compared to a mean value of approximately 35 kN. There is limited discussion of possible sources of error in their work.

The Absolute Nodal Coordinate Formulation has also been used in recent studies. Takehara et al. [39] developed a planar model a submerged rubber tether using the ANCF with nonlinear loading functions developed by Driscoll and Nahon [20]. An intermediate body fixed coordinate frame was used to define the cable mass matrix, which allows for the incorporation of the added fluid inertia only in the normal direction. The model was validated based on small-scale measurements of the tether undergoing pendulum motion and showed good agreement with experimental results. Kim et al. [40] and Park and Kim [41] have developed three-dimensional models of submerged cables using the ANCF, however they did not perform any experimental validation.

Since submerged cable dynamics is typically dominated by the external fluid forces, the formulation of the hydrodynamic forces provide a significant source of uncertainty in most models. In many finite element and finite segment models, the fluid forces are concentrated at the element nodes, which can also contribute significantly to the simulation error. Additionally, for low tension cable dynamics, the bending stiffness of the cable may also affect the accuracy of the simulation. The ANCF finite element method is thus a suitable choice for modelling the tow cable in the proposed model, since the fluid forces can be defined continuously along the length of the cable and bending-stiffness effects are inherent to the model.

Experimental validation of towed cable model is limited, particularly for ANCF finite element models and systems with active heave compensation. In the current study, the ANCF model will be validated using the data obtained in Calnan's flume tank trials [2].

## 2.4 Cable-Sheave Interactions

In Calnan's model [2], the attachment of the cable to the ship is implemented using a prismatic joint which actuates the cable end along a line based on the AHC setpoint and the winch dynamics. The contact between the cable and the sheave and winch are neglected. In Kamman and Huston's model [22], variable length elements are used to capture the reel-in and out of the cable. No models have been found in the literature that include the sheave and winch contact in a towed-cable model.

Several models have been developed, however, for other types of cable-pulley systems. These include reciprocating cable-pulley systems, such as weightlifting machines and elevators, belt-drives, and catenary-pantograph systems. There are two main formulations that are used to model the contact forces, penalty methods and Lagrange multiplier methods [11]. Both approaches can be used to describe normal contact as well as sliding (frictional) contact; however, this section focuses on normal contact as sliding friction effects are not expected to be a significant factor in the towed cable system.

For a body in contact with a surface, a penalty method is implemented by allowing the body to penetrate the surface. Figure 8 shows three possible contact cases: open contact, closed contact without penentration, and closed contact with penetration. Figure 8A shows the open contact case, where the bodies are separated and the penetration $\delta$ has a negative value. Figure 8B illustrates closed contact where the bodies are non-penetrating and the pentration $\delta$ is equal to zero. Figure 8C illustrates closed contact where the bodies are penetrating and the pentration $\delta$ is greater than zero. The normal contact penalty forces are then defined as a function of the relative penetration [42]. The surface thus act like a spring or spring-damper. A simple formulation is given by the Hertz contact theory, where the normal force $F_N$ acting on the body is defined [43]

$$F_N = k\delta^b \tag{20}$$

where $k$ is the contact stiffness, $\delta$ is the relative penetration and $b$ is a positive constant between 1 and 2. In order to model unilateral contact, where the normal force can act in only one direction, the condition $\delta \geq 0$ can be used. Thus if the value of the penetration is negative the bodies are not in contact and no force is applied.

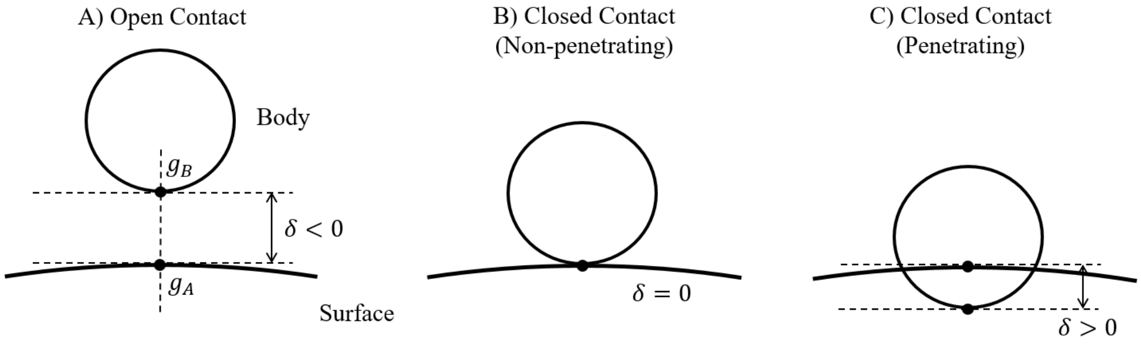

**Figure 8:** Open and closed contact cases.

Penalty methods have a number of disadvantages. Firstly, the penalty results in ill-conditioning of the system of equations and the numerical solution can be computationally expensive as a result [44]. The model may exhibit a large sensitivity to the contact stiffness, which is not a physical property of the system. Lastly, conservation of energy is violated due to the energy stored in the spring. Despite these disadvantages, penalty methods are widely used as a result of their simplicity [11].

Leamy and Wasfy [45] present an early model of a belt-drive system using a contact penalty. The model used straight truss (spring) elements with the normal and tangential contact forces concentrated at the nodes. As a result of using a lumped approach, the model required a very fine discretization of the cable; 100 elements (202 degrees of freedom) were used for each length of the belt equal to half of the pulley circumference. In a separate study [46] a three node element was used to incorporate the cable bending stiffness. Both the tangential and normal force distributions and the wrap angle of the cable around the pulley exhibited a strong dependence on the bending stiffness. Additionally, when the cable element was modified to include the cable bending stiffness [46], only 38 elements per half circumference (154 degrees of freedom) were used.

Lugris et al. present an ANCF model of an elevator with vertically suspended loads on either side of the pulley [7]. The ANCF model uses a contact penalty to determine the normal contact force and a nonlinear friction law for the tangential force. The researchers used 32 elements for a 180° contact arc. They note that the model worked with as few as 3 elements, but if the elements were long they would poorly adapt to the curvature of the pulley at the transitions onto or off of the surface. The poor adaptation of the elements to the surface introduced spurious vibrations into the system as elements entered or exited the contact surface. In contrast, Kerkkannen et al. [47] developed a nonlinear belt drive model using the shear-deformable ANCF elements. With the shear-deformation included only four elements were required for half of the pulley circumference.

Bulín et al. [9] modeled a cable pulley system with one cable end actuated by a motor and a mass sliding on an inclined plane using the ANCF method. The wrap angle of the cable around the pulley experienced small changes of less than 5 degrees throughout the motion. Ten elements were used to model the segment of the cable in contact with the pulley. Reasonable agreement was found between the simulation and experimental measurements of the motion of the load. Ten ANCF elements were used for a contact arc of 150°. The sensitivity of the numerical results to the cable bending stiffness was also examined. While the contact force distribution becomes increasingly nonlinear for increasing values of the bending stiffness, the simulated motion shows only a small dependence on the stiffness value.

In contrast to penalty methods, Lagrange multiplier methods are based on a condition of *impenetrability* [48]. In Figure 8A, the positions of the contact points on the body and the surface are defined by the coordinates $g_A$ and $g_B$, respectively. Considering a body in closed contact with a surface, Figure 8B, the impenetrability condition is defined using a holonomic constraint equation

$$\Phi = g_B - g_A = 0. \tag{21}$$

Thus, the distance between the two contact points along the surface normal vector must be zero for the constraint to be satisfied. In the case of unilateral contact, the constraint becomes

$$\Phi = g_B - g_A \geq 0 \tag{22}$$

such that bodies can separate.

The forces required to satisfy the constraint acting on the body and the surface, respectively, are [49]

$$F_B = -\frac{\partial \Phi}{\partial g_B} \lambda. \tag{23a}$$

$$F_A = -\frac{\partial \Phi}{\partial g_A}\lambda. \tag{23b}$$

The Lagrange multiplier method increases the number of unknowns in the system as $\lambda$ must be calculated in addition to the coordinates $g_A$ and $g_B$. The constraint equation $\Phi$ and the equations of motion of the body form a set of differential algebraic equations. During closed contact, there must also be a condition to check whether the bodies are transitioning from closed to open contact. If the relative acceleration of the bodies $\ddot{g} = \ddot{g}_A - \ddot{g}_A$ is greater than zero, the bodies are separating thus the Lagrange multiplier $\lambda$ is set to zero and no force is applied [48].

A main disadvantage of the Lagrange multiplier method in comparison to a penalty method arises when the contact occurs over a distributed area. The penalty method can be used to describe the contact force as a *continuous* function of spatial or material coordinates, for example the arc parameter $p$ in the ANCF method. With the Lagrange multiplier method, the forces are only determined at a discrete set of contact points, posing a number of challenges. First, each contact point defined must have a Lagrange multiplier associated with it. Each Lagrange multiplier adds a degree of freedom to the resulting governing equations, thus adding to the computational effort required. Secondly, as the cable moves or deforms relative to the surface, the contact points on the surface will no longer match and must be continuously recalculated. Additionally, a unilateral constraint can repeatedly switch from open to closed contact, resulting in a spurious vibration or “chatter” [50].

Lagrange multiplier methods have been used in more limited scenarios than penalty methods. For example, Seo et al. [6] model the bilateral contact between a catenary and a pantograph using a sliding constraint at a single point. Peng et al. [51] model a system with a cable wrapped around multiple pulleys. Motors at each end reel the cable in or out. Instead of modeling the sliding contact along the pulley surfaces, the cable is constrained at each transition point. Variable length elements are used to simulate that reeling behavior, thus avoiding the computational inefficiency of modeling the contact forces.

For existing models of cable-pulley systems, the penalty method is most widely used. It is reasonable to conclude that penalty methods are desirable for systems with large distributed contact areas as the contact forces can be distributed along the element length. The Lagrange multiplier method may be preferable when the number of contact points is limited as it avoids the ill-conditioning issues present in penalty methods.

Experimental validation of cable-pulley models using penalty methods is sparse. Some researchers such as Cepon et al. [5], Takehara et al. [52] and Bulín et al. [9] have performed experiments to validate ANCF models, but focus mainly on sliding behavior of the cable such as cable slip. In this thesis, the focus is mainly on variations in normal contact forces. The study by Bulín et al is the only study found in the literature of cable-pulley contact where the wrap angle of the cable around the pulley changes throughout the motion. In their study, the wrap angle changed by only 5°, estimated based on the geometry provided, whereas in the current study large changes in wrap angle are expected due to the motion of the ship in waves. Another area that has been unexplored in the literature is the contact between the cable and the three-dimensional groove of a sheave. Most cable-pulley models examine only planar contact.

## 2.5 Summary

In this chapter, various methods for modelling flexible cables, submerged cable dynamics and cable-surface contact were described. The Absolute Nodal Coordinate Formulation was found to be advantageous as continuous distributions of the external hydrodynamic and contact forces along the length of the element can be used. In this thesis, the cable will be modeled using the ANCF method.

A contact penalty method will be used to define contact forces acting on the cable, as it provides a simple and effective method to define unilateral contact forces that are distributed along the length of the element. Thus, the cable may come into and out of contact with the sheave surface at any point along its length. This will facilitate simulations of systems where the wrap angle of the cable around the sheave varies over time or where the cable detaches entirely from the sheave. Since the ship undergoes translations and rotations in three dimensions, the cable may detach from the sheave by sliding up the walls of the sheave groove. A model of the contact forces accounting for the shape of the groove will also be developed.

The following chapter describes the formulation of the cable model, the hydrodynamic loads and the normal contact forces.

# 3 Cable Model and Simulation

In this chapter, the development of the finite element cable model and computer simulation are described. The three-dimensional cable model is based on the Absolute Nodal Coordinate Formulation (ANCF). The hydrodynamic forces are described using the semi-empirical Morison equation and a nonlinear contact penalty method is implemented to describe the normal contact with the winch and sheave surfaces. Section 3.1 outlines the geometry and kinematics of the ship. In Section 3.2, the formulation of the ANCF cable element and its structural matrices are described. Section 3.3 details the model of the hydrodynamic loading based on the Morison equation. In Section 3.4, the contact penalty method is implemented to provide the cable-sheave and cable-winch interactions. Section 3.5 describes the formulation of the kinematic constraints, which are used to fix the cable to the winch drum and eliminate redundant coordinates. Lastly, Section 3.7 shows the complete governing equations and describes the numerical solution.

## 3.1 Ship Geometry and Kinematics

Figure 9 shows two coordinate frames, the $x, y$, and $z$ axes which make up the inertial frame and the $X, Y$, and $Z$ axes comprising the body-fixed frame. The position of the ship's center of gravity is represented by a position vector $\mathbf{r}_{CG}$ in the absolute (or inertial) coordinate frame. In the ship's body-fixed coordinate frame, the origin is located at the center of gravity of the ship. Position vectors in the body-fixed frame are denoted $\mathbf{s} = [X\ Y\ Z]^T$. Three euler angles - yaw, pitch, and roll or $\alpha, \beta$ and $\gamma$, respectively - are used to describe the orientation of the ship.

The transformation between the body fixed frame and the inertial frame is

$$\mathbf{r} = \mathbf{R}_B^I(\alpha, \beta, \gamma)\mathbf{s} + \mathbf{r}_{CG} = \mathbf{R}_z(\alpha)\mathbf{R}_y(\beta)\mathbf{R}_x(\gamma)\mathbf{s} + \mathbf{r}_{CG} \tag{24}$$

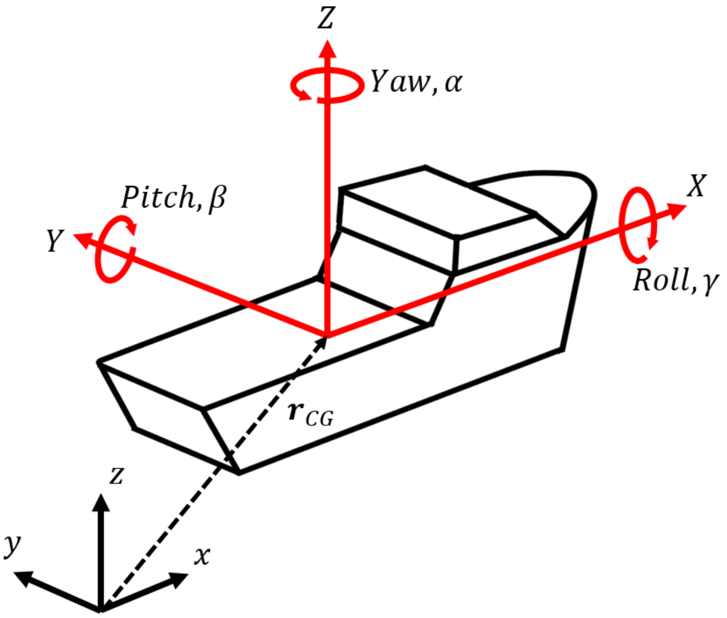

**Figure 9:** Schematic of the inertia coordinate frame $(x, y, z)$ and body fixed coordinate frame $(X, Y, Z)$

with

$$\mathbf{R}_z(\alpha) = \begin{bmatrix} \cos\alpha & -\sin\alpha & 0 \\ \sin\alpha & \cos\alpha & 0 \\ 0 & 0 & 1 \end{bmatrix} \tag{25a}$$

$$\mathbf{R}_y(\beta) = \begin{bmatrix} \cos\beta & 0 & \sin\beta \\ 0 & 1 & 0 \\ -\sin\beta & 0 & \cos\beta \end{bmatrix} \tag{25b}$$

$$\mathbf{R}_x(\gamma) = \begin{bmatrix} 1 & 0 & 0 \\ 0 & \cos\gamma & -\sin\gamma \\ 0 & \sin\gamma & \cos\gamma \end{bmatrix} . \tag{25c}$$

The equations of motion of the finite element cable model were developed in the inertial coordinate frame. The finite element formulation is described in the following section.

## 3.2 ANCF Cable Model and Internal Forces

The Absolute Nodal Coordinate Formulation, introduced by Shabana [23], is a widely used method based on the Euler-Bernoulli beam theory for modeling flexible cables. Each ANCF element consists of two nodes. The position of an arbitrary point on the element in the inertial coordinate frame is described by a parametric function

$$\mathbf{r}(p) = [x(p) \quad y(p) \quad z(p)]^T \tag{26}$$

with $p \in [0, L]$ where $L$ is the undeformed element length. The generalized coordinate vector $\mathbf{q}$ consists of the absolute positions of the nodes and slope vectors at each node:

$$\mathbf{q} = [\mathbf{r}(0) \quad \mathbf{r}_p(0) \quad \mathbf{r}(L) \quad \mathbf{r}_p(L)]^T \tag{27}$$

where $\mathbf{r}_p$ is the derivative of $\mathbf{r}$ and is a vector tangent to the cable centerline. Figure 10 shows a deformed cable element at the top and the equivalent undeformed element at the bottom with the nodes represented by closed circle. The position vector $\mathbf{r}$ of an arbitrary point on the cable is measured to the centerline of the cable and can be interpolated from the generalized coordinates using the equation

$$\mathbf{r}(p) = \mathbf{S}(p)\mathbf{q}, \tag{28}$$

where $\mathbf{S}(p)$ is the shape function which represents the cubic polynomial given by

$$\mathbf{S}(p) = \begin{bmatrix}(1-3\xi^2+2\xi^3)\mathbf{I}_3 & (\xi-2\xi^2+\xi^3)\mathbf{I}_3 & (3\xi^2-2\xi^3)\mathbf{I}_3 & (\xi^2-\xi^3)\mathbf{I}_3\end{bmatrix}, \tag{29}$$

where $\mathbf{I}_3$ is a 3x3 identity matrix and $\xi = p/L$ is the arc parameter normalized by the element length. This definition of the cable element does not include shear deformation. The cross-section of the cable element is always perpendicular to the cable centerline.

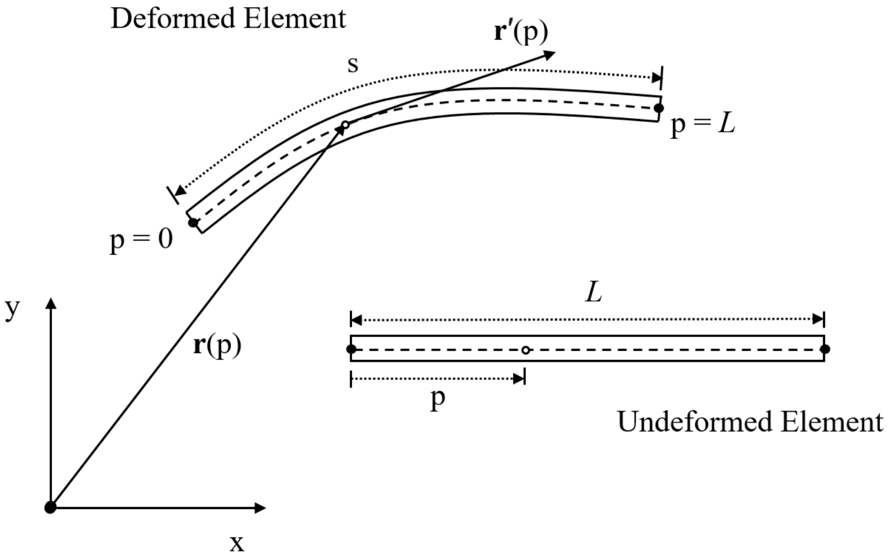

**Figure 10:** Deformed cable element and equivalent undeformed element in the inertial coordinate frame.

Using the standard matrix form of the Newton-Euler equations, the element equations of motion are

$$\mathbf{M}\ddot{\mathbf{q}} = \mathbf{Q}_{\mathrm{ext}} - \mathbf{Q}_{\mathrm{int}} \tag{30}$$

where $\mathbf{M}$ is the mass matrix, $\mathbf{Q}_{\mathrm{ext}}$ is the *net* vector of generalized external forces, and $\mathbf{Q}_{\mathrm{int}}$ is the generalized internal force. The generalized internal force $\mathbf{Q}_{\mathrm{int}}$ is given by the sum

$$\mathbf{Q}_{\mathrm{int}} = \mathbf{Q}_l + \mathbf{Q}_t + \mathbf{Q}_d \tag{31}$$

where $\mathbf{Q}_l$ is the longitudinal (tensile) elastic force, $\mathbf{Q}_t$ is the transverse (bending) elastic force and $\mathbf{Q}_d$ is the internal damping force. The net generalized external force is given by the sum

$$\mathbf{Q}_{\text{ext}} = \mathbf{Q}_g + \mathbf{Q}_H + \mathbf{Q}_N \tag{32}$$

where $\mathbf{Q}_g$ is the generalized gravitational force, $\mathbf{Q}_H$ is the generalized hydrodynamic force, and $\mathbf{Q}_N$ is the generalized normal contact force. Additionally, the first element is constrained to the winch surface using a kinematic constraint. The governing equations for the first element are

$$\mathbf{M}\ddot{\mathbf{q}} = \mathbf{Q}_{\text{ext}} - \mathbf{Q}_{\text{int}} + \mathbf{Q}_c \tag{33}$$

where $\mathbf{Q}_c$ is the generalized constraint force.

Given a distributed force per unit length $\mathbf{f}_i(p)$, the generalized force vector $\mathbf{Q}_i$ can be determined by premultiplying by the transpose of the shape function and integrating over the length of the element [53]:

$$\mathbf{Q}_i = \int_0^L \mathbf{S}^T \mathbf{f}_i(p) dp. \tag{34}$$

For example, the generalized gravitational force $\mathbf{Q}_g$ is given by

$$\mathbf{Q}_g = \int_0^L \mathbf{S}^T \rho A [0 \quad 0 \quad -g]^T dp \tag{35}$$

where $\rho$ is the cable density, $A$ is the cross-sectional area, and $g$ is the acceleration due to gravity. The formulation of the remaining generalized forces and the mass matrix are described in the following sections.

### 3.2.1 Mass Matrix

Using the variational mass lumping approach the mass matrix $\mathbf{M}$ is derived from the kinetic energy of the element $K$ [23]. The kinetic energy of an infinitesimal cable segment is

$$dK = \frac{1}{2}\rho A \left|\dot{\mathbf{r}}(p)\right|^2 dp, \tag{36}$$

where $\rho$ is the cable density, $A$ is the cross-sectional area and $\dot{\mathbf{r}}(p)$ is the velocity of the cable at an arbitrary point. Integrating the differential kinetic energy $dK$ over the interval 0 to $L$ and substituting $\dot{\mathbf{r}}(p) = \mathbf{S}(p)\dot{\mathbf{q}}$ gives the total kinetic energy of the element:

$$K = \int_0^L \frac{1}{2}\rho A \, \dot{\mathbf{r}}(p)^T \dot{\mathbf{r}}(p) \, dp = \frac{1}{2}\rho A \int_0^L \dot{\mathbf{q}}^T \mathbf{S}(p)^T \mathbf{S}(p) \dot{\mathbf{q}} \, dp. \tag{37}$$

The mass matrix is then given by the second derivative of the kinetic energy with respect to the generalized velocity vector $\dot{\mathbf{q}}$ [23]:

$$\mathbf{M} = \frac{\partial^2 K}{\partial \dot{\mathbf{q}} \partial \dot{\mathbf{q}}} = \rho A \int_0^L \mathbf{S}(p)^T \mathbf{S}(p) \, dp. \tag{38}$$

The above formulation results in a constant mass matrix $\mathbf{M}$ which can be evaluated symbolically prior to the simulation.

#### 3.2.2 Longitudinal Elastic Force

The longitudinal stiffness force represents the tensile stiffness of the element. Berzeri and Shabana [29] derive the stiffness from the longitudinal strain energy $U_l$ given by

$$U_l = \frac{1}{2} \int_0^L EA\varepsilon^2 dp \tag{39}$$

where $E$ is the Young's modulus, $A$ is the cross-sectional area, $\varepsilon$ is the longitudinal strain. The generalized longitudinal force $\mathbf{Q}_l$ is then given by the derivative of the strain energy with respect to the generalized coordinates:

$$\mathbf{Q}_l = \left(\frac{\partial U_l}{\partial \mathbf{q}}\right)^T = EA \int_0^L \varepsilon \frac{\partial \varepsilon}{\partial \mathbf{q}} dp \tag{40}$$

where $\mathbf{Q}_l$ represents the longitudinal component of the elastic force and $\mathbf{Q}_t$ represents the transverse or bending component.

Berzeri and Shabana define $\varepsilon$ as the Green-Lagrange strain given by

$$\varepsilon = \frac{1}{2}({\mathbf{r}_p}^T \mathbf{r}_p - 1). \tag{41}$$

However, using the above strain definition results in coupling of the longitudinal strains to the element curvature, since the slope vector $\mathbf{r}_p$ defines not only the shape of the element, but the distribution of strain across the element. As a result, an element with no overall strain (i.e. an arc length equal to the unstretched length $L$) but a non-zero curvature will have non-zero strain along its length. The coupling of the longitudinal and bending deformations leads to increased stiffness of the numerical solution in addition to erroneous cable tensions in elements with significant curvatures.

It is thus desirable to decouple the longitudinal strains from the curvature. Yue et al. [54] present an alternative stiffness force definition that alleviates the coupled behavior. First a secondary set of generalized coordinates $\mathbf{q}^\Delta$, representing only the longitudinal deformation of the ANCF cable element, is defined:

$$\mathbf{q}^\Delta = \begin{bmatrix} 0 & |\mathbf{r}'(0)| & \int_0^L |\mathbf{r}'(p)| dp & |\mathbf{r}'(L)| \end{bmatrix}^T . \tag{42}$$

This formulation represents a one-dimensional cable element that is parameterized equivalent to the full ANCF element. Thus, the longitudinal coordinate of an arbitrary point on the element is given by

$$r^\Delta = \mathbf{S}^\Delta \mathbf{q}^\Delta \tag{43}$$

where $\mathbf{S}^\Delta$ is the one-dimensional shape function

$$\mathbf{S}^\Delta = \begin{bmatrix} (1 - 3\xi^2 + 2\xi^3) & (\xi - 2\xi^2 + \xi^3) & (3\xi^2 - 2\xi^3) & (\xi^2 - \xi^3) \end{bmatrix} . \tag{44}$$

The one-dimensional coordinate $r^{\Delta}$ is then substituted into the Green-Lagrange strain (Equation 41) giving a decoupled longitudinal strain $\varepsilon^{\Delta}$

$$\varepsilon^{\Delta} = \frac{1}{2}\left[\left(\frac{\partial r^{\Delta}}{\partial p}\right)^2 - 1\right] = \frac{1}{2}\left[(\mathbf{S}_p^{\Delta}\mathbf{q}^{\Delta})^T(\mathbf{S}_p^{\Delta}\mathbf{q}^{\Delta}) - 1\right] \tag{45}$$

where the subscript $p$ represents the derivative with respect to $p$. Yue et al. [54] then define the longitudinal elastic force $\mathbf{Q}_l$ by substituting the decoupled strain $\varepsilon^{\Delta}$ into Equation 40 as

$$\mathbf{Q}_l = EA\int_0^L \varepsilon^{\Delta}\frac{\partial \varepsilon^{\Delta}}{\partial \mathbf{q}}dp = \frac{1}{2}EA\int_0^L (\mathbf{q}^{\Delta T}\mathbf{S}^{\Delta T}\mathbf{S}^{\Delta}\mathbf{q}^{\Delta} - 1)(\mathbf{S}_p^{\Delta}\mathbf{q}^{\Delta})\left(\frac{\partial \mathbf{q}^{\Delta}}{\partial \mathbf{q}}\right)^T \mathbf{S}_p^{\Delta T}dp \tag{46}$$

where $\partial\mathbf{q}^{\Delta}/\partial\mathbf{q}$ is a 4x12 Jacobian matrix given by

$$\frac{\partial \mathbf{q}^{\Delta}}{\partial \mathbf{q}} = \begin{bmatrix} \mathbf{0}_{1x12} \\ \\ \dfrac{\mathbf{r}_p(0)^T}{|\mathbf{r}_p(0)|}\mathbf{S}_p(0) \\ \\ \displaystyle\int_0^L \frac{\mathbf{r}_p(p)^T}{|\mathbf{r}_p(p)|}\mathbf{S}_p(p)dp \\ \\ \dfrac{\mathbf{r}_p(L)^T}{|\mathbf{r}_p(L)|}\mathbf{S}_p(L) \end{bmatrix}. \tag{47}$$

In this work, each of the integrals in Equations 42, 46, and 47 are evaluated using a numerical quadrature with trapezoidal weights.

### 3.2.3 Transverse Stiffness

Similar to the longitudinal stiffness, the transverse elastic force is derived from the strain energy $U_t$ given by

$$U_t = \int_0^L EI\kappa^2 dp \tag{48}$$

where $E$ is the Young's modulus, $I$ is the second moment of area and $\kappa$ is the curvature [29]. The curvature follows the Seret-Frenet definition and is given by

$$\kappa = \left| \frac{d\mathbf{r}^2}{ds^2} \right| = \frac{|\mathbf{r}_p \times \mathbf{r}_{pp}|}{|\mathbf{r}_p|^3} \tag{49}$$

where $s$ is the arc length and $\mathbf{r}_p$ and $\mathbf{r}_{pp}$ are the first and second partial derivatives of $\mathbf{r}$ with respect to $p$ [29]. The transverse elastic force is then given by

$$\mathbf{Q}_t = \frac{\partial U_t}{\partial \mathbf{q}} = EI \int_0^L \kappa \frac{\partial \kappa}{\partial \mathbf{q}} dp. \tag{50}$$

Significant simplification of Equation 50 can be achieved by assuming that the longitudinal deformations are small (i.e. $|\mathbf{r}_p| \approx 1$) and thus the arc length $s$ is approximately equal to the parameter $p$, in which case the curvature simplifies to [29]

$$\kappa \approx |\mathbf{r}_{pp}|. \tag{51}$$

Substituting Equation 51 into Equation 50, the transverse elastic force becomes

$$\mathbf{Q}_t = \left[ EI \int_0^L \mathbf{S}_{pp}(p)^T \mathbf{S}_{pp}(p) dp \right] \mathbf{q}. \tag{52}$$

As with the mass matrix, the integral in Equation 52 is a constant matrix and can be evaluated symbolically prior to the simulation.

### 3.2.4 Damping

The internal damping force $\mathbf{Q}_d$ serves to include internal energy dissipation as well as improve the numerical stability of the simulation. For submerged cables it is common to neglect the internal cable damping [55] since the external fluid damping dominates. However, in the current work the inclusion of internal damping was found to have a significant effect on the numerical stiffness and stability of the simulation. Additionally, the damping effects may be significant in the unsubmerged section of the cable; thus, internal damping was implemented based on a Rayleigh dissipation function.

The Rayleigh dissipation function represents one-half of the energy dissipated during the motion and has a general form

$$R = 1/2 \int c\dot{u}^2 dV \tag{53}$$

where $c$ is a damping factor and $u$ is a generalized coordinate [56]. The generalized coordinate is chosen to be the gradient $\mathbf{r}_p = \partial \mathbf{r}/\partial p$, where $\mathbf{r}$ is the absolute position of a cable segment, such that energy is dissipated if the velocity of a differential cable segment differs from the velocity of adjacent segments. Thus, damping will occur during bending and axial deformations. The energy dissipation will also occur during rigid body rotations, however the additional dissipation can be viewed as viscous damping due to air or water resistance. The Rayleigh dissipation function becomes

$$R = 1/2 \int_0^L c(\dot{\mathbf{r}}_p \cdot \dot{\mathbf{r}}_p) dp \tag{54}$$

The damping force $\mathbf{Q}_d$ is then given by

$$\mathbf{Q}_d = \frac{\partial R}{\partial \dot{\mathbf{q}}} = c \int_0^L \mathbf{S}_p^T \mathbf{S}_p dp \; \dot{\mathbf{q}}. \tag{55}$$

The damping coefficient $c$ is not an intrinsic material property and must therefore be estimated on a case-by-case basis based on a measurable property such as the cable damping ratio. The estimation of the damping coefficient for the flume-scale and full-scale cable models is further discussed in Sections 4.3 and 5.1, respectively. The next section describes the hydrodynamic force model used for the flume and full-scale systems.

## 3.3 Hydrodynamic Forces

The external hydrodynamic force per unit length $\mathbf{f}_H$ consists of three components: the drag force $\mathbf{f}_D$, the inertia force $\mathbf{f}_I$ and the buoyancy force $\mathbf{f}_B$, such that

$$\mathbf{f}_H = \mathbf{f}_D + \mathbf{f}_I + \mathbf{f}_B. \tag{56}$$

The buoyancy force is given by Archimedes' principal,

$$\mathbf{f}_B = -\rho_f A \mathbf{g} \tag{57}$$

where $\mathbf{g} = [0 \quad 0 \quad -9.81]^T$ m/s$^2$ is the gravitational acceleration vector, $\rho_f$ is the fluid density and $A$ is the cable corss-sectional area. The drag force follows Driscoll and Nahon's [20] definition, utilizing nonlinear loading functions and is defined in Section 3.3.1. Section 3.3.2 shows the derivation of the inertia force from the Morison equation (Equation 13). The integration of the distribution of hydrodynamic forces over the length of each element is outlined in Section 3.3.3. Finally the forces acting on the towed body are defined in Section 3.3.4.

### 3.3.1 Nonlinear Drag Force

The drag forces used in this work are based on the model employed by Driscoll and Nahon [20] and Buckham et al. [36]. The model accounts for the nonlinear decomposition of the drag force into normal and tangential components and exhibits good agreement with experimental studies of drag forces on towed cables over a wide range of towing conditions [20]. The components of the drag force are

$$\mathbf{f}_{D,n} = -\frac{1}{2}\rho_f d C_D |\mathbf{V}|^2 \frac{\mathbf{V}_n}{|\mathbf{V}_n|} f_n \tag{58a}$$

$$\mathbf{f}_{D,t} = -\frac{1}{2}\rho_f d C_D |\mathbf{V}|^2 \frac{\mathbf{V}_t}{|\mathbf{V}_t|} f_t \operatorname{sgn}(\mathbf{V}_t \cdot \mathbf{u}_t) \tag{58b}$$

where $d$ is the cable diameter, $C_D$ is a common drag coefficient, $\mathbf{V} = \mathbf{V_f} - \dot{\mathbf{r}}$ is the relative velocity between the cable and flow, $f_n$ and $f_t$ are normal and tangential empirical loading functions, $\mathbf{V}_n$ and $\mathbf{V}_t$ are the normal and tangential components of $\mathbf{V}$ given by

$$\mathbf{V}_t = (\mathbf{V} \cdot \mathbf{u}_t)\mathbf{u}_t \tag{59a}$$

$$\mathbf{V}_n = \mathbf{V} - \mathbf{V}_t \tag{59b}$$

and $\mathbf{u}_t = \mathbf{r}_p/|\mathbf{r}_p|$ is the unit tangent vector along the cable centerline [36]. Figure 11 illustrates the absolute and relative flow velocity vectors and their components normal and tangential to the cable element. The absolute flow velocity vector $\mathbf{V}_f$ is shown as a solid blue line, the relative flow velocity vectors $\mathbf{V}$ is shown as a solid red line and their component vectors are shown as dotted lines.

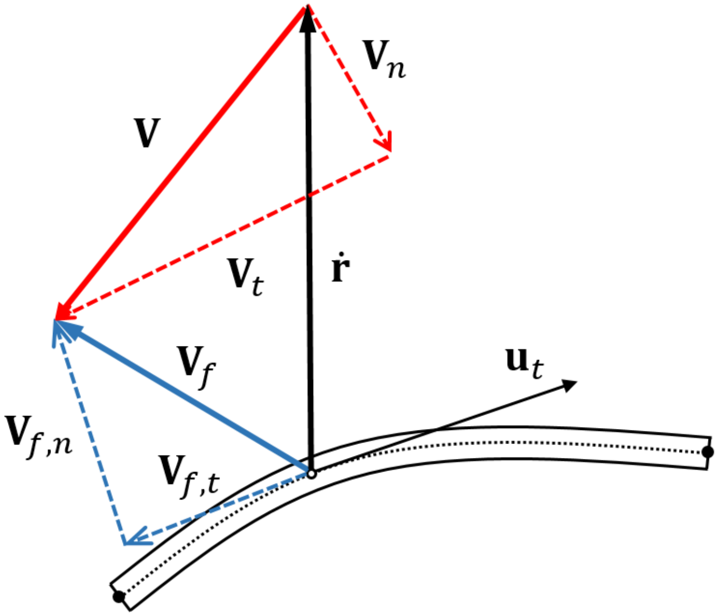

**Figure 11:** Absolute and relative flow velocity vectors in relation to a cable element

The empirical loading functions are given by Driscoll and Nahon [20] as

$$f_n = 0.5 - 0.1\cos\eta + 0.1\sin\eta - 0.4\cos 2\eta - 0.11\sin 2\eta \tag{60a}$$

$$f_t = 0.01\left(2.009 - 0.3858\eta + 1.9159\eta^2 - 4.1615\eta^3 + 3.5064\eta^4 - 1.1873\eta^5\right) \tag{60b}$$

where $\eta \in [0 \ \ \pi/2]$ is the angle between the flow vector and the cable centerline in radians. Relationships developed by Choo and Casarella [32] between the drag coefficient $C_D$ and Reynold's number $Re$ for towed cables are

$$C_D(Re) = \begin{cases} \dfrac{8\pi}{ReS}(1 - 0.87S^{-2}), & 0 < Re \leq 1 \\ 1.45 + 8.55Re^{-0.9}, & 1 < Re < 30 \\ 1.1 + 4Re^{-0.5}, & 30 \leq Re < 10^5 \end{cases} \tag{61}$$

where

$$S = -0.077215665 + \ln(8Re^{-1}) \tag{62}$$

and

$$Re = \frac{\rho_f d\mathbf{V}_n}{\mu} \tag{63}$$

Various experimental studies of submerged cables [57, 58] show that the *mean* drag acting on the cable can be much higher than for rigid cylinders. The increase in drag is a result of vibration of the cable due to vortex shedding. An additional force $\mathbf{f}_{D,amp}$ is applied to the cable to capture the drag amplification due to vortex-induced vibrations (VIV). It is defined

$$\mathbf{f}_{D,amp} = G(\overline{\mathbf{f}}_{D,n} + \overline{\mathbf{f}}_{D,t}) \tag{64}$$

where $G$ is an amplification factor and $\overline{\mathbf{f}}_{D,n}$ and $\overline{\mathbf{f}}_{D,t}$ are the steady state values of normal and tangential drag forces, which are obtained using Equation 58 with the cable velocity $\dot{\mathbf{r}}$ set to zero. In this way, only the mean component of the drag force is amplified and not the transient components.

The total drag force per unit length $\mathbf{f}_D$ from Equation 56 is

$$\mathbf{f}_D = \mathbf{f}_{D,n} + \mathbf{f}_{D,t} + \mathbf{f}_{D,amp}. \tag{65}$$

### 3.3.2 Added Mass and Inertia Force

Within Equation 56, the non-drag terms in the Morison equation are collectively referred to as the inertia force $\mathbf{f}_I$ given by

$$\mathbf{f}_I = \rho_f A C_m(\dot{\mathbf{V}}_{f,n} - \ddot{\mathbf{r}}_n) + \rho_f A \dot{\mathbf{V}}_{f,n} \tag{66}$$

where $C_m$ is the hydrodynamic mass coefficient, $\dot{\mathbf{V}}_{f,n}$ is the acceleration of the flow normal to the cable, and $\ddot{\mathbf{r}}_n$ is the normal component of the cable acceleration [30].

The first term in the above equation $\rho_f A C_m(\dot{\mathbf{V}}_{f,n} - \ddot{\mathbf{r}}_n)$ is the hydrodynamic mass force. When the cable accelerates relative to the fluid it must also accelerate the fluid surrounding it. If the relative acceleration is normal to the cable's centerline the volume of fluid displaced is equal to that of the cable, however, if the cable moves tangential to its own centerline, then a minimal amount of fluid is displaced. Thus, the hydrodynamic mass force consists only of the component of the acceleration *normal* to the cable centerline. While the hydrodynamic mass force accounts for the inertia of the fluid in the immediate vicinity of the body, the second term in Equation 66, referred to as the Froude-Krylov force, occurs as a result of the pressure-gradient created by the absolute acceleration of the fluid in the outer-flow region.

The normal acceleration vector $\ddot{\mathbf{r}}_n$ can be obtained using the following relation

$$\begin{aligned}\ddot{\mathbf{r}}_n &= \ddot{\mathbf{r}} - \ddot{\mathbf{r}}_t \\ &= \ddot{\mathbf{r}} - \mathbf{u}_t(\mathbf{u}_t^T\ddot{\mathbf{r}}) \\ &= \mathbf{S}\ddot{\mathbf{q}} - \mathbf{u}_t(\mathbf{u}_t^T\mathbf{S}\ddot{\mathbf{q}}) \\ &= (1 - \mathbf{u}_t^T\mathbf{u}_t)\mathbf{S}\ddot{\mathbf{q}}\end{aligned} \tag{67}$$

where $\mathbf{u}_t$ is the unit vector tangent to the cable centerline and $\mathbf{S}$ is the element shape function and $\ddot{\mathbf{q}}$ is the generalized acceleration vector.

Note that the inertia force $\mathbf{f}_I$ contains the cable acceleration $\ddot{\mathbf{r}} = \mathbf{S}\ddot{\mathbf{q}}$ and the governing equations shown in Equation 30 are *implicit* as the generalized acceleration $\ddot{\mathbf{q}}$ appears on both sides of the equations. The governing equations can be written in *explicit* form by isolating the component of the inertia force proportional to the cable acceleration and moving it to the left side of Equation 30. Thus explicit numerical integration methods such as MATLAB's *ode15s* can be used. The component of the inertia force proportional to $\ddot{\mathbf{r}}_n$ is denoted $\mathbf{f}_a$ and the remaining terms are denoted $\mathbf{f}_I'$, thus

$$\mathbf{f}_I = \mathbf{f}_a + \mathbf{f}_I', \tag{68}$$

where

$$\mathbf{f}_a = -\rho_f A C_m \ddot{\mathbf{r}}_n. \tag{69a}$$

$$\mathbf{f}_I' = \rho_f A(C_m + 1)(\dot{\mathbf{V}}_{f,n}) + \rho_f A\dot{\mathbf{V}}_{f,n}. \tag{69b}$$

The explicit form of the governing equations will be further detailed in the following section where the definitions of the generalized hydrodynamic forces are described.

### 3.3.3 Generalized Hydrodynamic Force

The total generalized hydrodynamic force $\mathbf{Q}_H$ is given by the integral over the length of the element as

$$\mathbf{Q}_H = \int_0^L \mathbf{S}(p)^T \mathbf{f}_H dp = \int_0^L \mathbf{S}(p)^T (\mathbf{f}_D + \mathbf{f}_I' + \mathbf{f}_a + \mathbf{f}_B) dp \tag{70}$$

The component of containing the added mass force $\mathbf{f}_a$ is isolated giving the generalized added mass force $\mathbf{Q}_a$:

$$\mathbf{Q}_a = \int_0^L \mathbf{S}(p)^T \mathbf{f}_a dp = -\rho_f A C_m \int_0^L \mathbf{S}(p)^T \ddot{\mathbf{r}}_n dp \tag{71}$$

Subsituting the expression for the normal acceleration $\ddot{\mathbf{r}}_n$ from Equation 67, $\mathbf{Q}_a$ becomes

$$\mathbf{Q}_a = -\rho_f A C_m \int_0^L \mathbf{S}^T (1 - \mathbf{u}_t^T \mathbf{u}_t) \mathbf{S} dp \; \ddot{\mathbf{q}} \tag{72}$$

The generalized added mass force $\mathbf{Q}_a$ has a form similar to the inertial force of the cable, $\mathbf{M}\ddot{\mathbf{q}}$, and can thus be written

$$\mathbf{Q}_a = -\mathbf{M}_a \ddot{\mathbf{q}} \tag{73}$$

where $\mathbf{M}_a$ is the added mass matrix,

$$\mathbf{M}_a = \rho_w C_m A \int_0^L \mathbf{S}^T (1 - \mathbf{u}_t^T \mathbf{u}_t) \mathbf{S} dp. \tag{74}$$

The equations of motion for the element from Equation 30 can then rewritten as explicit ODEs of the form

$$(\mathbf{M} + \mathbf{M}_a)\ddot{\mathbf{q}} = \mathbf{Q}_{\text{ext}} - \mathbf{Q}_{\text{int}}. \tag{75}$$

where the generalized external force $\mathbf{Q}_{\text{ext}}$ now excludes the added mass force $\mathbf{Q}_a$:

$$\mathbf{Q}_{\text{ext}} = \mathbf{Q}_g + \mathbf{Q}_N + \mathbf{Q}_h. \tag{76}$$

The remaining terms in Equation 70 are denoted $\mathbf{Q}_h$:

$$\mathbf{Q}_h = \int_0^L \mathbf{S}(p)^T(\mathbf{f}_D + \mathbf{f}'_I + \mathbf{f}_B)dp \tag{77}$$

The generalized force $\mathbf{Q}_h$ can be approximated using a numerical quadrature with equally-spaced integration points. Three possible conditions are considered for each element: the element is fully submerged below the waterline, the element is partially submerged, or the element is unsubmerged. Figure 12 shows a partially submerged element with the waterline shown as a dotted line and the integration points shown as open circles, except for the nodes which are shown as closed circles. The index of the first integration point below the waterline is denoted $j^*$.

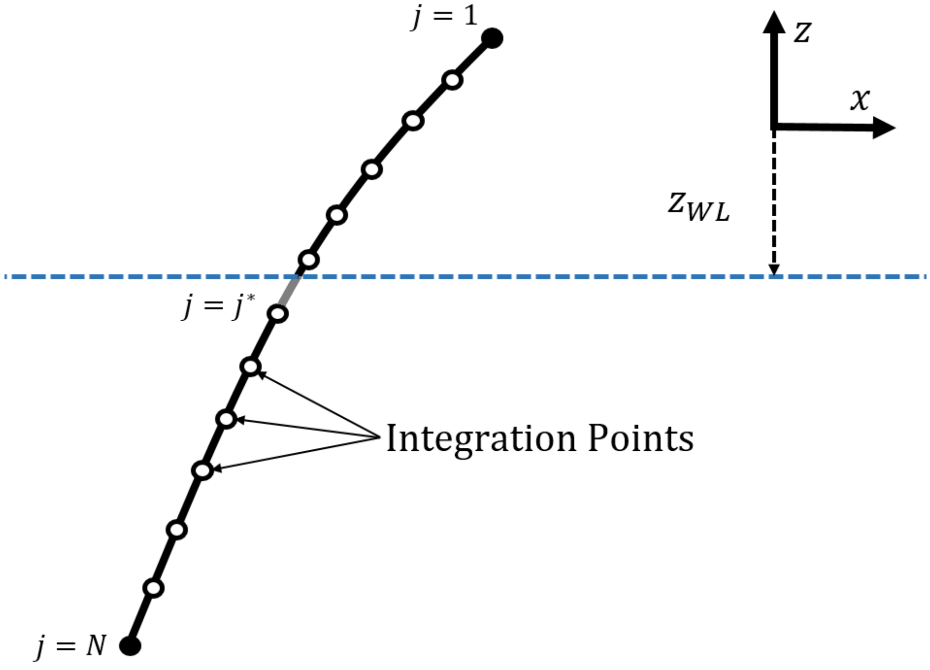

**Figure 12:** Partially submerged cable element.

For each condition, the generalized force $\mathbf{Q}_h$ is

$$\mathbf{Q}_h = \begin{cases} \mathbf{0}_{12\times 1}, & \text{if unsubmerged} \\ \frac{L}{N_I}\sum_{j=1}^{N_I} \mathbf{S}(p_i)^T \mathbf{f}_h(p_i) w_i + \mathbf{Q}_h^*, & \text{if partially sugmerged} \\ \frac{L}{N_I}\sum_{j=1}^{N_I} \mathbf{S}(p_i)^T \mathbf{f}_h(p_i) w_i, & \text{if fully sugmerged.} \end{cases} \tag{78}$$

where $N_I$ is the number of integration points, $p_j$ is the parameter value corresponding to the integration point and $w_j$ is the quadrature weight. The quadrature weights $w_j$ are defined using the trapezoidal rule and are given by

$$w_j = \begin{cases} 0, & z(p_j) \geq z_{WL} \\ 0.5, & z(p_j) < z_{WL} \text{ and } j \in \{1, j^*, N\} \\ 1, & z(p_j) < z_{WL} \text{ and } j \in \{2, 3, ..., N-1\} \backslash j^* \end{cases} \tag{79}$$

where $z$ is the vertical position of the point and $z_{WL}$ is the vertical position of the waterline.

In Figure 12 the interval between point $j^*$ and the waterline is shown as a light grey segment. The additional force $\mathbf{Q}_h^*$ in the partially submerged case accounts for the force acting on the light grey interval and is found by taking the trapezoidal area of the force distribution between point $j^*$ and the waterline:

$$\mathbf{Q}_h^* = \frac{1}{2}[\mathbf{S}(p^*)^T \mathbf{f}_H(p^*) + \mathbf{S}(p_{WL})^T \mathbf{f}_H(p_{WL})](p^* - p_{WL}). \tag{80}$$

where $p^*$ is the value of the arc parameter $p$ at point $j^*$ and $p_{WL}$ is the value of the arc parameter at the waterline.

Similarly, the added mass matrix $\mathbf{M}_a$ in Equation 75 is replaced with a quadrature. If the element is unsubmerged the added mass matrix is given by

$$\mathbf{M}_a = \mathbf{0}_{12\times 12}, \tag{81}$$

if the element is fully submerged, the added mass is

$$\mathbf{M}_a = \rho_w C_m A \frac{L}{N} \sum_{j=1}^{N} w_j \mathbf{S}(p_j)^T [1 - \mathbf{u}_t(p_j)^T \mathbf{u}_t(p_j)] \mathbf{S}(p_j), \tag{82}$$

and if the element is partially submerged the added mass matrix is

$$\mathbf{M}_a = \rho_w C_m A \frac{L}{N} \sum_{j=1}^{N} w_j \mathbf{S}(p_j)^T [1 - \mathbf{u}_t(p_j)^T \mathbf{u}_t(p_j)] \mathbf{S}(p_j) + \mathbf{M}_a^*. \tag{83}$$

The same quadrature weights defined in Equation 79 are used in Equations 82 and 83.

The additional added mass component $\mathbf{M}_a^*$ in the partially submerged case corresponds to the segment of cable between point $j^*$ and the waterline and is given by the trapezoidal area of the integral in Equation 74 over the interval from point $j^*$ to the waterline:

$$\begin{aligned} \mathbf{M}_a^* = \frac{1}{2} \rho_w C_m A \left\{ \mathbf{S}(p^*)^T [1 - \mathbf{u}_t(p^*)^T \mathbf{u}_t(p^*)] \mathbf{S}(p^*) \right. \\ \left. + \mathbf{S}(p_{WL})^T [1 - \mathbf{u}_t(p_{WL})^T \mathbf{u}_t(p_{WL})] \mathbf{S}(p_{WL}) \right\} (p^* - p_{WL}). \end{aligned} \tag{84}$$

In addition to the hydrodynamic forces acting on the cable, the fluid flow also acts on the towed sphere. In the next section the forces acting on the sphere are defined.

### 3.3.4 Towed Body Forces

The towed body is treated as a lumped mass located at the end of the cable. The total force acting on the towed body is given by the sum of the buoyancy, gravitational, d'Alembert and hydrodynamic forces, which follow from the Morison equation (Equation 13). The net force is

$$\mathbf{F}_b = \mathbf{F}_{b,g} + \mathbf{F}_{b,D} + \mathbf{F}_{b,I} + \mathbf{F}_{b,m}. \tag{85}$$

where $\mathbf{F}_{b,g}$ is the net force due to gravity and buoyancy, $\mathbf{F}_{b,I}$ is the inertia force, $\mathbf{F}_{b,m}$ is the force due to hydrodynamic added mass and the d'Alembert force due to the body's inertia.

The gravitational and buoyancy force $\mathbf{F}_{b,g}$ is given by

$$\mathbf{F}_{b,g} = (-\rho_f V + m_b)\mathbf{g}, \tag{86}$$

where $V$ is the volume of the body and $m_b$ is the mass.

The drag force $\mathbf{F}_{b,D}$ is

$$\mathbf{F}_{b,D} = \frac{1}{2}\rho_f(\mathbf{A}_b \circ \mathbf{C}_{D,b}) \circ |\mathbf{V}_f - \mathbf{V}_b|(\mathbf{V}_f - \mathbf{V}_b), \tag{87}$$

where $\mathbf{V}_f$ is the flow velocity and $\mathbf{V}_b$ is the velocity of the end of the cable where the towed body is located. Since the geometry of the body may vary along each axis, $\mathbf{A}_b$ is a vector of areas found by projecting that volume of the body onto the inertial planes, $\mathbf{C}_{D,b}$ is a vector of drag coefficients for each coordinate axis, and $\circ$ represents the entry-wise product.

The inertia force $\mathbf{F}_{b,I}$ is given by

$$\mathbf{F}_{b,I} = \rho_f V(\mathbf{C}_{m,b} + 1) \circ \dot{\mathbf{V}}_f, \tag{88}$$

where $\mathbf{C}_{m,b}$ is a vector of inertia coefficients for each coordinate axis.

The force due to the hydrodynamic added mass and the d'Alembert force due to the body's inertia $\mathbf{F}_{b,m}$ given by

$$\mathbf{F}_{b,m} = -(m_b + \rho_f V C_{m,b})\dot{\mathbf{V}}_b. \tag{89}$$

The equivalent generalized force $\mathbf{Q}_b$ acting on the towbody is

$$\mathbf{Q}_b = \mathbf{S}(L)^T \mathbf{F}_b = \mathbf{S}(L)^T (\mathbf{F}_{b,g} + \mathbf{F}_{b,D} + \mathbf{F}_{b,I} + \mathbf{F}_{b,m}) \tag{90}$$

The last term in Equation 90 can be rewritten as

$$\mathbf{S}(L)^T \mathbf{F}_{b,m} = -\mathbf{M}_b \ddot{\mathbf{q}} \tag{91}$$

where $\mathbf{M}_b$ is the mass matrix of the body given by

$$\mathbf{M}_b = (m_b + \rho_f V C_{m,b}) \mathbf{S}(L)^T \mathbf{S}(L) \tag{92}$$

The mass matrix of the $n$th cable element is augmented by adding the mass matrix $\mathbf{M}_b$. This augmentation is further described in Section 3.7. In the next section, the formulation of the surface contact forces is described.

## 3.4 Surface Contact

In order to model the cable-sheave and cable-winch interactions, a contact penalty is used. The cable is allowed to "penetrate" the sheave surface and the normal force is defined as a function of the relative penetration $\delta$. The normal force per unit length $\mathbf{f}_N$ acting at a single point on the element is defined using a contact force model developed by Hunt and Crossley [59], which has been used by Bulìn et al. [9] and Lugris et al. [7] to model cable-pulley interactions in ANCF cable simulations. The Hunt-Crossley contact model represents the surface as a nonlinear spring-damper with the force per unit length acting on the cable given by [59]

$$\mathbf{f}_N = k_N \delta^n (1 + D\dot{\delta}) \mathbf{u}_N \tag{93}$$

where $\mathbf{u}_N$ is the unit vector normal to the sheave surface at the point of contact, $k_N$ is the contact stiffness, $\delta$ is the relative "penetration" of the node into the surface, $D$

is a damping coefficient and $n$ is a positive constant. The value of $n$ is typically based on empirical investigations of the evolution of the contact force between two bodies during an impact and may be a function of body geometry and material properties [42]. In the present analysis, a value of $n$ of 1.5 is used based the value used by Bulín et al. [9] to model cable-sheave contact.

The relative position vector between an arbitrary "contact point" on the cable and the center of the sheave or winch $\mathbf{s}_{rel}$ is

$$\mathbf{s}_{rel} = \mathbf{s} - \mathbf{s}_w \tag{94}$$

where $\mathbf{s}$ is the position of the cable segment in the ship's body-fixed frame and $\mathbf{s}_w$ is the position of the centroid of the winch or sheave. Figure 13 shows the transformation of the contact point onto the $YZ$ plane by rotating the relative position $\mathbf{s}_{rel}$ about the winch axis of rotation. The angle between $\mathbf{s}_{rel}$ is denoted $\theta_{YZ}$ and the rotated vector, shown as a red arrow, is denoted $\mathbf{p}$. The contact forces are calculated first by transforming the relative position $\mathbf{s}_{rel}$ onto a fixed plane by rotating about the axis of rotation of the winch or sheave. The fixed plane is selected to be the $YZ$ plane. The planar contact forces are then calculated based on the two-dimensional cross-section of the surface in the $YZ$ plane. Lastly, the contact force is then transformed to the inertial frame.

The rotation angle $\theta_{YZ}$ is

$$\theta_{YZ} = \operatorname{sgn}(X_{rel}) \cos^{-1}\left(\frac{\mathbf{s}_{rel} \cdot [0 \quad 0 \quad 1]^T}{X_{rel}^2 + Z_{rel}^2}\right) \tag{95}$$

where $X_{rel}$ and $Z_{rel}$ are the components of $\mathbf{s}_{rel}$ in the $X$ and $Z$ axes. The rotated vector $\mathbf{p}$ is

$$\mathbf{p} = \mathbf{R}_y(\theta_{YZ})\mathbf{s}_{rel} \tag{96}$$

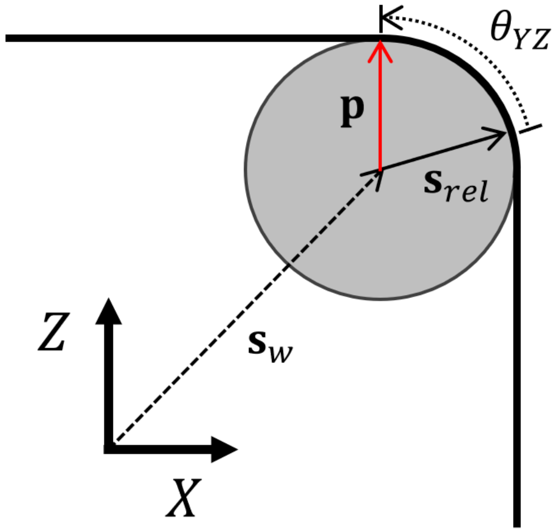

**Figure 13:** Transformation of contact point to $ZY$ plane

where $\mathbf{R}_y$ is the rotation matrix defined in Equation 25b, which rotates about the $Y$ axis. The penetration $\delta$ of the cable into the surface is

$$\delta = -(\mathbf{p} - \mathbf{p}_0) \cdot \mathbf{n} \tag{97}$$

where $\mathbf{n}$ is a unit vector normal to the contact surface in the $YZ$-plane and $\mathbf{p}_0$ is a nominal vector given by

$$\mathbf{p}_0 = [0 \quad 0 \quad r + d/2]^T \tag{98}$$

and $r$ is the radius of the winch or sheave (in the latter case, measured to the root of the sheave groove).

Figure 14 illustrates the sheave (left) and winch (right) contact surfaces. The winch is idealized as an infinite cylinder. Note that since the contact forces are applied at the cable centerline, the "contact surface", shown as a dotted line, is offset from the actual surface by the radius of the cable. The unit vector normal to the winch contact surface in the $YZ$-plane is

$$\mathbf{n}^w = [0 \quad 0 \quad 1]^T. \tag{99}$$

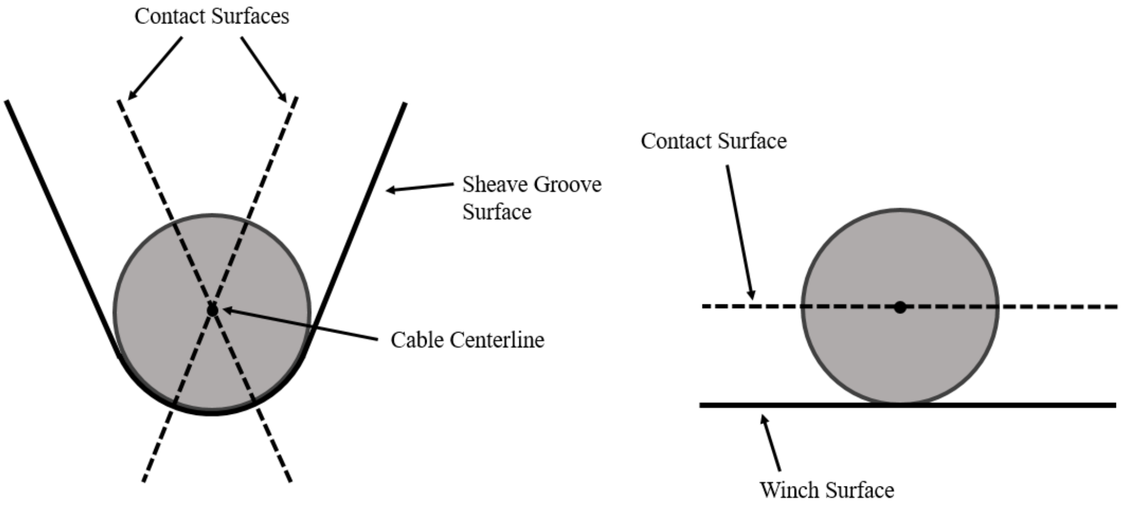

**Figure 14:** Sheave (left) and winch (right) surface cross-sections. Real surfaces are shown as solid lines. Offset contact surfaces are shown as dotted lines.

In order to accurately model the interaction between the cable and the sheave, the angled and curved surface of the sheave groove is represented by two straight lines parallel to the straight walls of the groove. Figure 14 shows the contact surfaces as dotted lines and the actual surface of the groove as a solid line. Figure 15 shows the penetration of the cable centerline below the contact surfaces. The contact surfaces, labeled $s1$ and $s2$, intersect at the point $\mathbf{p}_0$ and have normal vectors $\mathbf{n}^{s1}$ and $\mathbf{n}^{s2}$:

$$\mathbf{n}^{s1} = [\cos(\theta_g/2) \quad 0 \quad \sin(\theta_g/2)]^T \tag{100a}$$

$$\mathbf{n}^{s2} = [-\cos(\theta_g/2) \quad 0 \quad \sin(\theta_g/2)]^T \tag{100b}$$

where $\theta_g$ is the throat angle of the groove. Figure 16 illustrates the dimensions of the groove. The groove surface is idealized such that the radius of curvature of the groove $r_g$ is assumed to be equal to the radius of the cable. The two contact surfaces intersect at the center of curvature of the groove.

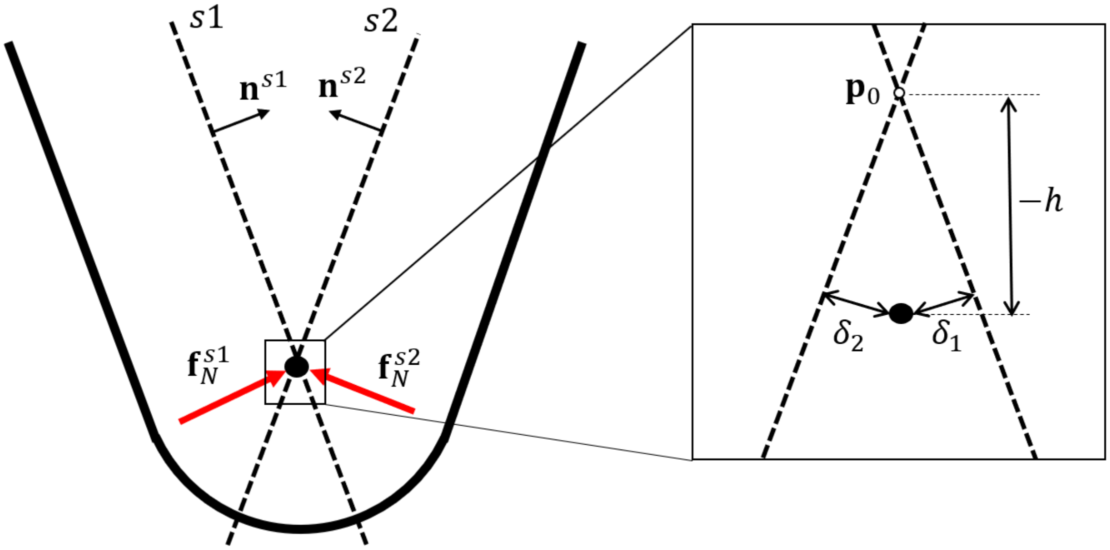

**Figure 15:** Sheave groove contact.

If the cable centerline lies below either of the dotted lines, a penalty force is produced proportional to the penetration. If the centerline lies above both lines, no normal force is applied. In Figure 16, the depth of the groove is denoted $h_g$. The distance $h$ between point $\mathbf{p}$ and $\mathbf{p}_0$ in the $Z$-axis is

$$h = (\mathbf{p} - \mathbf{p}_0) \cdot \mathbf{k}. \tag{101}$$

If the cable centerline goes above the top of the groove (i.e. $h > h_g$), then no force is applied. The unit vector $\mathbf{u}_N$ gives the direction of the force in the inertial frame, and is found by rotating the surface normal vector $\mathbf{n}$ by the inverse of the rotation $\mathbf{R}_y(\theta_{YZ})$ applied in Equation 96 and then rotating from the body-fixed frame to the inertial frame with the rotation matrix $\mathbf{R}_B^I(\alpha, \beta, \gamma)$ where $\alpha, \beta$ and $\gamma$ are the roll, pitch and yaw of the ship. The unit normal in the inertial frame is thus

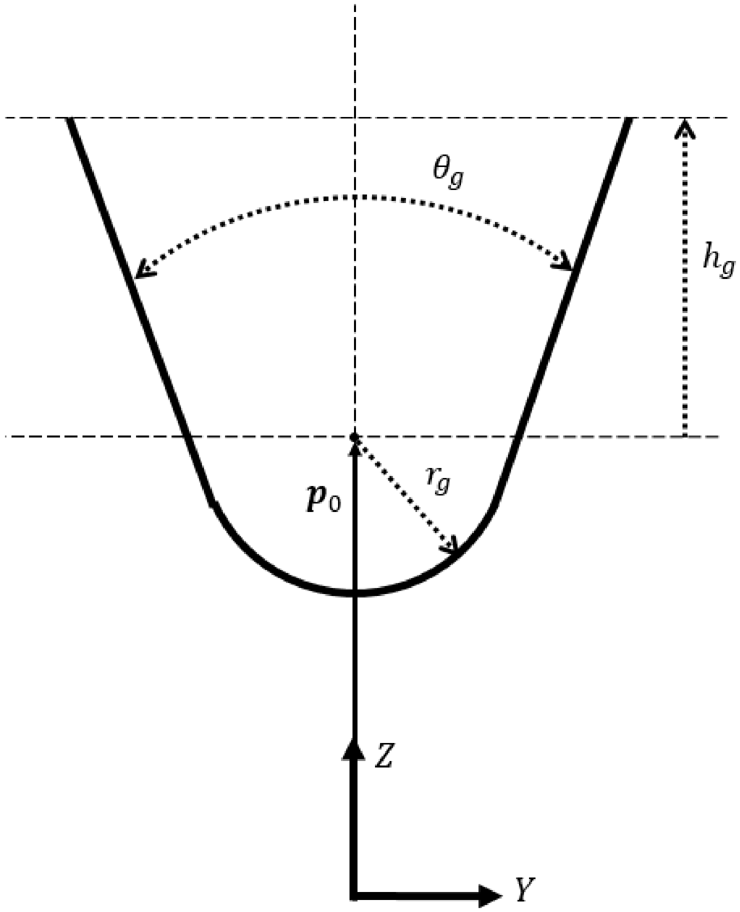

**Figure 16:** Dimensions of sheave groove.

$$\mathbf{u}_N = \mathbf{R}_B^I(\alpha, \beta, \gamma)\mathbf{R}_y(\theta_{YZ})^{-1}\mathbf{n}. \tag{102}$$

The generalized contact force $\mathbf{Q}_N$ is given by the sum of the contact forces normal to each contact surface integrated over the length of the element is

$$\mathbf{Q}_N = \sum \int_0^L \mathbf{S}(p)^T \mathbf{f}_N dp = \int_0^L \mathbf{S}(p)^T (\mathbf{f}_N^{s1} + \mathbf{f}_N^{s2} + \mathbf{f}_N^{w}) dp. \tag{103}$$

where the superscripts indicate the contact surface. The normal force per unit length is evaluated at $N_I$ discrete points points per element and the generalized contact force is approximated using a numerical quadrature. An element can have no contact with the surface, partial contact or full contact. For these three cases, the quadrature is

$$\mathbf{Q}_N = \begin{cases} \mathbf{0}_{12\times 1}, & \text{if no contact} \\ \frac{L}{N_I}\sum_{j=1}^{N_I}\mathbf{S}(p_j)^T[\sum w_j \mathbf{f}_N(p_j)] + \mathbf{Q}_N^*, & \text{if partial contact} \\ \frac{L}{N_I}\sum_{j=1}^{N_I}\mathbf{S}(p_j)^T[\sum w_j \mathbf{f}_N(p_j)], & \text{if full contact.} \end{cases} \tag{104}$$

where $\mathbf{0}_{12\times 1}$ is a $12 \times 1$ null matrix, $w_j$ is the quadrature weight. Figure 17 illustrates the partial contact case and the equivalent undeformed element. The contact surface is shown as a dotted line. The integration points are shown as open circles, except for the element nodes which are shown as close circles. The arc parameter $p$ is measured from the first node ($j = 1$). The index $j$ of the last integration point that has a positive penetration (i.e. closed contact) is denoted $j^*$.

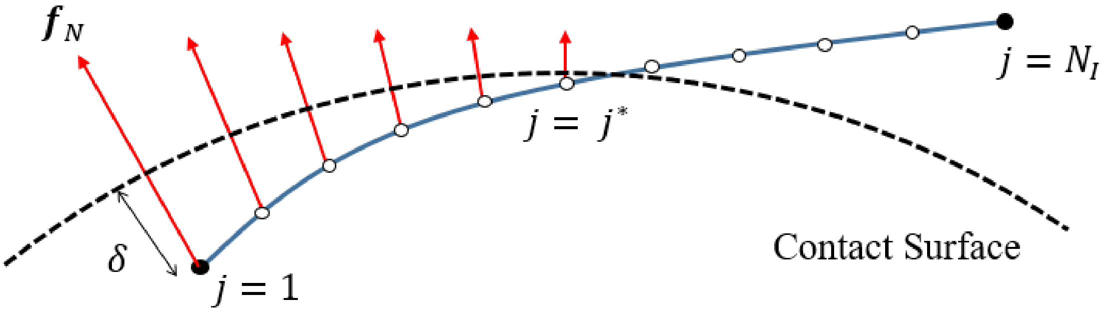

**Figure 17:** Sheave groove contact forces at discrete integration points.

To evaluate the numerical quadrature in Equation 104, the trapezoidal rule is used to define the quadrature weights which are

$$w_j = \begin{cases} 0, & \text{if } \delta_j \leq 0 \text{ or } h_j \geq h_g \\ 0.5, & \text{if } \delta_j > 0 \text{ and } h_j \geq h_g \text{ and } j \in \{1, j^*, N_I\} \\ 1, & \text{if } \delta_j > 0 \text{ and } h_j \geq h_g \text{ and } j \in \{2, 3, ..., N_I - 1\}\backslash j^*. \end{cases} \tag{105}$$

Note that each contact surface has a distinct set of quadrature weights.

In the partial contact case, the additional generalized force $\mathbf{Q}_N^*$ account for the force acting on the interval between point $j^*$ and the point where the cable intersects the contact surface:

$$\mathbf{Q}_N^* = 0.5|p^* - p_0| \left[\mathbf{S}(p^*)^T \mathbf{f}_N(p^*) + \mathbf{S}(p_0)^T \mathbf{f}_N(p_0)\right] \tag{106}$$

where $p^*$ is the value of the arc parameter $p$ at point $j^*$ and $p_0$ is the arc parameter at the intersection point.

In this section, the formulation of the normal contact forces between the cable and the sheave and winch surfaces was described. Since the focus of the research is on examining variations in normal contact forces between the cable and sheave, the tangential contact forces were neglected. The sheave was thus idealized as having a frictionless surface or, equivalently, having zero rotational inertia. In the next section, the kinematic constraint forces which constrain the end of the cable to the surface of the winch are described.

## 3.5 Kinematic Constraints

The end of the cable is constrained to an arbitrary point on the surface of the winch, such that the rotation of the winch will reel the cable in or out. The augmented (Lagrange multiplier) formulation [60] is used to define the generalized constraint force. In the augmented formulation, a constraint force is applied to each constrained node in order to satisfy a constraint equation of the form

$$\mathbf{\Phi}(\mathbf{q}, t) = \mathbf{0}. \tag{107}$$

The force $\mathbf{Q}_c$ required to satisfy the constraint $\mathbf{\Phi}$ can then defined by introducing a vector of Lagrange multipliers $\lambda$:

$$\mathbf{Q}_c = -{\mathbf{\Phi}_{\mathbf{q}}}^T \lambda \tag{108}$$

The equations of motion from Equation 30 become differential algebraic equations of the form

$$\begin{aligned} \mathbf{M}\ddot{\mathbf{q}} + \mathbf{Q}_{\text{int}} - \mathbf{Q}_{\text{ext}} + {\mathbf{\Phi}_{\mathbf{q}}}^T \lambda = 0 \\ \mathbf{\Phi} = 0 \end{aligned} \tag{109}$$

where $\mathbf{M}$ is the mass matrix of the system, $\mathbf{Q}_{int}$ is the generalized internal force and $\mathbf{Q}_{ext}$ is the sum of external generalized forces, excluding the constraint force $\mathbf{Q}_c$.

It is necessary to solve for both the system accelerations $\ddot{\mathbf{q}}$ and the Lagrange multipliers $\lambda$, thus the number of degrees of freedom increases by the number of constraints. An additional set of governing equations is derived by taking the second derivative of Equation 107 with respect to time gives

$$\mathbf{\Phi}_{tt} = -\mathbf{\Phi}_{\mathbf{q}}\ddot{\mathbf{q}} - (\mathbf{\Phi}_{\mathbf{q}}\dot{\mathbf{q}})_q\dot{\mathbf{q}} - 2(\mathbf{\Phi}_q)_t\dot{\mathbf{q}}. \tag{110}$$

Note that the subscripts $t$ and $tt$ denote the first and second *partial* derivatives with respect to time, while an over-dot denotes the *total* derivative with respect to time. Furthermore, denoting

$$\mathbf{b} := -\mathbf{\Phi}_{tt} - (\mathbf{\Phi}_{\mathbf{q}}\dot{\mathbf{q}})_{\mathbf{q}}\dot{\mathbf{q}} - 2(\mathbf{\Phi}_{\mathbf{q}})_t\dot{\mathbf{q}}, \tag{111}$$

the constraint is expressed at the acceleration level as

$$\mathbf{\Phi}_{\mathbf{q}}\ddot{\mathbf{q}} = \mathbf{b}. \tag{112}$$

Equation 112 assumes that the constraint equations are satisfied exactly, which is only true in an ideal computational environment. Due to the error inherent to the numerical solution of the equations of motion, the above method is numerically unstable unless corrections are applied to prevent accumulation of error or "constraint drift" [61].

A well-known method for "stabilization" or "regularization" of the constraint is Baumgarte's stabilization method [62], wherein the equation

$$\ddot{\mathbf{\Phi}} + 2a_1\dot{\mathbf{\Phi}} + a_2^2\mathbf{\Phi} = 0 \tag{113}$$

is to be satisfied instead of $\ddot{\mathbf{\Phi}} = 0$. The additional terms introduce feedback, similar to a PD controller, if the solution drifts from the constrained value. The variable $\mathbf{b}$ in Equation 112 is then replaced with

$$\mathbf{b}' = \mathbf{b} - 2a_1\dot{\mathbf{\Phi}} - a_2^2\mathbf{\Phi} \tag{114}$$

where $a_1$ and $a_2$ are chosen constants. The governing equations can now be written as

$$\begin{bmatrix} \mathbf{M} & \mathbf{\Phi_q} \\ \mathbf{\Phi_q} & 0 \end{bmatrix} \begin{bmatrix} \ddot{\mathbf{q}} \\ -\lambda \end{bmatrix} = \begin{bmatrix} \mathbf{Q}_{\text{ext}} - \mathbf{Q}_{\text{int}} \\ \mathbf{b}' \end{bmatrix} \tag{115}$$

It is desirable to eliminate the Lagrange multipliers $\lambda$ from Equation 115 to keep the equations of motion as explicit ODEs to facilitate the use of ODE solvers, such as MATLAB's *ode15s*. By rearranging Equation 115, the Lagrange multipliers can be written

$$\lambda = \left[\mathbf{\Phi}_q\mathbf{M}^{-1}{\mathbf{\Phi}_q}^T\right]^+ (\mathbf{\Phi_q}\mathbf{a} - \mathbf{b}') \tag{116}$$

where $^+$ represents the Moore-Penrose pseudo-inverse and $\mathbf{a}$ is the associated accelerations of the unconstrained system

$$\mathbf{a} = \mathbf{M}^{-1}(\mathbf{Q}_{\text{ext}} - \mathbf{Q}_{\text{int}}) \tag{117}$$

Combining Equation 116 with Equation 108, the generalized constraint force becomes

$$\mathbf{Q}_c = -\mathbf{\Phi}_q{}^T \left[\mathbf{\Phi}_q \mathbf{M}^{-1} \mathbf{\Phi}_q{}^T\right]^+ (\mathbf{\Phi}_\mathbf{q}\mathbf{a} - \mathbf{b}') \tag{118}$$

The equations of motion can again be written as explicit ODEs:

$$\mathbf{M}\ddot{\mathbf{q}} + \mathbf{Q}_{\text{int}} - \mathbf{Q}_{\text{ext}} - \mathbf{Q}_c = 0. \tag{119}$$

One end of the cable is constrained to the surface of the winch using the kinematic constraint

$$\mathbf{\Phi} = \mathbf{r}^{(1)}(0) - \mathbf{r}_{CG} - \mathbf{R}_B^I(\alpha, \beta, \gamma)(\mathbf{s}_w + \mathbf{R}_y(\phi) r_w \mathbf{k}) = 0 \tag{120}$$

where $\mathbf{r}^{(1)}(0)$ is the position of the first node of the first element, $\mathbf{r}_{CG}$ is the position of the center of gravity of the ship, $\mathbf{s}_w$ is the position of the winch in the body-fixed coordinate frame, $\mathbf{R}_B^I$ is the rotation matrix from the ship's body frame to the inertial frame, $\mathbf{R}_y$ is the rotation matrix corresponding to the winch rotation of $\phi$ about its axis and $\mathbf{k} = [0 \quad 0 \quad 1]^T$ is the versor of the $Z$ axis. The constraint is applied using Baumgarte's stabilization method where

$$\dot{\mathbf{\Phi}} = \dot{\mathbf{r}}^{(1)}(0) - \dot{\mathbf{r}}_{CG} - \frac{d\mathbf{R}_B^I}{dt}(\mathbf{s}_w + \mathbf{R}_y(\phi) r_w \mathbf{k}) - \mathbf{R}_B^I \frac{d\mathbf{R}_y(\phi)}{dt} r_w \mathbf{k} \tag{121}$$

and

$$\mathbf{b} = \ddot{\mathbf{r}}_{CG} + \frac{d^2\mathbf{R}_B^I}{dt^2}(\mathbf{s}_w + \mathbf{R}_y(\phi)r_w\mathbf{k}) + 2\frac{d\mathbf{R}_B^I}{dt}\frac{d\mathbf{R}_y(\phi)}{dt}r_w\mathbf{k} + \mathbf{R}_B^I\frac{d^2\mathbf{R}_y(\phi)}{dt^2}r_w\mathbf{k}. \quad (122)$$

are substituted into Equation 114.

In addition to the constraint applied to the end of the cable, each element must also be constrained to its neighbouring elements to provide connectivity between elements. The next section describes the formulation of the inter-element connectivity.

## 3.6 Inter-element Connectivity

Each element making up the cable can be treated as one body of a multibody system. Two coincident cable nodes must be constrained, such that the cable is continuous and smooth along its length. To connect adjacent nodes together and to make the slope of the cable continuous, the position vectors $\mathbf{r}$ and gradient vectors $\mathbf{r}_p$ of adjacent nodes are constrained by the inter-element constraint equation

$$\mathbf{\Phi}^{(i,i+1)} = \begin{bmatrix} \mathbf{r}^{(i)}(L) - \mathbf{r}^{(i+1)}(0) \\ \mathbf{r}_p^{(i)}(L) - \mathbf{r}_p^{(i+1)}(0) \end{bmatrix} = \begin{bmatrix} \mathbf{0} \\ \mathbf{0} \end{bmatrix} \quad (123)$$

where $i$ and $i+1$ are the indices of the elements being constrained and $L$ is the unstretched element length. Figure 18 shows two adjacent elements with the position vectors $\mathbf{r}^{(i)}(L)$ and $\mathbf{r}^{(i+1)}(0)$ shown as solid arrows and the slope vectors $\mathbf{r}_p^{(i)}(L)$ and $\mathbf{r}_p^{(i+1)}(0)$ indicated by dashed arrows.

For these constraints, the augmented formulation used in Section 3.5 would require solving for all 12 degrees of freedom per element. By the definition of the constraints in Equation 123, two constrained nodes are coincident and have the same slope. Therefore the generalized coordinates of the two nodes are expected to have the same value and half of the constrained coordinates are redundant. An alternative method to

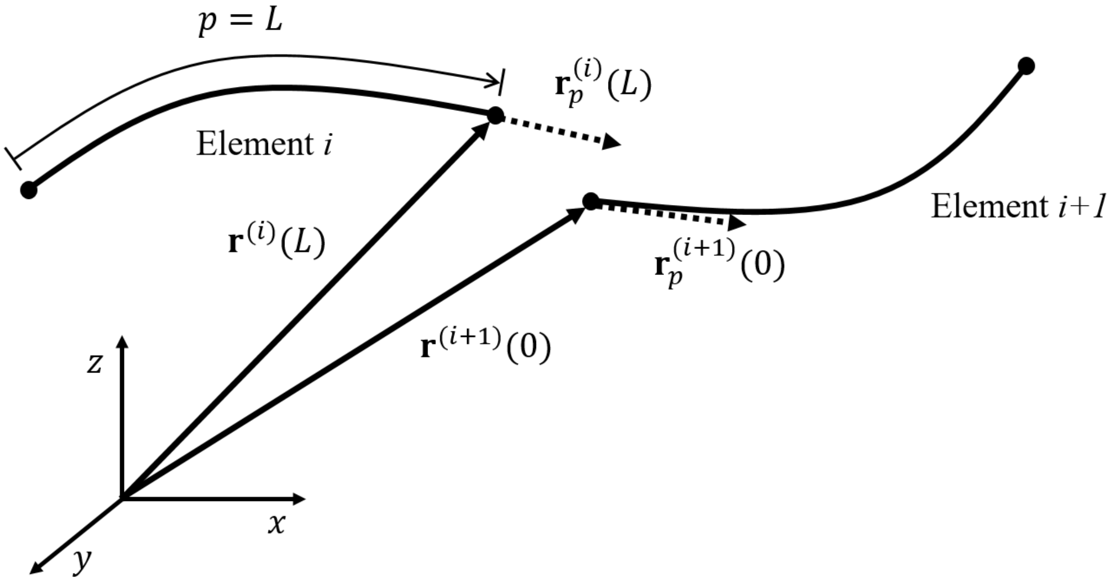

**Figure 18:** Adjacent elements with constrained coordinate vectors

the augmented formulation is the embedding technique [60] which serves to eliminate the redundant coordinates, thereby improving the computational efficiency of the simulation as well as eliminating numerical error in the constraints.

The vector $\mathbf{q}^{(i,i+1)}$, which contains all generalized coordinates of elements $i$ and $i+1$ is

$$\mathbf{q}^{(i,i+1)} = \begin{bmatrix} \mathbf{q}^{(i)} \\ \mathbf{q}^{(i+1)} \end{bmatrix} \tag{124}$$

The generalized coordinate vector $\mathbf{q}$ for a single element is given in Equation 27. The combined coordinate vector $\mathbf{q}^{(i,i+1)}$ is partitioned by defining a set of independent coordinates $\mathbf{q}_i$ and the remaining dependent coordinates $\mathbf{q}_d$, thus

$$\mathbf{q}^{(i,i+1)} = \begin{bmatrix} \mathbf{q}_i{}^T & \mathbf{q}_d{}^T \end{bmatrix}^T . \tag{125}$$

The *dependent* coordinates are selected to be the position and gradient vector of the first node of element $i+1$

$$\mathbf{q}_d = \begin{bmatrix} \mathbf{r}^{(i+1)}(0) \\ \mathbf{r}_p^{(i+1)}(0) \end{bmatrix} \tag{126}$$

and the independent coordinates are

$$\mathbf{q}_i = \begin{bmatrix} \mathbf{r}^{(i)}(0) \\ \mathbf{r}_p^{(i)}(0) \\ \mathbf{r}^{(i)}(L) \\ \mathbf{r}_p^{(i)}(L) \\ \mathbf{r}^{(i+1)}(L) \\ \mathbf{r}_p^{(i+1)}(L) \end{bmatrix} . \tag{127}$$

The Jacobian of $\mathbf{\Phi}^{(i,i+1)}$ with respect to the combined coordinate vector $\mathbf{q}^{(i,i+1)}$ is

$$\mathbf{\Phi}_q^{(i,i+1)} = \begin{bmatrix} \mathbf{0} & \mathbf{0} & \mathbf{I} & \mathbf{0} & -\mathbf{I} & \mathbf{0} & \mathbf{0} & \mathbf{0} \\ \mathbf{0} & \mathbf{0} & \mathbf{0} & \mathbf{I} & \mathbf{0} & -\mathbf{I} & \mathbf{0} & \mathbf{0} \end{bmatrix} \tag{128}$$

where $\mathbf{0}$ is a $3 \times 3$ null matrix and $\mathbf{I}$ is a $3 \times 3$ identity matrix. The Jacobian matrix $\mathbf{\Phi}_q^{(i,i+1)}$ is also partitioned into two components $\mathbf{\Phi}_{q,i}$ and $\mathbf{\Phi}_{q,d}$ which contain the columns of $\mathbf{\Phi}_q^{(i,i+1)}$ corresponding to the independent and dependent coordinates respectively. The constraint equation from Equation 123 can then be rewritten

$$\mathbf{\Phi}_{q,i}\mathbf{q}_i + \mathbf{\Phi}_{q,d}\mathbf{q}_d = 0 \tag{129}$$

Combining Equations 125 and 129, the following expression which relates the combined coordinate vector $\mathbf{q}^{(i,i+1)}$ to the independent coordinates $\mathbf{q}_i$ is obtained:

$$\mathbf{q}^{(i,i+1)} = \mathbf{B}\mathbf{q}_i, \tag{130}$$

where $\mathbf{B}$ is a transformation matrix given by

$$\mathbf{B} = \begin{bmatrix} \mathbf{I} \\ -\boldsymbol{\Phi}_{q,d}{}^{-1}\boldsymbol{\Phi}_{q,i} \end{bmatrix} \tag{131}$$

and $\mathbf{I}$ is an identity matrix.

The formulation shown above constrains two consecutive elements. In the full cable model, each element is constrained to its neighbouring elements. The method described in this section can be expanded to the full model by defining a constraint matrix $\boldsymbol{\Phi}^{(1,2,...,N_E)}$ which includes the constraints for all elements $i = 1, 2, ..., N_E$, where $N_E$ is the number of elements and collecting the generalized coordinates for all elements in a single vector $\mathbf{q}^{(1,2,...,N_E)}$. The constraint matrix $\boldsymbol{\Phi}^{(1,2,...,N_E)}$ and coordinate vector $\mathbf{q}^{(1,2,...,N_E)}$ are then partitioned into independent and dependent components and the transformation matrix $\mathbf{B}$ is determined. From an initial $12N_E$ degrees of freedom, the embedding technique reduces the system to $6N_E + 6$ independent coordinates.

A reduced set of governing equations containing only the independent coordinates can be defined as

$$(\mathbf{B}^T\overline{\mathbf{M}}\mathbf{B})\ddot{\mathbf{q}}_i + \mathbf{B}^T(\overline{\mathbf{Q}}_{\text{int}} - \overline{\mathbf{Q}}_{\text{ext}} - \overline{\mathbf{Q}}_c) = 0 \tag{132}$$

where $\overline{\mathbf{M}}$ is the “master” mass matrix, which is a block diagonal matrix containing the mass and added mass matrices of each element, $\overline{\mathbf{Q}}_{\text{int}}$ and $\overline{\mathbf{Q}}_{\text{ext}}$ are the master internal and external generalized forces, and $\overline{\mathbf{Q}}_c$ is the master constraint force [60]. The following section outlines the formulation of the master mass matrix and generalized forces, as well as the simulation procedure.

## 3.7 System Assembly and Simulation Procedure

The total mass matrix for each element is found by summing the mass and added mass matrices, $\mathbf{M}^{(i)}$ and $\mathbf{M}_A^{(i)}$, from Equations 9 and 74, respectively, as well as the towed body mass matrix $\mathbf{M}_b$ from Equation 92 for the final element. The elemental mass matrices are then assembled block-diagonally to form the master or system mass matrix $\overline{\mathbf{M}}$:

$$\overline{\mathbf{M}} = \begin{bmatrix} \mathbf{M}^{(1)} + \mathbf{M}_A^{(1)} & \mathbf{0} & \dots & \mathbf{0} \\ & \mathbf{M}^{(2)} + \mathbf{M}_A^{(2)} & & \mathbf{0} \\ & & \ddots & \vdots \\ sym. & & & \mathbf{M}^{(N_E)} + \mathbf{M}_A^{(N_E)} + \mathbf{M}_b \end{bmatrix} \tag{133}$$

The master internal force vectors $\overline{\mathbf{Q}}_{\text{int}}$ and $\overline{\mathbf{Q}}_{\text{ext}}$ is formed by assembly the elemental vectors $\mathbf{Q}_{\text{int}}^{(i)}$ (Equation 31) and $\mathbf{Q}_{\text{ext}}^{(i)}$ (Equation 76) vertically and adding the external generalized towbody force $\mathbf{Q}_b$ (Equation 90) acting on the final element:

$$\overline{\mathbf{Q}}_{\text{int}} = \begin{bmatrix} \mathbf{Q}_{\text{int}}^{(1)} \\ \mathbf{Q}_{\text{int}}^{(2)} \\ \vdots \\ \mathbf{Q}_{\text{int}}^{(N_E-1)} \\ \mathbf{Q}_{\text{int}}^{(N_E)} \end{bmatrix} \quad \text{and} \quad \overline{\mathbf{Q}}_{\text{ext}} = \begin{bmatrix} \mathbf{Q}_{\text{ext}}^{(1)} \\ \mathbf{Q}_{\text{ext}}^{(2)} \\ \vdots \\ \mathbf{Q}_{\text{ext}}^{(N_E-1)} \\ \mathbf{Q}_{\text{ext}}^{(N_E)} + \mathbf{Q}_b \end{bmatrix}. \tag{134}$$

The constraint force $\mathbf{Q}_c$ from Equation 118 is applied only to the first element, thus the master generalized constraint force is

$$\overline{\mathbf{Q}}_{\mathrm{c}} = \begin{bmatrix} \mathbf{Q}_c \\ \mathbf{0}_{12\times 1} \\ \vdots \\ \mathbf{0}_{12\times 1} \\ \mathbf{0}_{12\times 1} \end{bmatrix} \tag{135}$$

where $\mathbf{0}_{12\times 1}$ is a $12 \times 1$ null vector.

Furthermore, an additional degree of freedom is added representing the winch rotation $\phi$. The acceleration of the winch is given by a PD control equation

$$\ddot{\phi} = k_1(\phi_{SP} - \phi) + k_2(\dot{\phi}_{SP} - \dot{\phi}) \tag{136}$$

where $k_1$ and $k_2$ are chosen constants and $\phi_{SP}$ is the set-point. The winch rotations can then be used to evaluate the constraint force $\mathbf{Q}_c$, which satisfies the constraint given in Equation 120.

The complete set of ODEs are therefore

$$\begin{bmatrix} \ddot{\mathbf{q}}_i \\ \ddot{\phi} \end{bmatrix} = \begin{bmatrix} (\mathbf{B}\overline{\mathbf{M}}\mathbf{B})^{-1}\mathbf{B}(\overline{\mathbf{Q}}_{\mathrm{ext}} - \overline{\mathbf{Q}}_{\mathrm{int}} + \overline{\mathbf{Q}}_c) \\ k_1(\phi_{SP} - \phi) + k_2(\dot{\phi}_{SP} - \dot{\phi}) \end{bmatrix}. \tag{137}$$

The ODEs are solved using MATLAB's stiff ODE solver *ode15s.* The procedure used to stimulate the cable motion is as follows:

1. The simulation parameters are defined, including:
   (a) the time span,
   (b) the cable discretization, i.e. the number of elements $N_E$ and length $L^{(i)}$ of each element
   (c) the initial conditions $\mathbf{q}(0)$, $\dot{\mathbf{q}}(0)$, $\phi(0)$ and $\dot{\phi}(0)$,
   (d) the constraint Jacobian $\mathbf{\Phi}_{\mathbf{q}}$, and

   (e) the embedding matrix $\mathbf{B}$.

2. The system parameters, including the cable properties, system dimensions, and fluid properties are defined. The ship motion, including the position and velocity of the center-of-gravity and the roll, pitch and yaw angles and their derivatives are defined as a function of time. Constant matrices such as the mass matrices $\mathbf{M}^{(i)}$ (Equation 9) and gravitational force vectors $\mathbf{Q}_e^{(i)}$ (Equation 35) can also be evaluated for each element.

3. The ODE solver is called with the following inputs: the array of initial conditions, the time span, and a structure containing the system parameters and constant matrices.

4. The ODE solver iterates over an "ODE function" which takes an array input of $[\mathbf{q}_i^T \quad \dot{\mathbf{q}}_i^T \quad \phi \quad \dot{\phi}]$ and performs the following steps:
   (a) Evaluates the generalized longitudinal elastic force $\mathbf{Q}_l$ (Equation 46), transverse elastic force $\mathbf{Q}_t$ (Equation 52) and the generalized damping force $\mathbf{Q}_d$ (Equation 55) for each element,
   (b) Evaluates the generalized external hydrodynamic force $\mathbf{Q}_h$ (Equation 78) and contact force $\mathbf{Q}_N$ (Equation 104) for each element and the towed body force $\mathbf{Q}_b$ (Equation 90),
   (c) Assembles the master internal and external generalized force vectors $\overline{\mathbf{Q}}_{\text{int}}$ and $\overline{\mathbf{Q}}_{\text{ext}}$,
   (d) Evaluates the added mass matrix $\mathbf{M}_a$ (Equation 81-83) for each element and the towbody mass matrix $\mathbf{M}_{a,b}$ (Equation 92),
   (e) Assembles the master mass matrix $\overline{\mathbf{M}}$,
   (f) Evaluates the set-point $\phi_{SP}$ and its derivative $\dot{\phi}_{SP}$ based on the chosen set-point algorithm and the ship motion data at the current time-step,

(g) Evaluates the constraint force $\mathbf{Q}_c$ (Equation 118) and master constraint force $\overline{\mathbf{Q}}_c$,

(h) Solves for $\dot{\mathbf{q}}_i$ and $\ddot{\phi}$ by Equation 137.

The ODE function returns the array $[\dot{\mathbf{q}}_i^T \quad \ddot{\mathbf{q}}_i^T \quad \dot{\phi} \quad \ddot{\phi}]$ to the ODE solver.

5. The ODE solver returns the array $[\mathbf{q}_i^T \quad \dot{\mathbf{q}}_i^T \quad \phi \quad \dot{\phi}]$ for each time step.

## 3.8 Summary

In this chapter, a model of a towed-cable system with winch and sheave contact was described, contributing toward the first objective of this thesis. The formulation of the following elements of the finite element cable model were shown:

1. the ANCF finite element, the mass matrix, the internal elastic forces and the internal damping force,
2. the external hydrodynamic forces acting on the cable and towbody,
3. the external contact forces,
4. the kinematic constraint force which constrains the end of the cable to the winch,
5. the inter-element connectivity using the embedding technique.

Finally, the simulation procedure was outlined.

The model was developed to predict the cable dynamics of a towed body system with ship motion and active heave compensation. The outputs of the simulation can be used to examine variations in the cable tension and contact forces during the motion. In future work, the simulated tension and contact forces could be used to examine and predict detachment of the cable from the sheave. Also, the motion of the towed body can be simulated and used to evaluate the performance of heave compensation algorithms. A contribution of this thesis shown in this chapter is the description of the contact between the cable and the sheave groove. The model incorporates the three-dimensional geometry of the groove in order to accurately represent the contact forces as the ship moves and rotates.

In the next chapter, the model will be validated based on small scale experimental measurements of towbody motion and cable tension.

# 4 Experimental Validation

In this chapter, the experimental validation of the cable model is described. Two experiments were performed for small scale pulley systems with an external load attached to one end of the cable. In the first experiment the pulley is stationary and the experimental cable tension and wrap angle of the cable around the pulley were compared to the simulated results. Preliminary results from the first experiment were published in the paper entitled "Cable-Pulley Interaction with Dynamic Wrap Angle Using the Absolute Nodal Coordinate Formulation" by C. Westin and R.A. Irani in the Proceedings of the 4th International Conference of Control, Dynamic Systems, and Robotics (CDSR'17) [63] and received a Best Paper award. In the second experiment, the pulley was actuated to simulate ship motion and the recorded and simulated cable tension were compared. Lastly, experimental towbody motion for a small scale towed cable system with active heave compensation obtained by Calnan [2] was utilized to validate the model.

## 4.1 Cable-Pulley System with Stationary Pulley

The first experiment consisted of a stationary pulley supporting a nylon fibre rope pinned at one and and attached to a rigid load at the other end. Figure 19 illustrates the system. The load was released from an initial angle, measured from the horizontal, with the rope taut. The load was then allowed to swing.

The cable simulation was reduced to two dimensions since the cable and load undergo planar motion only. Since the rotational inertia of the external load is significant in this system, the lumped formulation of the attached body described in Section 3 is insufficient to capture the rigid body dynamics. Thus, the simulation was modified by adding a linear elastic element representing the load. The element is described by two coordinate vectors or four translational degrees of freedom: $\mathbf{r}_P = [x_P \; y_P]$ representing

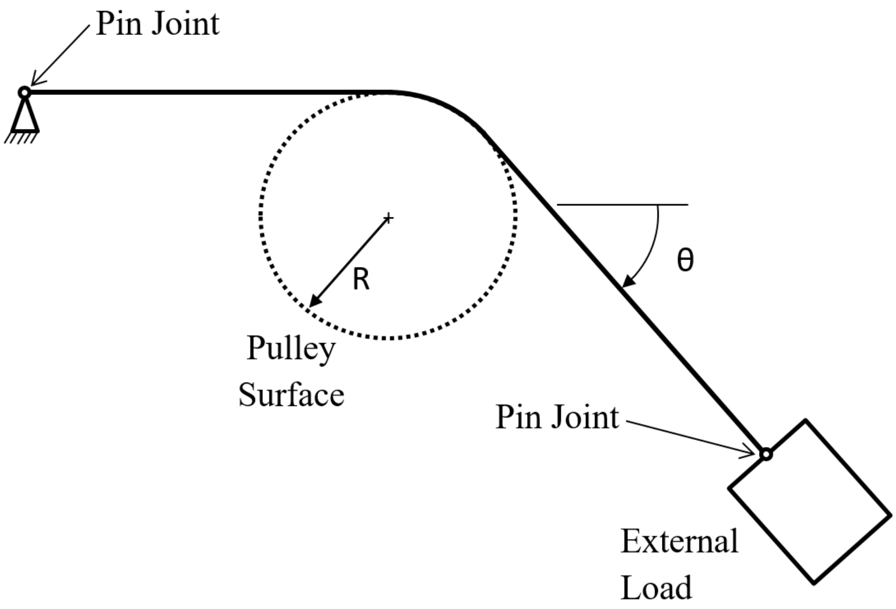

**Figure 19:** Illustration of cable-pulley system with static pulley.

the position of the attachment point and $\mathbf{r}_I = [x_I \; y_I]$ representing the position of the center of inertia of the body. The mass matrix for the load $\mathbf{M}_L$, derived by Jalon and Bayo [49], is implemented here as

$$\mathbf{M}_L = \begin{bmatrix} 2m_L(1 - \frac{L_{P,G}}{L_{P,I}})\mathbf{I} & m_L(\frac{L_{P,G}}{L_{P,I}} - 1)\mathbf{I} \\ m_L(\frac{L_{P,G}}{L_{P,I}} - 1)\mathbf{I} & m_L\mathbf{I} \end{bmatrix}, \tag{138}$$

where where $m_L$ is the mass of the load, $L_{P,G}$ and $L_{P,I}$ are the distances between the cable attachment point and the centers of gravity and inertia, respectively, and $\mathbf{I}$ is a 2x2 identity matrix. The internal elastic force for the linear element is

$$\mathbf{Q}_{L,int} = k_L \frac{|\mathbf{r}_p - \mathbf{r}_I| - L_{P,I}}{L_{P,I}} \begin{bmatrix} 1 & 0 & -1 & 0 \\ 0 & 1 & 0 & -1 \\ -1 & 0 & 1 & 0 \\ 0 & -1 & 0 & 1 \end{bmatrix} \begin{bmatrix} x_P \\ y_P \\ x_I \\ y_I \end{bmatrix} \tag{139}$$

where $k_L$ is the tensile stiffness of the load. Additionally, a spherical constraint was used to constrain the end of the cable to the attachment point on the load.

During the experiment, the tension was measured using a 100 kg load cell. The angle of the rope relative to the horizontal axis was measured via a vision system to determine the wrap angle of the cable on the pulley. Colored markers were placed at two points along the rope and camera footage of the rope motion was collected at 60 frames per second. Using the image processing tools in MATLAB, the recorded frames were converted to Hue-Saturation-Value (HSV) colormaps, then each pixel with a hue and saturation value within predefined ranges was identified. The coordinates of each matching pixel were then averaged to find the centroid of each marker. The orientation of the line connecting the centroids of the two markers relative to the horizontal was then calculated. The calculated angle approximates the wrap angle of the cable around the pulley. A low-pass Butterworth filter was applied to both the tension and angle measurements.

The experiment was repeated for varying loads and initial wrap angles. The parameters of the system recorded during the experiments are given in Table 1. These values were also used to perform the corresponding simulations. The elastic modulus of a nylon fiber has a value of approximately 2 GPa [64]. Due to the fibrous construction of the rope, the bending stiffness is very small. Similar to the convergence shown by Bulín et al. [9], the second moment of area was selected by lowering the value until the contact forces converged to a constant distribution and was held constant at $4.0 \times 10^{-14}$ m$^4$ for all simulations. The rope length was measured along the centerline from the top of the pulley to the load attachment point and had a value of 44 cm. A minimal value of the damping coefficient $c$ of $1 \times 10^{-3}$ Ns was selected by increasing the coefficient until the high frequency vibration modes of the cable were attenuated and stability of the numerical solution was obtained.

A convergence study was performed using the parameters listed for Configuration 1 in Table 1. Simulations were performed to determine the cable tension and wrap

**Table 1:** Model parameters for cable-pulley experiment with stationary pulley.

| Configuration | 1 | 2 | 3 |
|---|---|---|---|
| Pulley radius, $R$ (cm) | 4.62 | 4.62 | 4.62 |
| Rope diameter, $d$ (cm) | 0.884 | 0.884 | 0.884 |
| Rope linear density (g/cm) | 0.59 | 0.59 | 0.59 |
| Rope modulus of elasticity, $E$ (GPa) | 2.0 | 2.0 | 2.0 |
| Rope second moment of area, $I$ (m$^4$) | $4.0 \times 10^{-14}$ | $4.0 \times 10^{-14}$ | $4.0 \times 10^{-14}$ |
| External load mass, $m_L$ (kg) | 9.43 | 18.50 | 27.57 |
| External load length, $L_{P,I}$ (cm) | 26.9 | 25.9 | 24.5 |
| External load length, $L_{P,G}$ (cm) | 25.8 | 24.5 | 23.2 |
| Initial wrap angle, $\theta_0$ (deg) | 34.9 | 40.4 | 49.4 |

angle while varying the number of elements from 10 to 25 elements. Each simulation was performed with 10 integration points per element. Figure 20 shows the simulated wrap angle (left) and cable tension (right) for the first 1 s of motion. Increasing the mesh beyond 10 elements had no significant effect on the simulated wrap angle or cable tension, thus ten elements were used for the final simulations.

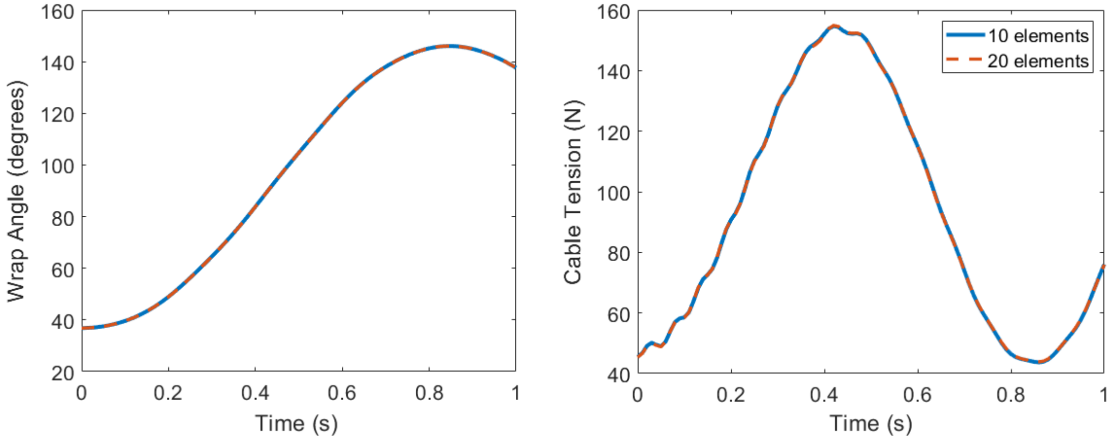

**Figure 20:** Simulated wrap angle (left) and cable tension (right) with 10 and 20 elements.

For each configuration, the simulation was performed for 10 seconds of motion. Figure 21 compares the experimental and simulation wrap angles for configuration 1. The standard deviation of the error was determined to be 1.37 degrees with a maximum error of 2.77 degrees as the wrap angle varied between 36.7 and 146 degrees. Similarly, the standard deviation of the error was 3.73 degrees with a maximum error of 9.24 degrees as the wrap angle varied between 43.3 and 139 degrees for Configuration 2. The standard deviation of the error was 2.14 degrees with a maximum error of 4.30 degrees as the wrap angle varied between 52.4 and 129 degrees for Configuration 3.

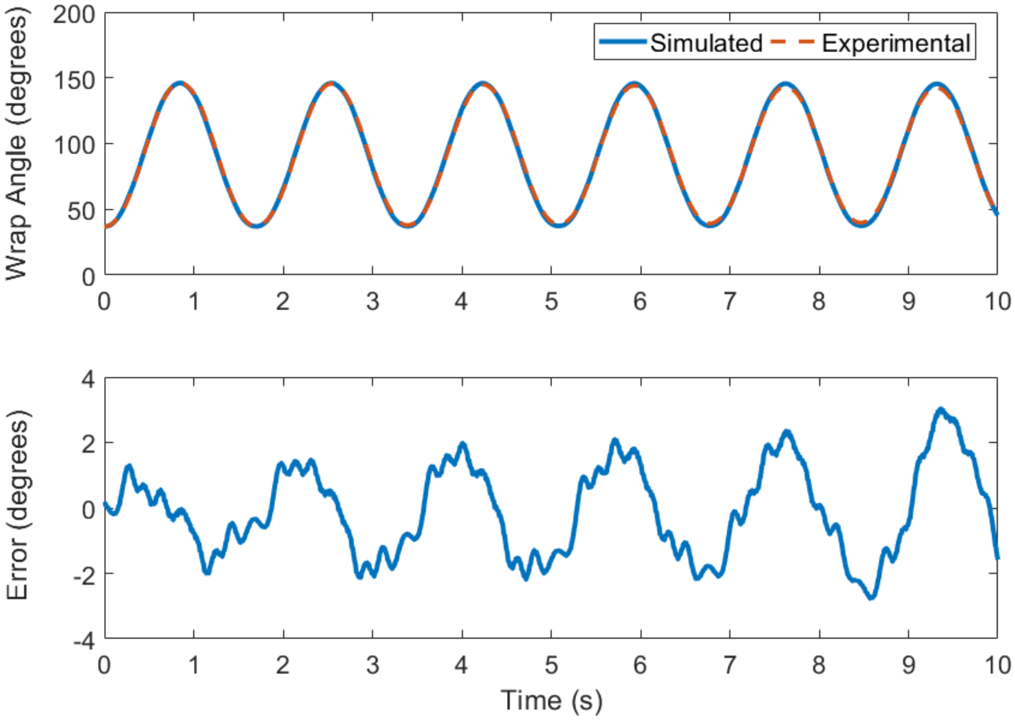

**Figure 21:** Comparison between experimental and simulated wrap angle for stationary pulley experiment.

Figure 21 compares the experimental and simulation cable tensions for configuration 1. The standard deviation of the error was determined to be 6.22 N with a maximum error of 21.2 N. The measured tension varied between 49.2 and 162 N. Similarly, the standard deviation of the tension error was 14.64 N with a maximum error of 40.9 N for Configuration 2 where the measured tension varied between 119 N and 285 N. The standard deviation of the tension error was 14.6 N with a maximum error of 56.7 N for Configuration 3 where the measured tension varied between 204 and 367 N.

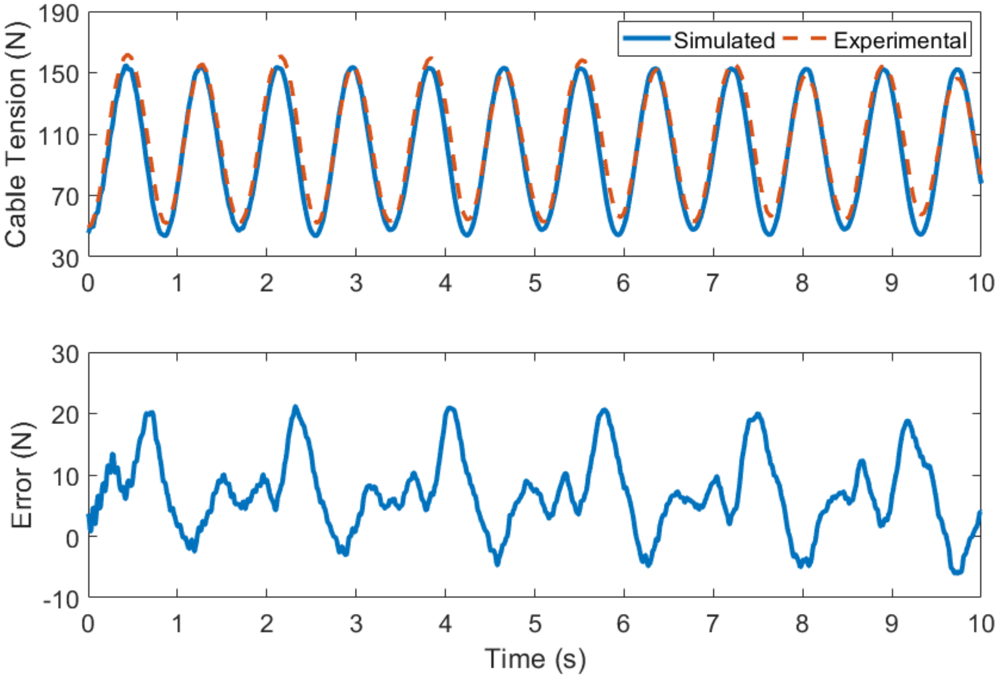

**Figure 22:** Comparison between experimental and simulated cable tension for stationary pulley experiment.

These results indicate a good agreement of the model implementation to the physical results over the given time period. A potential source of error in these results is the assumed elastic modulus of the cable. Additionally, the cable damping coefficient can be tuned to match the decay rate of the experimental motion and reduce the error in the simulation.

A contribution the this thesis is the validation of the model for a system undergoing large variations in the wrap angle of the cable around the pulley. It was demonstrated that the model can accurately reproduce the behavior of the system while the wrap angle varied by as much as 110 degrees from peak to peak. The next section examines the validation of the cable tension for a system with sheave motion.

## 4.2 Cable-Pulley System with Pulley Motion

A second experiment was performed with a moving pulley in order to further validate the simulated tension. Figure 23 illustrates the system consisting of a pulley attached to a cantilevered arm and supporting a fibre rope with a load attached to one end, while the other end of the cable is fixed to the cantilevered arm. An electric linear actuator was used to rotate the arm about a hinge. The cable tension was measured with a load cell and the actuator extension was recorded using an encoder to determine the positions of the pulley and the attachment point of the cable to the arm.

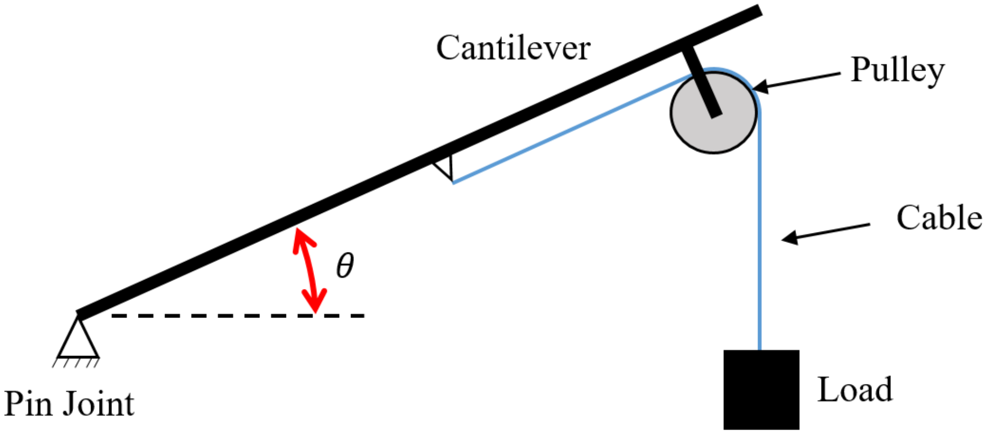

**Figure 23:** Illustration of cable-pulley system with moving pulley. A linear actuator is used to rotate the cantilever about the pin joint.

Table 2 lists the experimental parameters. The position of the centroid of the pulley relative to the pin joint when the arm is horizontal was [0.887, -0.0075] m. The position of the attachment point of the cable to the cantilever was [0.188, -0.0325] m. The length of the cable measured from the attachment point was 132 cm.

A PD controller was used to extend and retract the actuator based on a sinusoidal set-point with a frequency of 1 Hz. Figure 24 shows the angle of rotation $\theta$ of the cantilever as shown on Figure 23 for 10 seconds of motion. The experimental tension

**Table 2:** Model parameters for cable-pulley experiment with moving pulley.

| | |
|---|---|
| Pulley radius, $R$ | 3.18 cm |
| Rope diameter, $d$ | 0.884 cm |
| Rope linear density | 0.59 g/cm |
| Rope modulus of elasticity, $E$ | 2.0 GPa |
| Rope second moment of area, $I$ | $4.0 \times 10^{-14}$ m$^4$ |
| External load mass, $m_L$ | 4.749 kg |
| External load length, $L_{P,I}$ | 8.55 cm |
| External load length, $L_{P,G}$ | 6.85 cm |

data was filtered using an FIR filter with a pass-band edge frequency of 3 Hz.

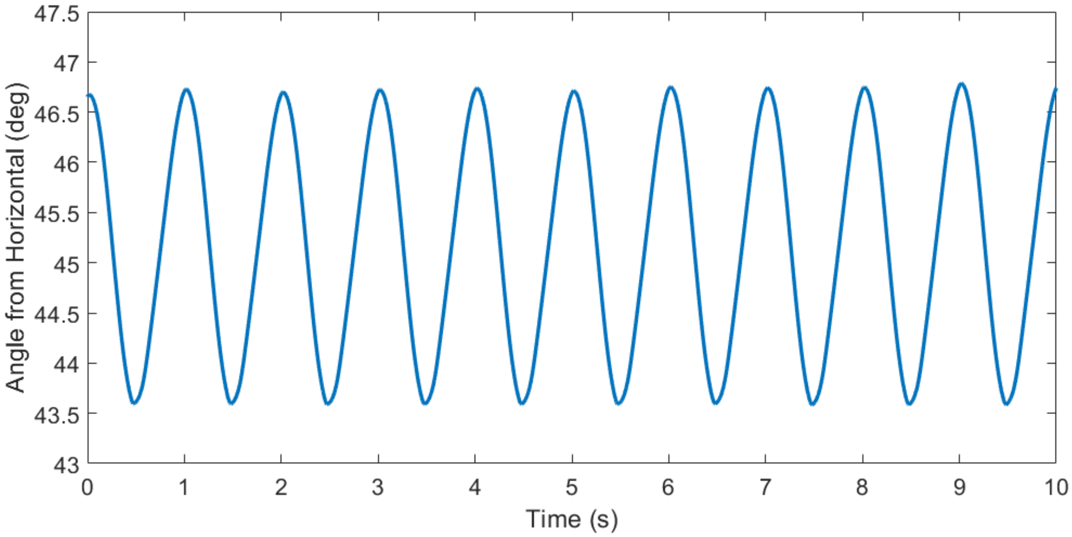

**Figure 24:** Rotation of cantilevered arm as function of time.

As the rope used was identical to the experiment in Section 4.1, the same cable properties were used. Following the convergence study in Section 4.1, the ratio between the element length and the pulley radius was 0.95. To determine an appropriate number of elements to be used in the simulation for this experiment, the ratio was kept the same and forty-four elements were used.

The simulation was performed for 10 seconds of motion. Figure 25 compares the simulated and measured tension as a function of time. The standard deviation of the error between the simulated and experimental tension was 1.79 N with a maximum error of 6.40 N as the tension varied from 36.9 N to 51.5 N over the given time frame. While the peak tension is significantly under-predicted by the simulation, the minimum tension value predicted by the simulation shows good agreement with the experimental measurements.

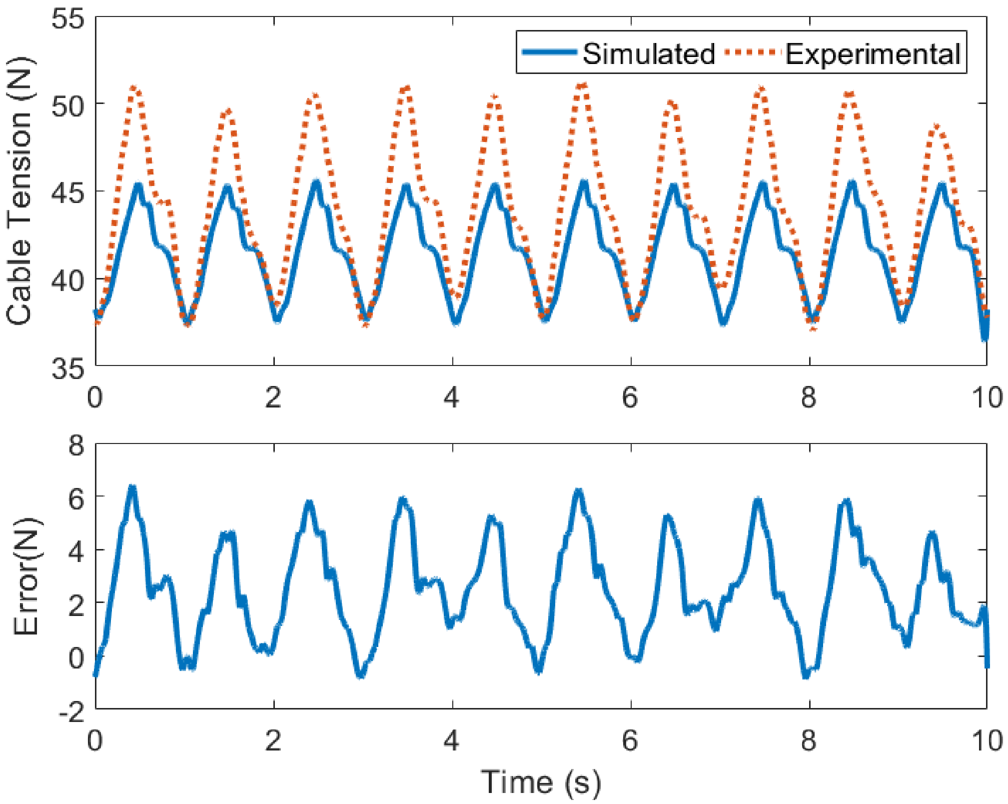

**Figure 25:** Comparison of measured and simulated cable tension for moving pulley experiment.

These results indicate that the simulation can reproduce the cable tension for systems with a moving pulley with reasonable accuracy. The simulation demonstrated good accuracy when the cable tension was at a minimum. Since detachment of a cable from a sheave is most likely to occur during low tension conditions, the ability of the model to accurately predict the minimum tension is advantageous when examining cable detachment behavior. Possible future work could focus on increasing the accuracy of the simulation for predicting peak cable tensions during periodic motions and snap loading. In the next section, the model is validated using previously recorded measurements of towed body motion in a flume tank.

## 4.3 Flume Tank Experiment

Calnan [2] performed an experiment to quantify the efficacy of the AHC algorithms. The experiments were performed in a recirculating flume tank. The system consisted of a thin nylon monofilament cable connected to a small winch. A spherical towbody was attached to the end of the cable. A 3 degree-of-freedom mechanism was used to translate the winch to simulate ship motion. Video recordings of the towbody motion were taken using two cameras, one perpendicular to the flow and one facing in the direction of the flow and submerged in the flume tank. The two videos were used to produce a three dimensional trace of the towbody motion. In the current study, Calnan's recorded towbody motion was used to validate the ANCF cable model.

Figure 26 shows a schematic of the system consisting of a winch, cable and a spherical towbody. The system did not include a sheave. The waterline is located 46 cm below the top of the sheave in its nominal position. Table 3 lists the parameters of the flume scale experiment. Note that the cable length is measured from the top of the sheave. For the current study, the origin of the inertial frame is located at the top of the winch when in its nominal position.

Calnan utilized ship motion data digitized from an Australian Defence Science and Technology Organisation (DSTO) report [65]. The data was used to determine the 3 degree-of-freedom translational motion of a winch located at the ship's stern and was then scaled to fit within the flume tank environment. Figure 27 shows the displacement of the winch along each axis as a function of time. In the current study, the MATLAB function *spapi* was used to produce a third-order piece-wise polynomial fit of the winch motion data. As the ODE solver *ode15s* uses a variable time step, the

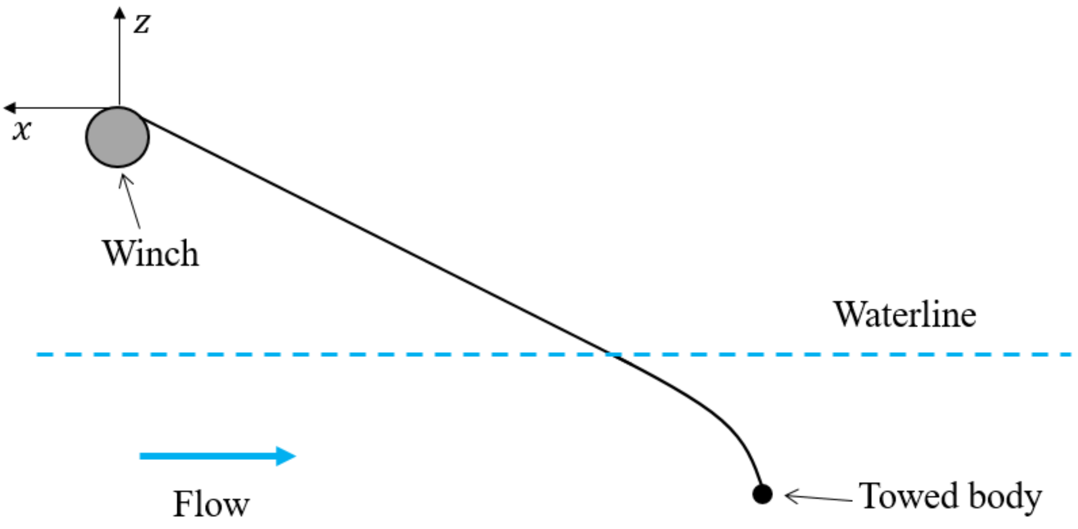

**Figure 26:** Flume tank system. The origin of the inertial frame is located at the top of winch in its nominal position. The $y$-axis is directed out of the page.

piece-wise polynomial allows the position and velocity of the winch to be evaluated at any time $t$ during the numerical integration.

Additionally, Calnan measured the flow velocity at several depths below the surface of the water in the flume tank. A empirical linear relationship between the mean flow velocity $\overline{\mathbf{V}}_f$ and depth was found to be

$$\overline{\mathbf{V}}_f = -0.5873(z - z_{WL}) - 0.3302 \tag{140}$$

where $z$ is the vertical position in the inertial frame and $Z_{WL}$ is the position of the waterline. The standard deviations of the flow along the $x$, $y$ and $z$ axes were found to be 0.0300 m/s, 0.0262 m/s, and 0.0152 m/s, respectively. Calnan applied a Chebyshev II low-pass filter with 80dB attenuation to a white noise signal in order to approximate the frequency spectrum of the measured velocity and scaled the filtered signal to match the measured variances in each axis. Following Calnan's work, a Chebyshev II filter was used in the current study to generate a time series of the flow velocity at a frequency of 100 Hz prior to the simulation. As with the sheave motion,

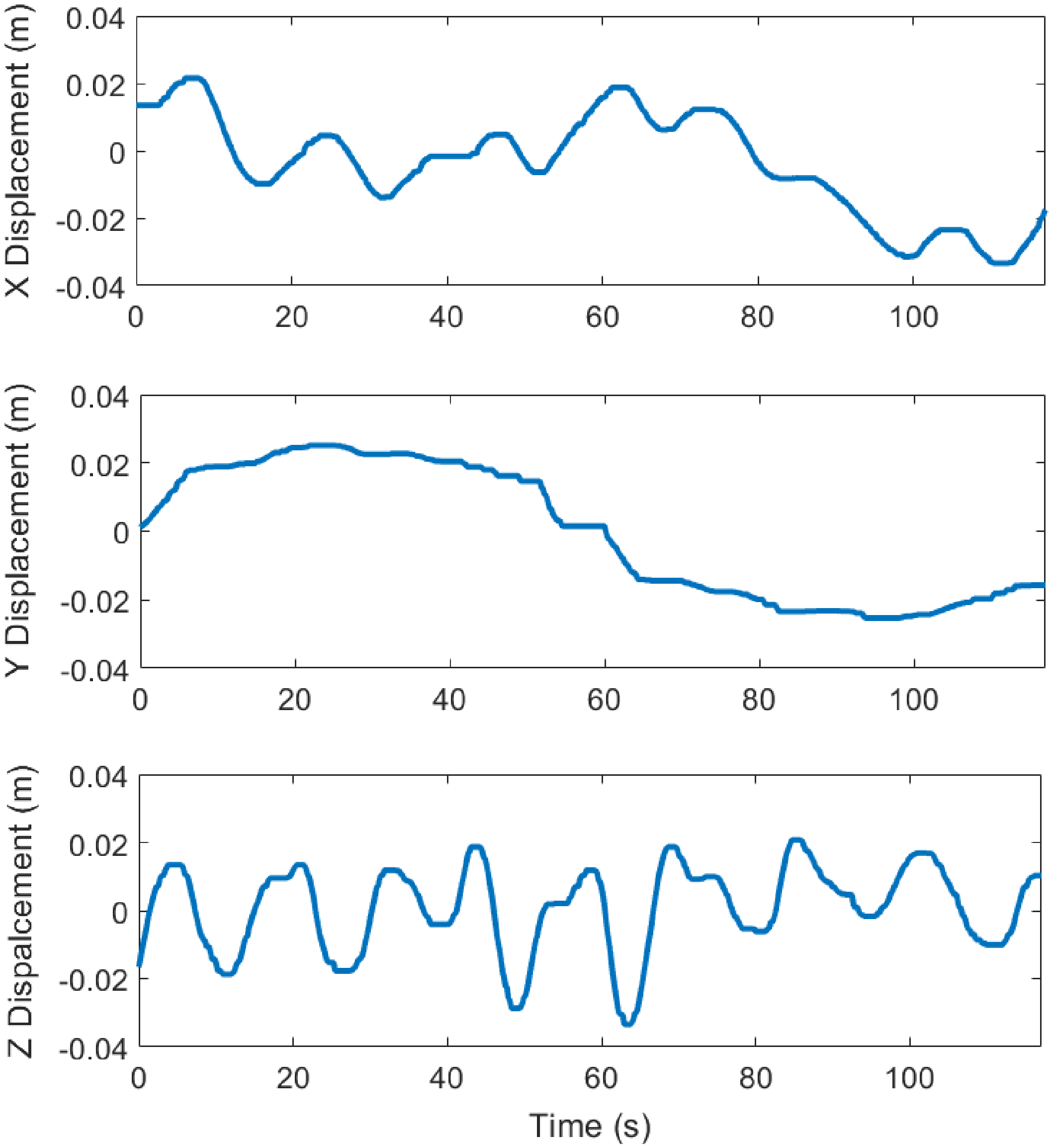

**Figure 27:** Winch displacement as a function of time from Calnan's flume tank experiment [2].

a piece-wise polynomial was fit to the data using the *spapi* function such that the flow velocity can be evaluated at any frequency required by the ODE solver.

In his flume-scale study, Calnan used a state-space model of a DC motor with position control to convert the PD controller output to a rotational acceleration. The

| Parameter | Value |
|---|---|
| Cable diameter | 0.45 mm |
| Linear cable density | 0.2 g/m |
| Nominal cable length | 1.01 m |
| Sphere diameter | 10 mm |
| Sphere mass | 1.33 g |
| Water density | 1026 kg/m$^3$ |
| Water viscosity | $1.2\times10^{-3}$ Pa·s |
| Winch radius | 17.35 mm |

**Table 3:** Flume scale system parameters.

PD gains were tuned based to obtain a 90% rise time of 0.2 s in response to a step input of 0.5764 rad. The length of cable reeled in or out by the winch tracked the AHC set point to within 1 mm for the majority of the motion. In the current study, the system was simplified such that the angular acceleration is given directly by the PD output of Equation 136. The proportional and derivative gains $k_1$ and $k_2$ were tuned manually to obtain tracking errors within approximately 1mm and a 90% rise time of 0.2s, following Calnan's experimental results. The proportional and derivative gains were selected to be 200 and 20, respectively. The standard deviation of the tracking error in the simulation was 0.42 mm. Figure 28 shows the error between the amount of cable reeled out and the simplified sheave set point.

The added mass coefficients of the cable and the towed sphere $C_m$ and $C_{m,b}$ were selected based on theoretical values of 1 and 0.5 [66], respectively, which are consistent with the values used by Calnan [2]. The following additional parameters were identified using the ANCF cable model: cable bending stiffness $EI$, damping coefficient $c$ and drag amplification factor $G$. The estimation of these parameters is described in the following section. Additionally, a convergence study was performed to ensure the accuracy of the simulations.

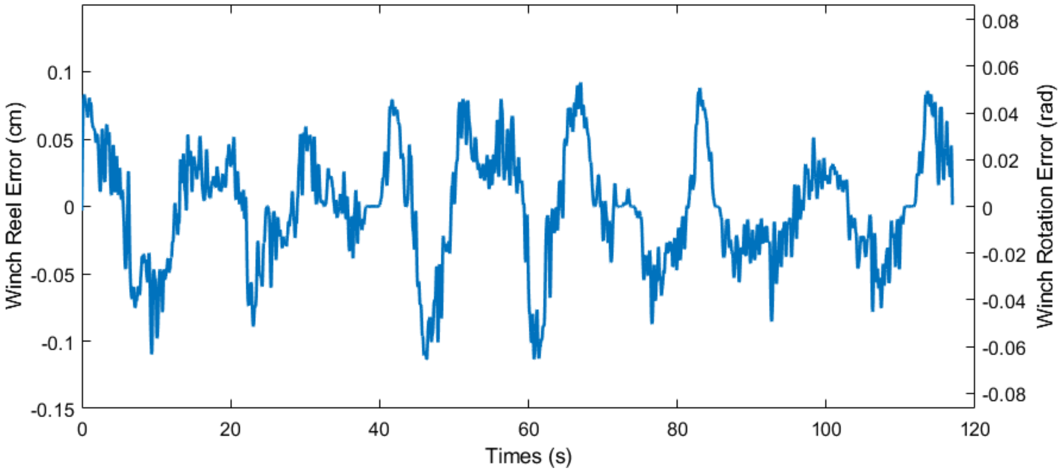

**Figure 28:** Error between winch reel distance and simplified sheave setpoint.

### 4.3.1 Parameter Estimation

The cable used in the flume tank tests was nylon fishing line [2]. Calnan assumed an elastic modulus $E$ of 3 GPa. Reported values of the elastic modulus for Nylon 6-6, a material commonly used in fishing lines, range from 0.7 to 5 GPa [67]. As the elastic modulus $E$ and the bending stiffness $EI$ are proportional, error in the value of $E$ can result in an unrealistic curvature at the winch transition. It is therefore necessary to estimate the bending stiffness empirically.

A test was conducted to approximate the elastic modulus by clamping one end of a small length of cable horizontally with a mass attached at the free end. A photograph, Figure 29 was taken of the cable profile in front of a grid of known spacing. Twenty-five points were selected graphically on the photograph and converted from pixel coordinates to spatial coordinates based on the grid spacing. The points could then be compared to the simulated cable profile. Figure 29 shows the photograph of the clamped cable with the selected points overlaid as red circles. The shadow visible in the figure was neglect in post-processing.

For each point on the photograph, the position in each axis is projected onto the cable profile. Figure 30 shows the cable profile as a blue line and the data point as

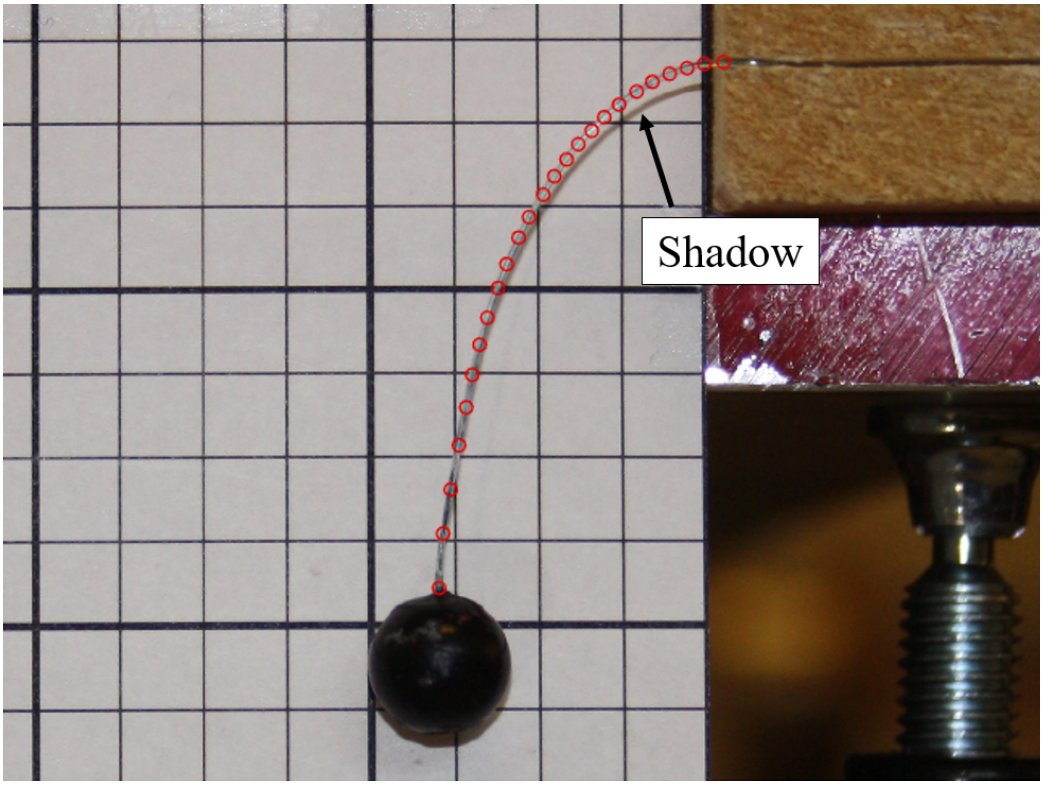

**Figure 29:** Photograph of clamped cable with selected points as red circles.

an open circle with a position $\mathbf{p}_k$ in spatial coordinates, where $k$ is the index of the point. The horizontal and vertical distances $\bar{x}$ and $\bar{z}$ between the data point and the cable profile were then estimated for each point.

An optimization was performed to determine the value of $EI$ that minimizes the function

$$\epsilon(EI) = \sum_{k=1}^{25} (\bar{x}_k^2 + \bar{z}_k^2). \tag{141}$$

The cable had a length of 46.4 mm measured from the fixed point to the center of the sphere. The minimization was performed using a golden section search over a range of $2\times10^{-6}$ to $6\times10^{-6}$ Nm$^2$. Conservatively, twenty cable elements were used to determine the profile of the cable at equilibrium. The optimal value of $EI$ was found to be $2.82 \times 10^{-6}$ Nm$^2$ with a total error $\epsilon$ of $2.54\times10^{-7}$ m$^2$. The Young's modulus

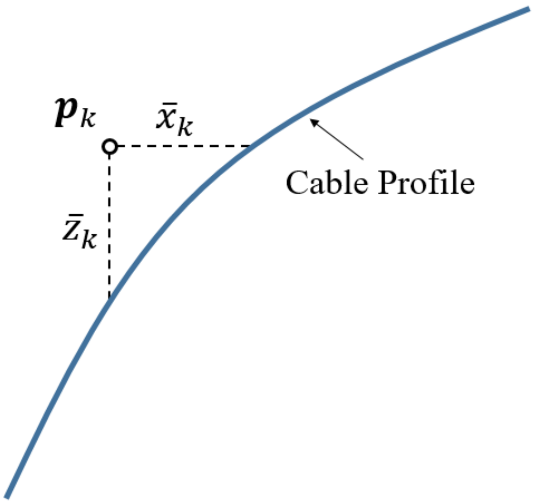

**Figure 30:** Projection of data point from photograph onto cable profile

was then be estimated to be 1.40 $GPa$ by dividing the bending stiffness $EI$ by the moment of inertia $I$ for a solid cylinder of $2.01\times10^{-15}$ m$^4$. Figure 31 shows the final simulated cable profile as an orange line and the points selected from the photograph as blue circles.

Calnan identified an empirical damping ratio of the cable of 0.061 [2]. In order to determine an appropriate damping coefficient $c$ from Equation 55 for the current study, a simplified model was introduced to approximate the relationship between the intrinsic damping and the damping coefficient. The simplified system consists of a vertical cable clamped at the top. The bottom of the cable is free and attached to a lumped mass. The cable properties and mass properties were kept the same as the parameters of the flume tank experiment listed in Table 3. The cable was deflected a small amount and then released. The damping ratio $\zeta$ is determined from the oscillating horizontal displacement using the equation

$$\zeta = \frac{1}{2\pi} ln \left( \frac{x_1}{x_2} \right) \tag{142}$$

where $x_1$ and $x_2$ are the displacements of successive peaks. The observed damping

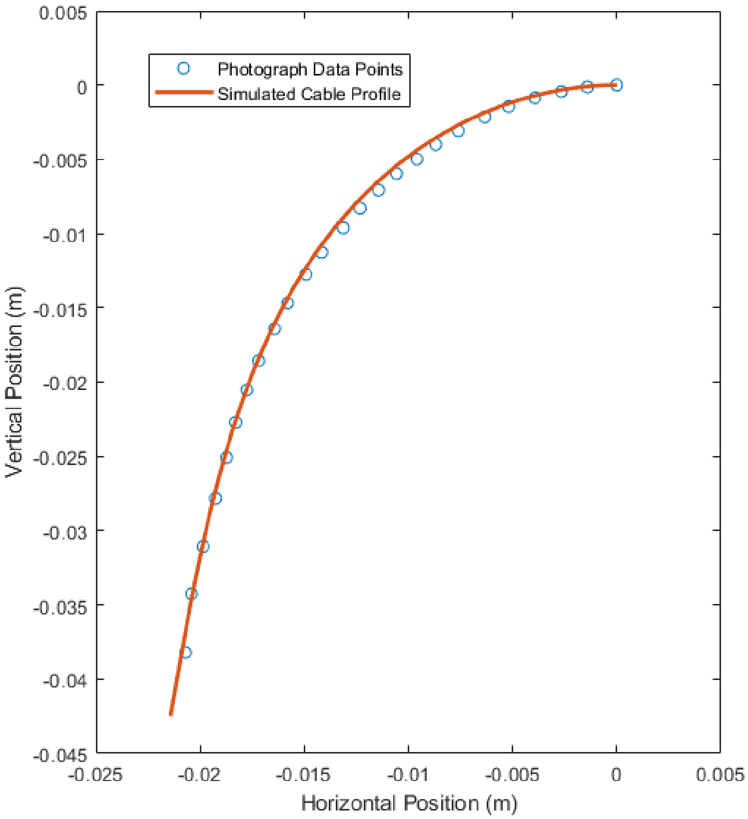

**Figure 31:** Simulated profile of clamped cable and points selected from photograph.

ratio was determined for a range of damping coefficients from $1 \times 10^{-4}$ to $10 \times 10^{-4}$ Ns. The damping ratio $\zeta$ and damping coefficient $c$ were found to have a linear relationship over the range. The equation of the line of best fit was determined to be $\zeta = 112.72c$. Based on the damping ratio of 0.061 determined experimentally by Calnan, the damping coefficient was selected to be $5.4{\times}10^{-4}$ Ns.

The drag amplification due to vortex shedding is quantified in the model by the amplification factor $G$ from Equation 64. This parameter was tuned based on the mean tow body position recorded in the flume tank experiments with no applied motion. The centroid of the experimental towbody motion was $[-0.708, -0.008, -0.685]$ m. The steady state position of the was obtained by running the simulation with no noise or winch motion. The system was considered to have reached equilibrium when the maximum velocity of any point on the cable is less than $1 \times 10^{-4}$ m/s. The error was taken as the Euclidean distance between the steady-state towbody position and the centroid of the experimental data. The amplification factor was estimated using a golden-section search method over a range from 1 to 2. The optimized value of the amplification factor $G$ was 1.737 with an error of 5.0 mm.

### 4.3.2 Cable Mesh

Since the elements in contact with the winch will have a much larger curvature than the rest of the cable, it is desirable to use a variable mesh such that smaller elements are used for the contact region and larger elements are used elsewhere. A variable mesh will minimize the number of elements required to obtain convergence and thereby reduce the computational requirements of the simulation.

The cable is thus divided into two segments as shown in Figure 32. Segment 1 comprises all points on the cable that may come into contact with with winch surface throughout the motion and segment 2 is remaining length of cable. A nominal winch rotation $\phi_{nom}$ measured from the vertical axis is defined, such that when the winch is in the nominal position the length of the cable measured from the top of the sheave be equal to the nominal length $L_{nom}$ of 1.01 m. The total cable length includes the nominal length $L_{nom}$ and the length of cable in contact with the winch:

$$L_{total} = L_{nom} + \phi_{nom} r_w \tag{143}$$

where $r_w$ is the winch radius. The length of the segment 1 is defined based on the maximum amount of cable to be reeled in. The nominal rotation angle was defined as $\pi/2$ rad and the length of the first segment was defined as 3/4 of the winch circumference or 81.8 mm. These values were selected based on the expected winch rotations for the simplified sheave case, such the the pin joint will not pass the top of the winch when fully reeled out and the second cable segment will not contact the winch when fully reeled in.

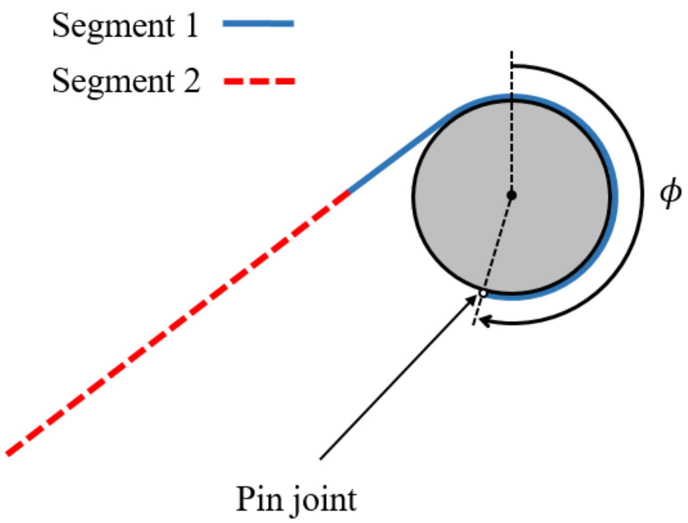

**Figure 32:** Cable segments and winch rotation.

Next, a convergence study was performed by successively increasing the number of elements in the two sections. The mesh for segment 1 was refined first, keeping the number of elements in segment 2 constant at 4 elements. Simulations were performed using the simplified sheave algorithm and a length of 20 s with the number of elements in the first segment ranging from 4 to 16. Figure 33 plots the sheave angle $\theta$ over time for each mesh. The change in the sheave angle was found to be insignificant between the 12 element and 16 element simulations with a maximum difference of $2.7\times10^{-4}$ rad. Thus 12 elements was selected for the first segment.

The mesh for the second segment was then refined, keeping the number of elements in the first segment constant at 12 elements. Again, 20s simulations were performed with the number of elements ranging from 4 to 16. Figure 34 plots the vertical position of the towed sphere. The change in the cable motion was again found to be insignificant between the 12 element and 16 element simulations with a maximum difference of 0.05 mm, thus 12 elements was selected for the second segment.

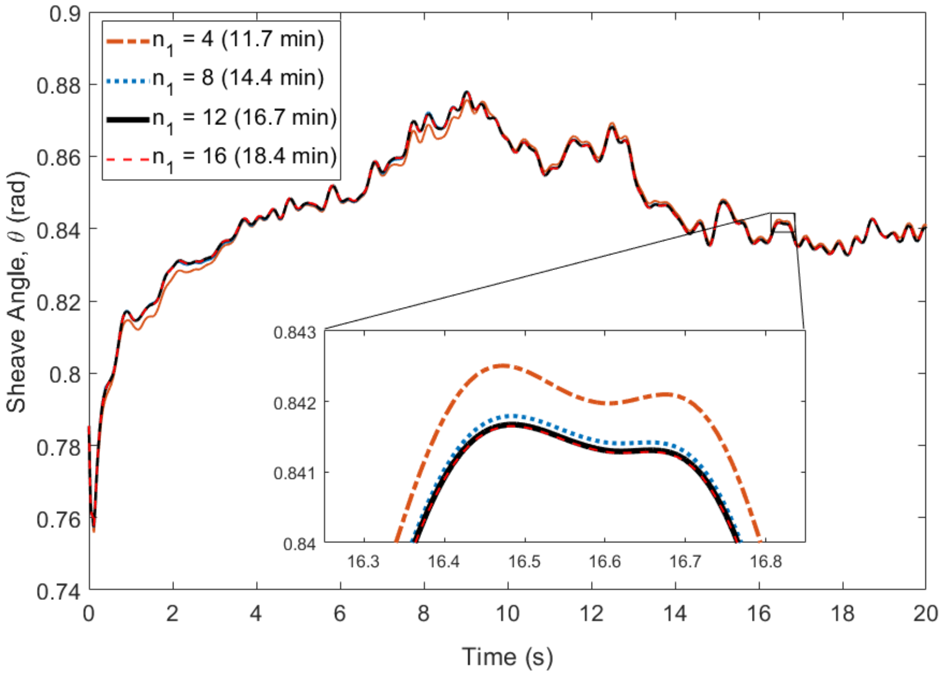

**Figure 33:** Sheave angle over time with the number of elements $n_1$ in the first segment varied between 4 and 12. Computation times are shown in the legend.

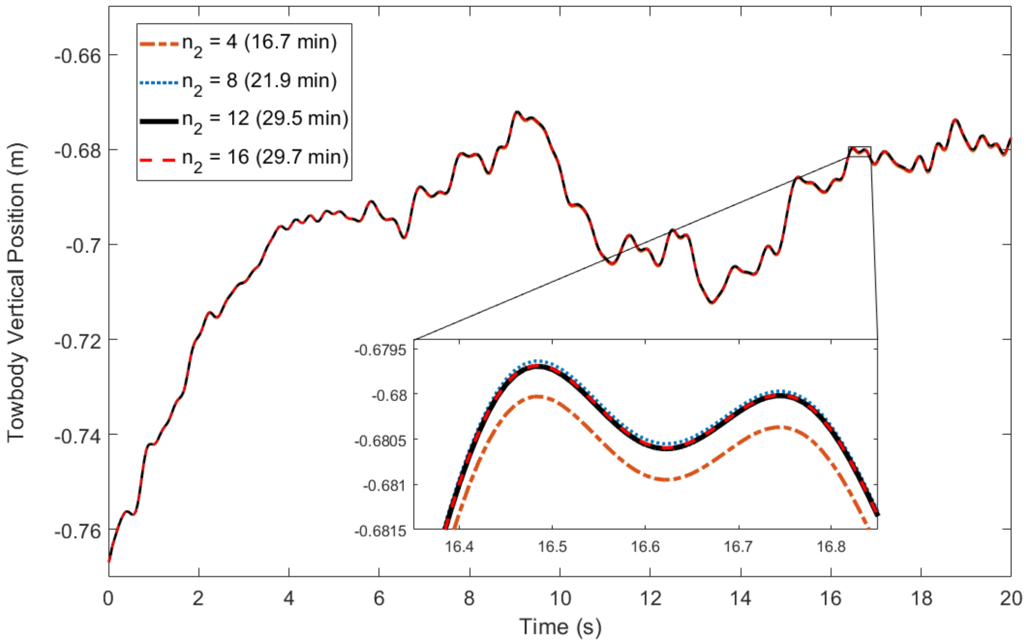

**Figure 34:** Vertical position of towed sphere over time with the number of elements $n_2$ in the second segment varied between 4 and 12. Computation times are shown in the legend.

### 4.3.3 Test Cases and Results

For each simulation, an ellipsoid was fit to the trace of the towbody motion such that it contained 95% of the data points. Calnan's ellipsoid fitting algorithm was used to fit the ellipsoid to the data. Figure 35 illustrates the principal axes of the ellipsoid $X_E, Y_E$ and $Z_E$. The ellipsoid fitting algorithm consists of centering the ellipsoid coordinate frame at the centroid of the simulated data. A best fit line and best fit plane are then fit to the data. The ellipsoid frame is rotated such that the $X_E$ axis is aligned with the best fit line and the $X_E$ and $Y_E$ axes are coplanar with the best fit plane. The radii of the ellipsoid are scaled proportional to the variance along each axis until 95% of the points are contained within the volume.

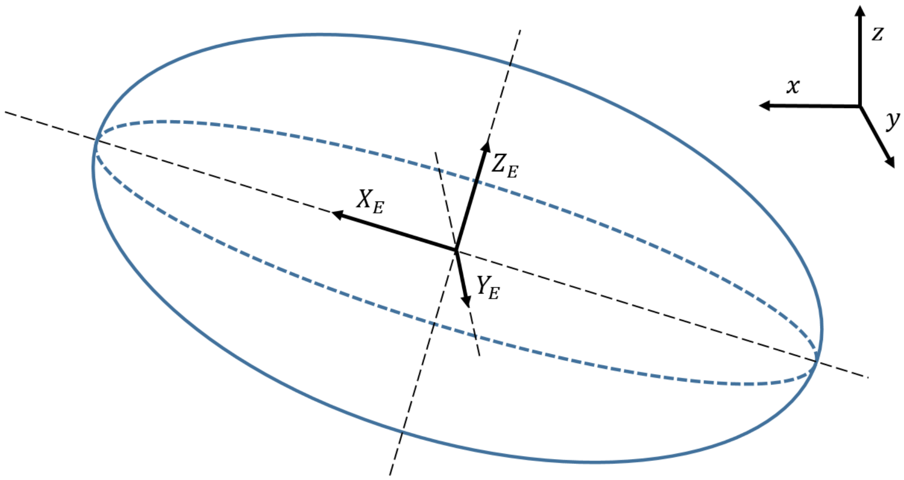

**Figure 35:** Ellipsoid principal axes and inertial coordinate frame.

The simulation was first performed without motion of the winch and the motion of the towbody was determined. Figure 36 shows the simulated towbody motion as a blue line viewed from the side of the flume tank. The experimental body motion is plotted as an orange line and Calnan's simulated towbody motion as a yellow line. Table 4 gives the results of the ellipsoid fitting and the standard deviation of the motion along each ellipsoid axis. The percent errors compared to the experimental results are given in parentheses. While Calnan's simulation underpredicted the ellipsoid volume by 58 percent, the current ANCF simulation overpredicted the volume by a similar amount. The ANCF simulation better predicted the centroid of the towbody motion. The distance between the centroid of the experimental motion and the simulation motion was 0.48 cm for the ANCF simulation and 1.59 cm for Calnan's simulation.

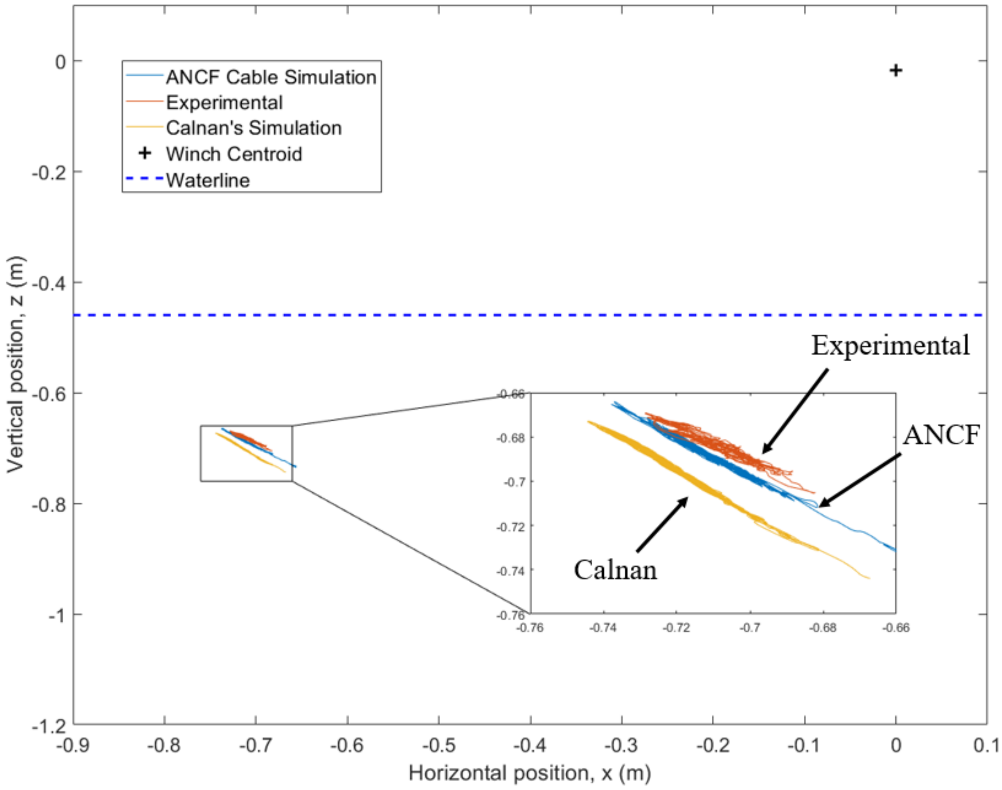

**Figure 36:** Motion of towed sphere with no winch motion.

| | Experimental | Calnan's Simulation | ANCF Simulation |
|---|---|---|---|
| Ellipsoid Volume ($cm^3$) | 4.82 | 2.04 (-58%) | 7.76 (61%) |
| $X_E$ Std. Dev. (cm) | 1.19 | 1.43 (20%) | 1.56 (31%) |
| $Y_E$ Std. Dev. (cm) | 0.78 | 0.43 (-45%) | 1.23 (58%) |
| $Z_E$ Std. Dev. (cm) | 0.13 | 0.05 (-62%) | 0.07 (-49%) |

**Table 4:** Results for no winch motion test case. Error relative to experimental values in parentheses.

Next, the simulation was first performed with winch motion but without heave compensation. Figure 37 shows the experimental and simulation motion traces. Table 5 compares the ellipsoid fitting results for the simulated and experimental motion. The ANCF simulation agreed closely with experimental ellipsoid volume with an error of only 1.7 percent, a significant improvement over Calnan's simulation which had an error of -24 percent. Again, an improvement was seen in the location of centroid of the towbody motion. The distance between the centroid of the experimental motion and the simulation motion was 2.15 cm for the ANCF simulation and 3.25 cm for Calnan's simulation.

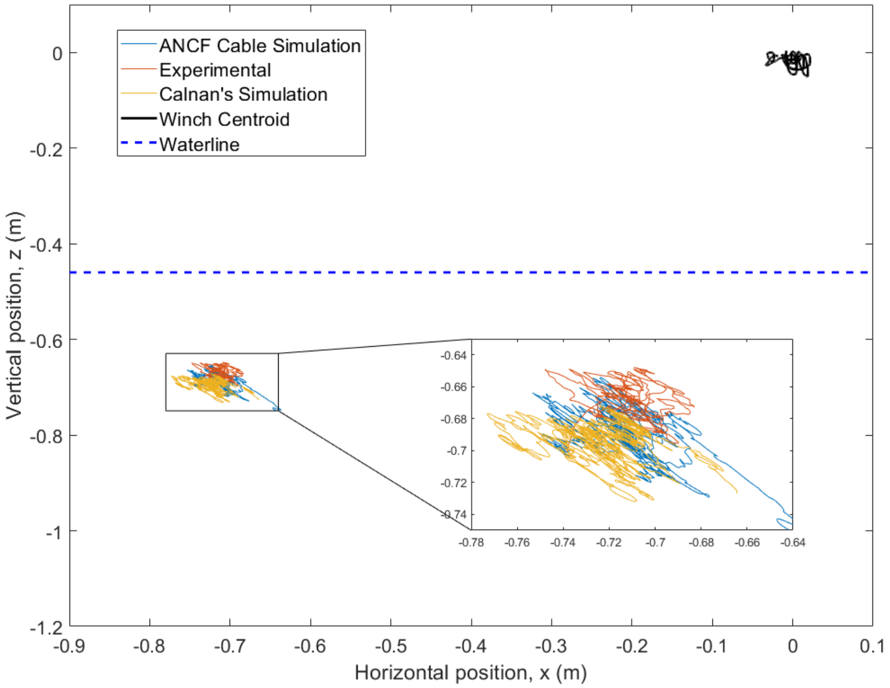

**Figure 37:** Motion of towed sphere for uncompensated case with winch motion.

Finally, the motion was simulated utilizing the rigorous sheave and simplified sheave heave compensation algorithms described in Section 2.1. Figure 38 shows the towed body motion for the rigorous sheave test case. Tables 6 and 7 give the ellipsoid

|  | Experimental | Calnan's Simulation | ANCF Simulation |
|---|---|---|---|
| Ellipsoid Volume ($cm^3$) | 182.84 | 138.51 (-24%) | 185.96 (1.7%) |
| $X_E$ Std. Dev. (cm) | 2.73 | 2.20 (-20%) | 2.14 (-21%) |
| $Y_E$ Std. Dev. (cm) | 1.36 | 1.41 (3.8%) | 1.55 (14%) |
| $Z_E$ Std. Dev. (cm) | 0.88 | 1.04 (19%) | 0.97 (10%) |

**Table 5:** Results for uncompensated case with winch motion. Error relative to experimental values in parentheses.

fitting results for the simplified and rigorous sheave test cases, respectively. In both cases the ellipsoid volume predicted by the ANCF simulation was smaller than the experimental volume, but a significant improvement over Calnan's simulation was observed. For the simplified sheave case, the ellipsoid volume was 27% smaller for the ANCF simulation and 51 percent smaller for Calnan's simulation. For the rigorous sheave case the volume was 22% smaller for the ANCF simulation and 56 percent smaller for Calnan's simulation. The standard deviation of the motion along the $Z_E$ axis of the ellipsoid was significantly smaller in the simulation than in the experimental results for both simulations.

The ANCF simulation and Calnan's simulations showed similar errors in the centroid of the motion in both cases. For the simplified sheave case, the distance between the centroid of the experimental motion and the simulation motion was 1.88 cm for the ANCF simulation and 2.14 cm for Calnan's simulation. For the rigorous sheave case, the distance between the centroid of the experimental motion and the simulation motion was 2.62 cm for the ANCF simulation and 2.32 cm for Calnan's simulation.

In general, the ANCF simulation performed significantly better at predicting the ellipsoid volume than Calnan's simulation. Also, the ANCF simulation demonstrated less error in the location of the centroid of the motion for most test cases. The ANCF performed best for the uncompensated case, with an error in the ellipsoid volume of only 1.7 percent. The highest error was observed in the case with no motion, with an error of 61 percent. One possible source of error in the simulations can be attributed

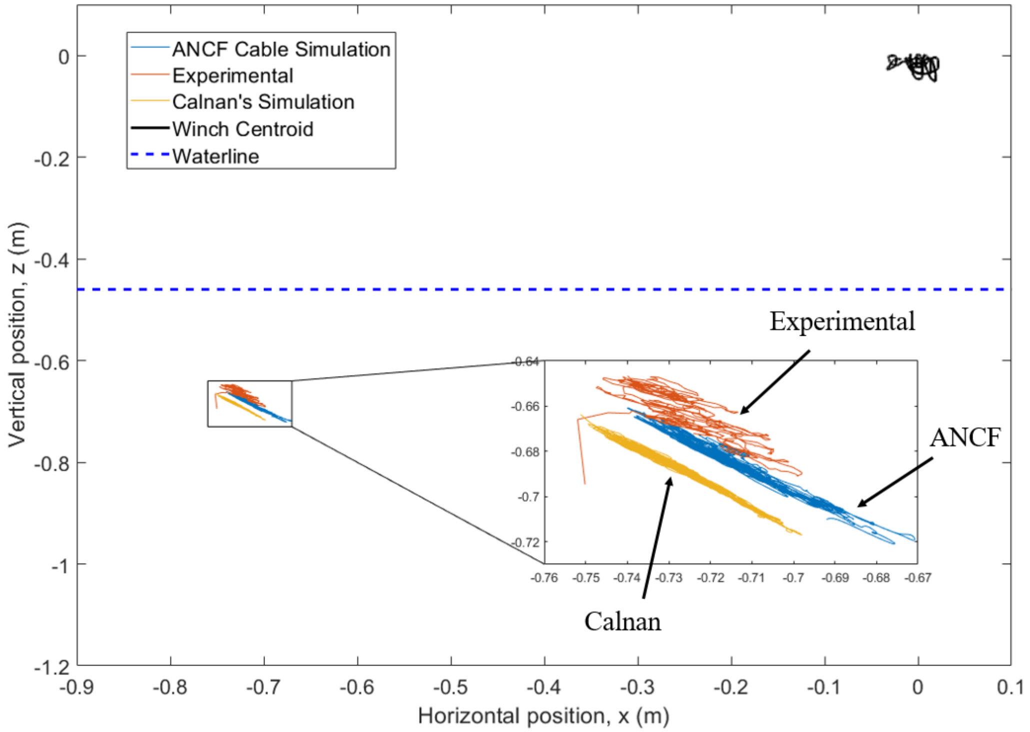

**Figure 38:** Motion of towed sphere for rigorous sheave test case.

| | Experimental | Calnan's Simulation | ANCF Simulation |
|---|---|---|---|
| Ellipsoid Volume ($cm^3$) | 36.55 | 18.00 (-51%) | 26.68 (-27%) |
| $X_E$ Std. Dev. (cm) | 2.58 | 2.07 (-20%) | 2.82 (9%) |
| $Y_E$ Std. Dev. (cm) | 1.29 | 1.18 (-8.5%) | 1.67 (30%) |
| $Z_E$ Std. Dev. (cm) | 0.28 | 0.13 (-52.5%) | 0.12 (-58%) |

**Table 6:** Results for simplified sheave case. Error relative to experimental values in parentheses.

| | Experimental | Calnan's Simulation | ANCF Simulation |
|---|---|---|---|
| Ellipsoid Volume ($cm^3$) | 24.92 | 11.07 (-56%) | 19.55 (-22%) |
| $X_E$ Std. Dev. (cm) | 2.42 | 2.08 (-13.9%) | 2.42 (0.3%) |
| $Y_E$ Std. Dev. (cm) | 1.15 | 1.14 (-1.2%) | 1.48 (28%) |
| $Z_E$ Std. Dev. (cm) | 0.28 | 0.06 (-78%) | 0.10 (-66%) |

**Table 7:** Results for rigorous sheave case. Error relative to experimental values in parentheses.

to the fact that the noise component of the flow velocity is the same at every point in the tank at a given time. Only the mean component of the flow was varied as a function of depth. In reality, the turbulence in the flow velocity is not uniform throughout the tank. This source of error is likely to be most significant in the case with no winch motion, as the motion of the towbody is governed only by the variation in the flow.

In the next chapter, a case study of a full-scale sheave and winch system is described.

# 5 Full Scale Case Study

To demonstrate the capabilities of the techniques developed in this thesis for a full scale system a case study was performed. The system consists of a towed body connected to the vessel by a wire rope, as described in Chapter 1. Both winch and sheave contact are included in the system, with the winch actuated to provide active heave compensation. The parameters used in the simulation are based on a real towed body system where the depth of the towed body, towing speed and the length of cable are known. Table 8 lists the known system parameters.

| **Parameter** | **Value** |
|---|---|
| Cable Diameter | 10 mm |
| Cable Mass per unit length | 0.389 kg/m |
| Cable length (nominal) | 450 m |
| Towbody net weight | 445 N |
| Towbody mass | 250 kg |
| Towbody depth (nominal) | 108 m |
| Flow velocity | [-2.2, 0, 0] m/s |
| Sheave radius | 0.25 m |
| Sheave groove depth | 10 mm [68] |
| Sheave throat angle | 60° [68] |
| Winch radius | 0.30 m |
| Faired cable section length | 150 m |
| Sheave position relative to ship CG | [-36.8, 0, 3.7] m |
| Winch position relative to ship CG | [-28.8, 0, 3.1] m |

**Table 8:** Full scale system parameters.

The motion of the ship was taken from the Australian DSTO report [65] consisting of linear velocities in the inertial frame and roll, pitch and yaw attitudes over 118 s. The linear rates were integrated using the trapezoidal method to obtain the position of the ship's center of gravity as a function of time. The linear positions and orientations of the ship were fit with third order piece-wise splines using the MATLAB function *spapi*. Figures 39 and 40 show the time series of the ship translation and rotations, respectively. The origin of the inertial coordinate frame is located at the waterline. The center of gravity of the ship was assumed to be located at the midpoint of the ship's longitudinal axis and coincident with the origin in the nominal position.

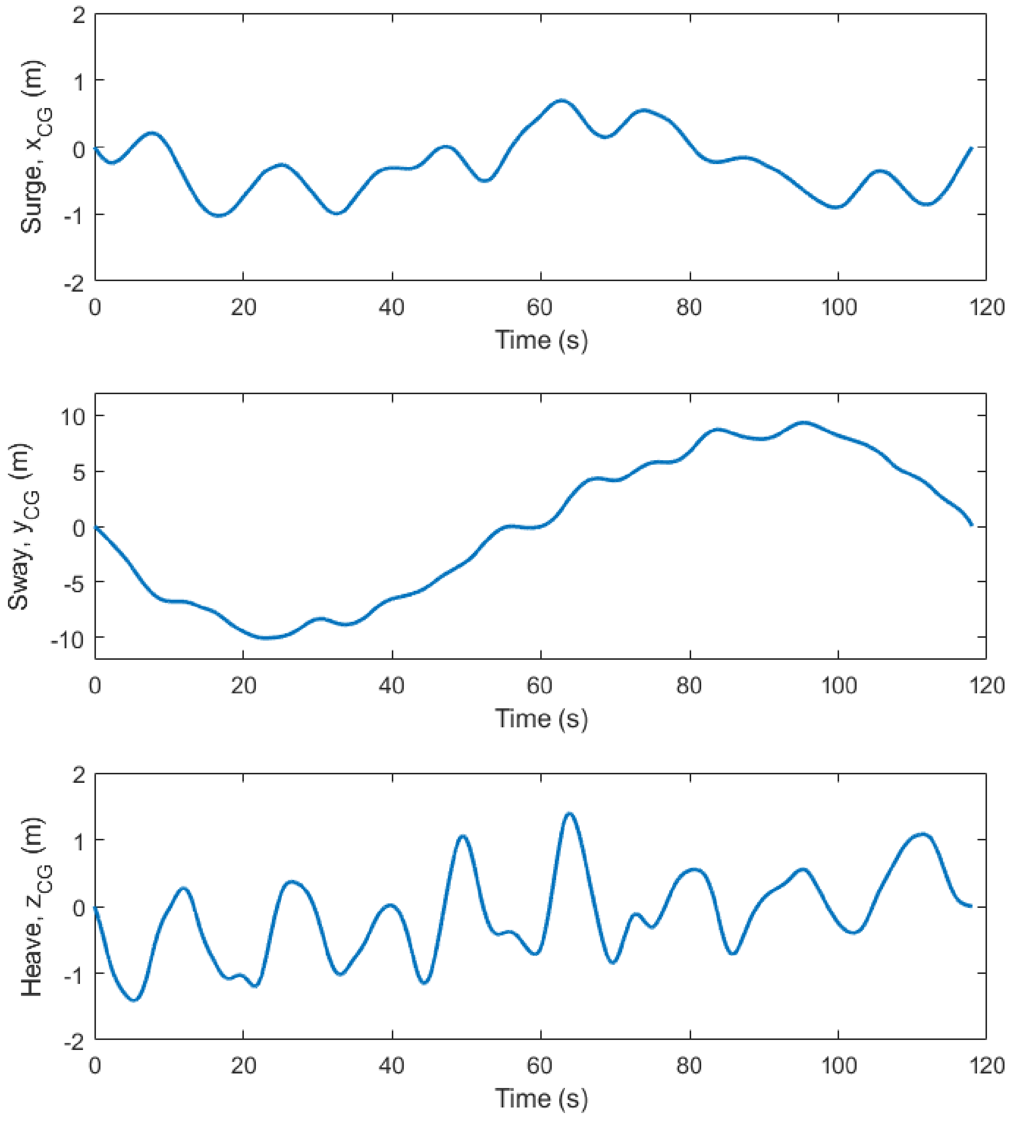

**Figure 39:** Ship translational motion from DSTO report [65]

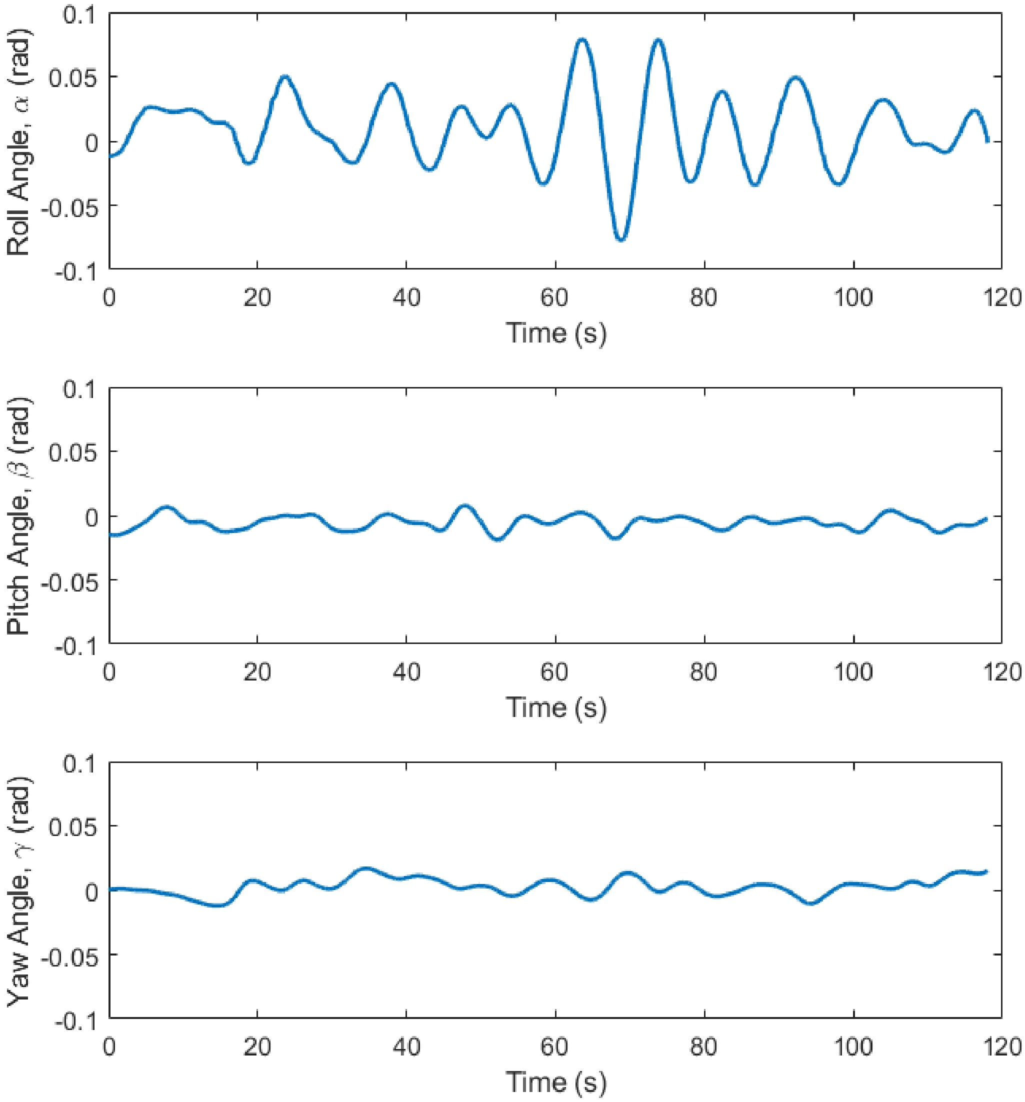

**Figure 40:** Ship rotational motion from DSTO report [65]

## 5.1 Cable Properties

The cable consists of an insulated copper conductor surround by steel wire "armour." The bending stiffness of the copper conductor and insulation were assumed to be negligible compared to the steel strands as the conductor wires are much smaller in diameter than the steel strands. For determining the axial and bending stiffnesses, the cable is treated as a standard 1x37 construction as the wire diameter and number of steel wires are similar to the armoured cable.

The equivalent elastic modulus of a wire rope with a 1x37 construction is approximately 117 GPa and the metallic area for a 10 mm diameter cable is $5.8\times10^{-5}$ m$^2$ [68]. A minimum estimate of the bending stiffness can be calculated by neglecting the friction between individual wires and assuming the total bending stiffness is the sum of the bending stiffnesses of the individual wires [69]. Using the average wire diameter $d_w$, the bending stiffness is

$$EI = E\sum \frac{\pi {d_w}^4}{64}. \tag{144}$$

From the metallic area, the average wire diameter with 37 wires is 1.4 mm. Assuming an elastic modulus of the steel wire of 200 Gpa, the bending stiffness is 1.40 Nm$^2$.

Damping ratios for wire ropes can range from less than 0.1% when under tension [70] to 37% for slack cables [71]. A damping ratio of 1% was assumed for this analysis in which the tension is substantial during towing operations. The damping coefficient $c$ was estimated using the same process described in Section 4.3.1 for the flume scale experiment. The relationship between the damping ratio $\xi$ and the damping coefficient was found to be $\xi = 3.05 \times 10^{-5}c + 5.5 \times 10^{-4}$. The damping coefficient corresponding to a damping ratio of 0.01 is thus $3.1 \times 10^2$ Ns.

## 5.2 Hydrodynamic Loading

The length of the cable is 450m. The final 150m of the cable has “ribbon fairing” attached, which are flexible ribbons that serve to suppress vortex-induced vibration of the cable. Empirical loading functions $f_n$ and $f_t$ specific to cables with ribbon fairing were used for the faired section and are given by

$$f_n = 0.498609 - 0.2499\cos(\eta) + 0.2527\sin(\eta) - 0.2487\cos(2\eta) \tag{145a}$$

$$f_n = -0.2255 + 0.3417\cos(\eta) + 0.255\sin(\eta) - 0.0811\sin(2\eta) \tag{145b}$$

where $\eta$ is the angle of attack between the cable and the flow [72]. For the bare cable section, the loading functions given in Equation 60 were used.

The towed body consists of a cylindrical shell with a hydrofoil attached which produces a downwards force. The cylindrical shell and hydrofoil are treated independently for the purposes of determining the drag force coefficient and interference drag between the bodies is neglected. It is also assumed that the orientation of the body is constant throughout the motion and the axis of the cylindrical shell is align with the flow along the $x$-axis of the inertial coordinate frame.

The cylindrical shell has a diameter of 300 mm and a length of 3 m. For axial flow along the horizontal $x$-axis the drag coefficient for a blunt cylinder is 0.85 [73]. For flow normal to the cylinder, along the $y$ and $z$-axes, the drag coefficient is 1 [74]. For the hydrofoil, a NACA2412 cross-section with an area of 0.5 $m^2$ and angle-of-attack of -6° is assumed. For flow along the vertical z-axis, the hydrofoil is treated as a flat plate with a drag coefficient of 1.17 [73]. For flow along the x-axis, the drag coefficient of the wing is 0.008 [74]. The drag on the hydrofoil is assumed to be negligible for flow along the $y$-axis. The lift acting on the hydrofoil is calculated using a lift coefficient of -0.6 [74], giving a lift force of -722 N at steady state.

The cable is towed at a speed of approximately 4.3 knots (2.2 m/s) with 450 m of cable reeled out and the observed depth is 108 m, representing a severe and undesirable drag condition. An initial simulation was performed where the system was allowed to reach steady state and the depth of the towed body was determined. Using the drag parameters outlined above the depth of the towed body was 213.7 m. A drag amplification factor $G$ was applied to the cable as shown in Equation 64 such that the simulated towbody depth matched the known depth of 108 m. The simulation was performed with the cable pinned at the top of the winch and with twenty cable elements. The amplification factor was tuned manually and a value of 3.54 was determined to achieve a depth of 108 m. This result indicates a significant level of uncertainty in the cable drag. Some of the uncertainty can be attributed to strumming of the bare cable section due to vortex induced vibration (VIV). Cable VIV has been shown to increase the mean cable drag by as much as 130 percent [75].

Figure 41 shows the profile of the cable without amplification of the drag force as a dotted line and the profile with amplification as a solid line. With drag amplification, the nominal angle of the cable measured from vertical as it leaves the sheave is 74.0°. This nominal angle is used to evaluate the simplified sheave setpoint described in Section 2.1.

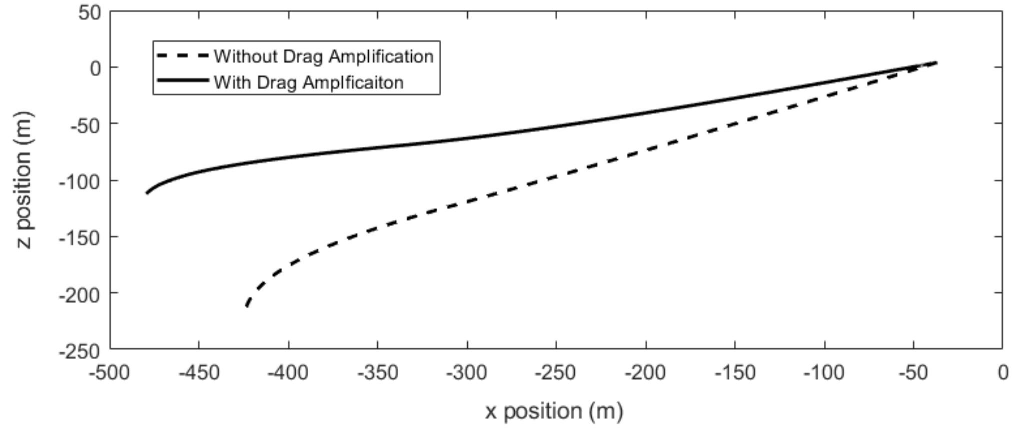

**Figure 41:** Cable profile with and without drag amplification

## 5.3 Initialization

Figure 42 shows the sheave and winch in the body fixed frame with the cable as a solid blue line. Four points are defined as shown on Figure 42: point 0 is the point of tangency for the cable at the nominal sheave angle $\theta_{nom}$, points 1 and 2 are the tangency points of the outer tangent between the sheave and the winch, and point 3 is the point corresponding to the end of the cable in the nominal position with a wrap angle $\phi_{nom}$.

In order to initialize the model, an initial set of generalized coordinates were generated for a straight cable tangent to the sheave surface at point 0. A path was then created originating at point 0 and consisting of 3 stages: moving along the surface of the sheave to point 1, moving linearly to point 2, and moving along the surface of the winch to point 3. A velocity profile starting and ending at rest is created with an integral area equal to the total length of the path. The velocity profile is then integrated and mapped onto the path to give a position vector as a function of time. Using a spherical kinematic constraint, the end of the cable is constrained to move along the path until reaching the nominal position at point 3. The system is then allowed to reach steady state and the final vector of generalized coordinates is then stored, to be used during the final simulation.

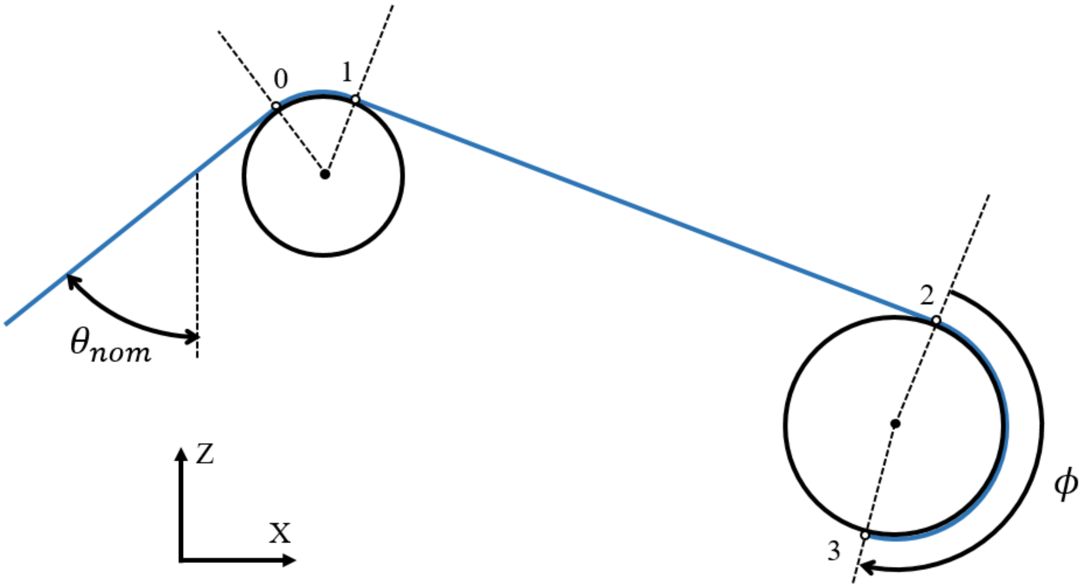

**Figure 42:** Sheave and winch in the ship's body fixed frame

## 5.4 Cable Mesh

The cable was divided into five segments. Figure 43 shows the cable segments and the number of elements used for each segment. Segments 1 and 3 consist of the points on the cable that may come into contact with the winch and sheave, respectively, throughout the motion. Segment 2 connects segments 1 and 3. Segment 4 and 5 comprise the remaining length of cable where segment 5 is the faired length of cable and segment 4 is un-faired.

Based on the winch rotations generated by the simplified sheave algorithm, the lengths of segments 1 and 3 were selected to be 2.5m each and the nominal winch angle $\phi_{nom}$ was selected to be 3.8 radians. The length of segment 2 is the distance between points 1 and 2 minus the length of segment 1, which was calculated to be 5.02 m. The lengths of segments 4 and 5 are 300 m and 150 m, respectively.

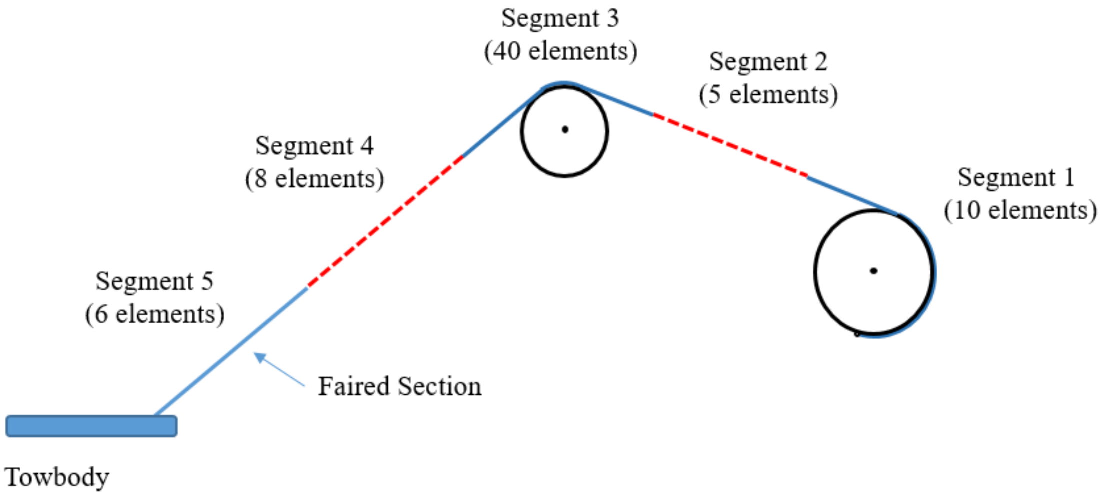

**Figure 43:** Cable segments and number of elements used (not to scale).

Due to the computational expense of initializing and simulating the system, a simplified mesh convergence study was performed. Using only segments 4 and 5, with the end of segment 4 pinned at the top of the winch, the simulation was performed and 20 seconds of the motion was recorded. First, the number of elements in segment 5 was varied from four to eight, with the elements in segment 4 held constant at four. Figure 44 shows the vertical motion of the towbody as a function of time. The computation time for each simulation is shown in the legend. Increasing the number of elements had no significant effect on the towbody motion, but resulted in a 5.3% increase in the computation time. Six elements were used for all subsequent simulations. Next, the elements in segment 4 were varied from four to ten elements. Figure 45 shows the vertical motion of the towbody as a function of time. No significant change in the motion of the towbody was observed beyond eight elements, thus eight elements were used in the subsequent simulations.

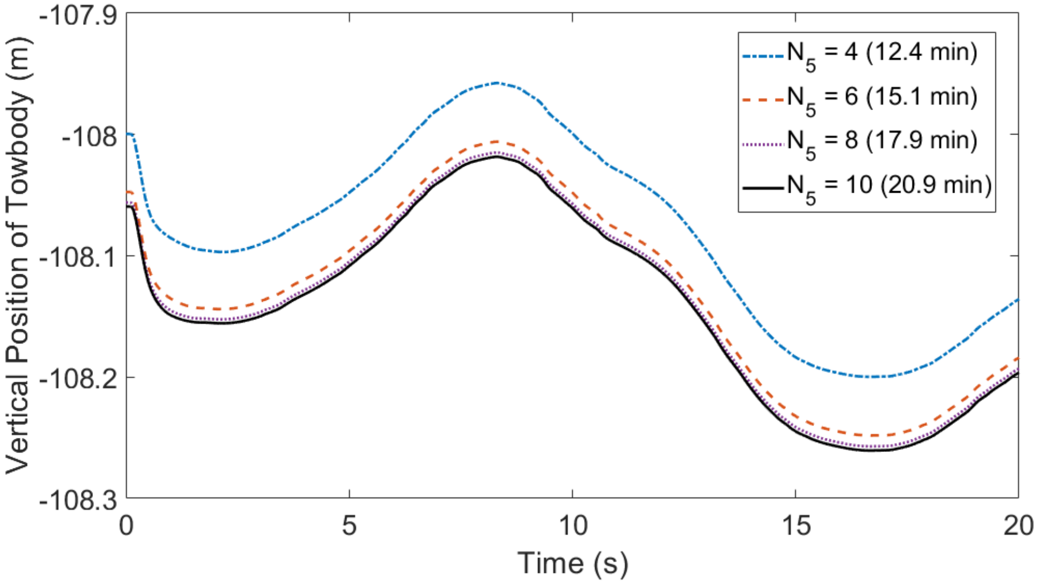

**Figure 44:** Vertical motion of towbody with number of elements in segment 5 varied. Computation times are shown in the legend.

For segment 3, the effect of the element size on the contact force distribution was considered. Figure 46 shows the contact force distribution as a function of the wrap angle measured from the vertical axis. The number of elements was varied from twenty to fifty. The distribution converges at approximately forty elements.

Since the contact forces between the cable and the winch are not specifically of

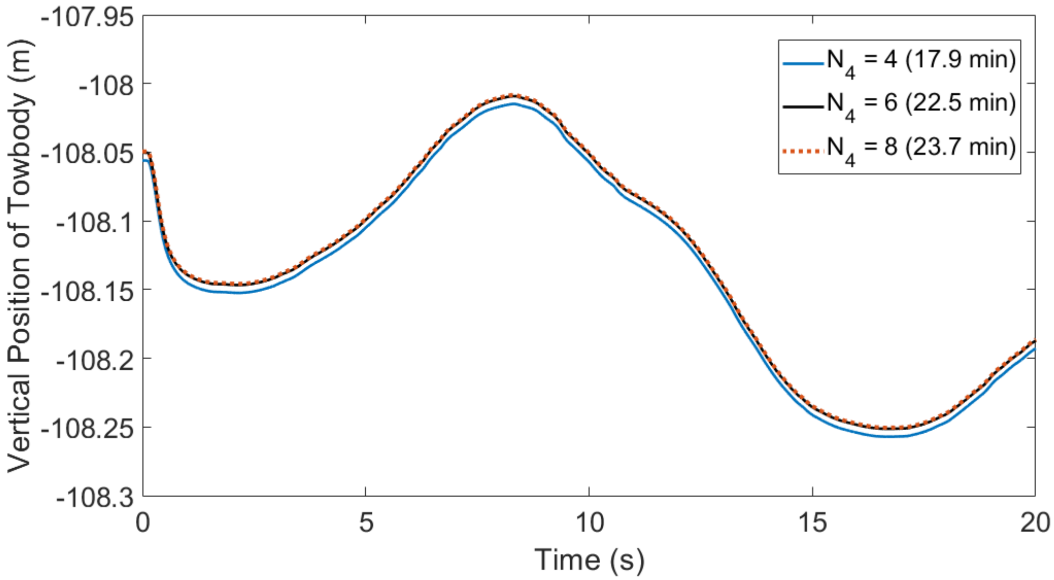

**Figure 45:** Vertical motion of towbody with number of elements in segment 4 varied. Computation times are shown in the legend.

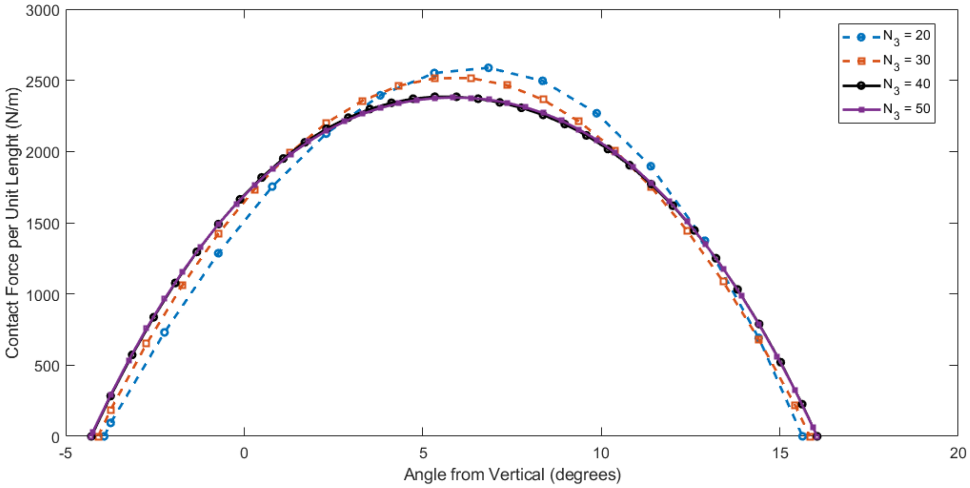

**Figure 46:** Contact force distribution as a function of angle with number of elements in segment 3 varied.

interest, the number of elements in segment 1 was set to 10. Additionally, segment 2 was not expected to undergo significant bending deformations and is mainly loaded in tension only, thus only five elements were used.

The convergence study demonstrated in this section uses a simplified mesh to assess the convergence in the towbody motion for Segments 4 and 5. The convergence in Segment 3 was assessed by examining only the contact distribution at equilibrium. Since Segments 1 and 2 were not expected to significantly influence the dynamics, the spatial convergence of those segments was not examined. The above procedure was selected in order to limit the total computation time required and make the analysis feasible on readily available hardware. If a significant amount of computational power is available, such as using a computer cluster, a more comprehensive convergence convergence analysis could be performed. For instance, the motion of the full system could be simulated while varying the number of elements in each of the five cable segments. The mesh could then be refined until the change in a particular variable of interest (e.g. the contact force between the cable and the sheave) is smaller than a desired tolerance.

## 5.5 Simulations and Results

Three test cases with different set point algorithms were considered in this analysis: no heave compensation, the simplified sheave algorithm, and the rigorous sheave algorithm. Table 9 lists the simulation parameters used.

| **Parameter** | **Value** |
|---|---|
| Nominal sheave angle, $\theta_{nom}$ | 74.0 deg |
| Winch proportional gain, $k_1$ | 250 |
| Winch derivative gain, $k_2$ | 50 |
| Contact stiffness, $k_N$ | $1 \times 10^6$ N/m |
| Integration points per element, $N_I$ | 10 |
| Constraint stabilization coefficients, $a_1 = a_2$ | 10 |

**Table 9:** Full scale simulation parameters.

Figure 47 shows the simulated towbody motion in the $XZ$ plane for the uncompensated case as a dotted blue line and for the simplified sheave test case as a solid orange line. No significant difference was observed between the simplified sheave and rigorous sheave cases since the variation in the sheave angle was small. Thus, only the results for the simplified sheave case are depicted. When considering all axes, the three-dimensional ellipsoid volume containing 95% of the data points was 0.197 $m^3$ for the uncompensated case, 0.021 $m^3$ for the simplified sheave case and 0.020 $m^3$ for the rigorous sheave case. The reduction in ellipsoid volume from the uncompensated case was 89.3 percent for the simplified sheave algorithm and 89.8 percent for the rigorous sheave algorithm. The reduction in the ellipsoid volume is comparable to the values found in the small scale simulations. The reductions in volume are nearly identical for the simplified and rigorous sheave algorithms, supporting Calnan's conclusion that real-time measurement of the sheave angle is not required for most applications [2].

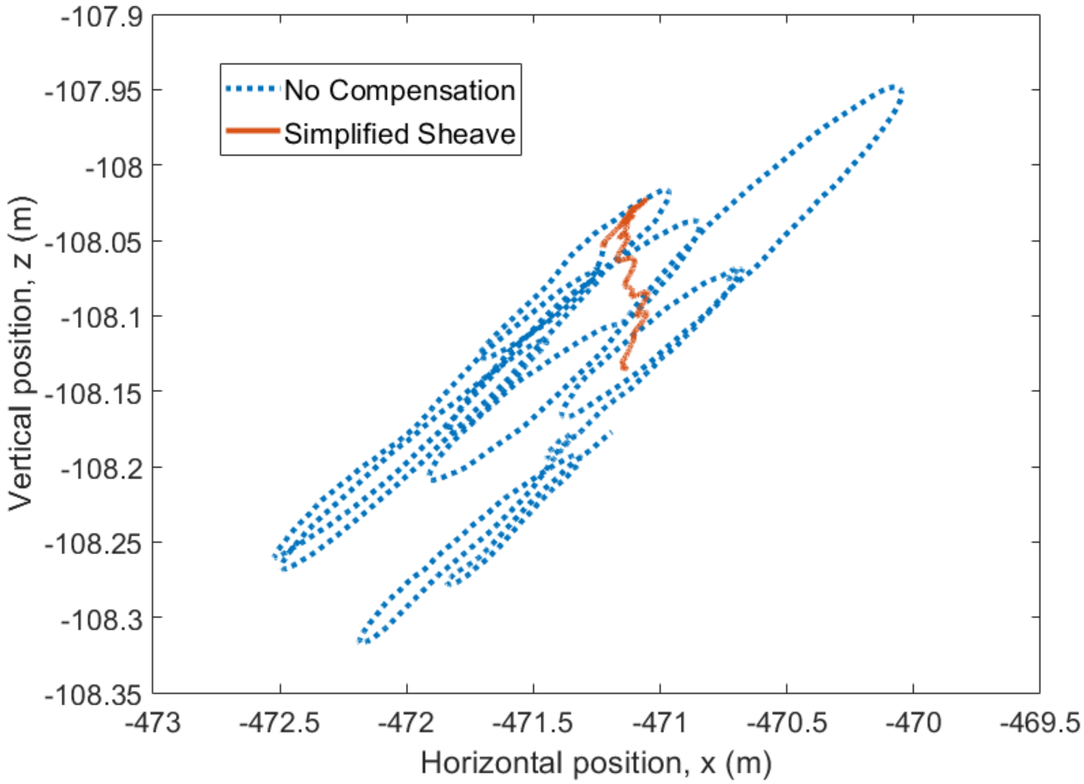

**Figure 47:** Towbody motion for uncompensated and simplified sheave test cases.

Figure 48 compares the cable tension at the sheave as a function of time for the uncompensated and simplified sheave test cases. The average cable tension was 3.71

kN in both cases. The inclusion of motion compensation has a significant effect on the simulated cable tension, reducing the standard deviation of the tension from 262.8 N in the uncompensated case to 23.5 N in the simplified sheave case. The tension ranged from 3.07 kN to 4.70 kN in the uncompensated case and from 3.50 kN to 2.83 kN with compensation. Without compensation, the drag acting on the cable and towbody induces a large variation in the cable tension as the ship moves. With compensation, the winch rotation reduces the variation by reeling cable out when the tension is increasing and reeling cable in when the tension is decreasing.

Figure 49 compares the total contact force between the cable and the sheave as a function of time for the uncompensated and simplified sheave test cases. Both cases demonstrate similar variations in the contact force with the force ranging from 1.24 kN to 2.03 kN in the uncompensated case and 1.28 kN to 2.08 kN in the compensated case. The standard deviation of the contact force is 140 N in the uncompensated case and 105 N in the compensated case.

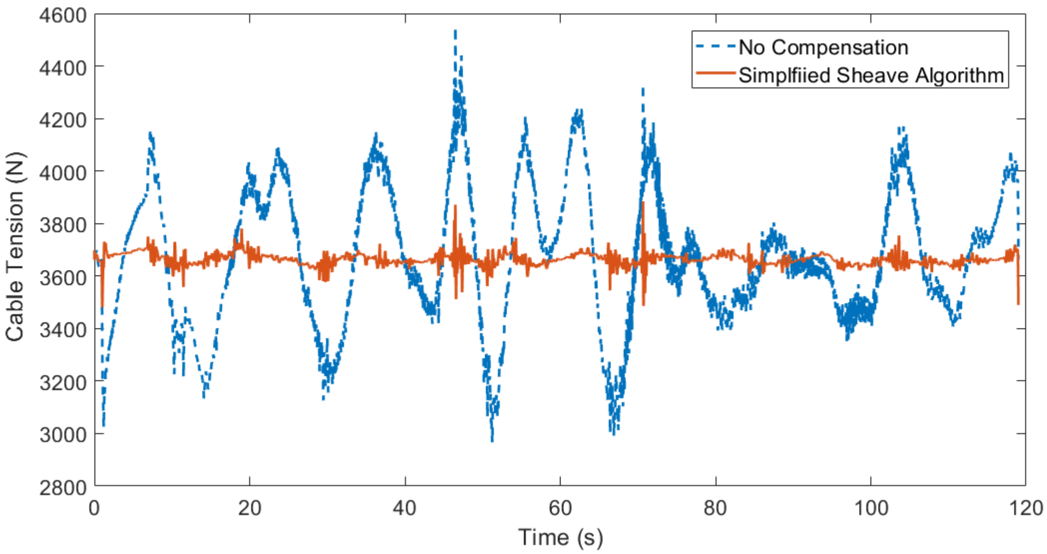

**Figure 48:** Cable tension at the sheave for uncompensated and simplified sheave test cases.

An additional case study was performed examining the effect of vortex-induced

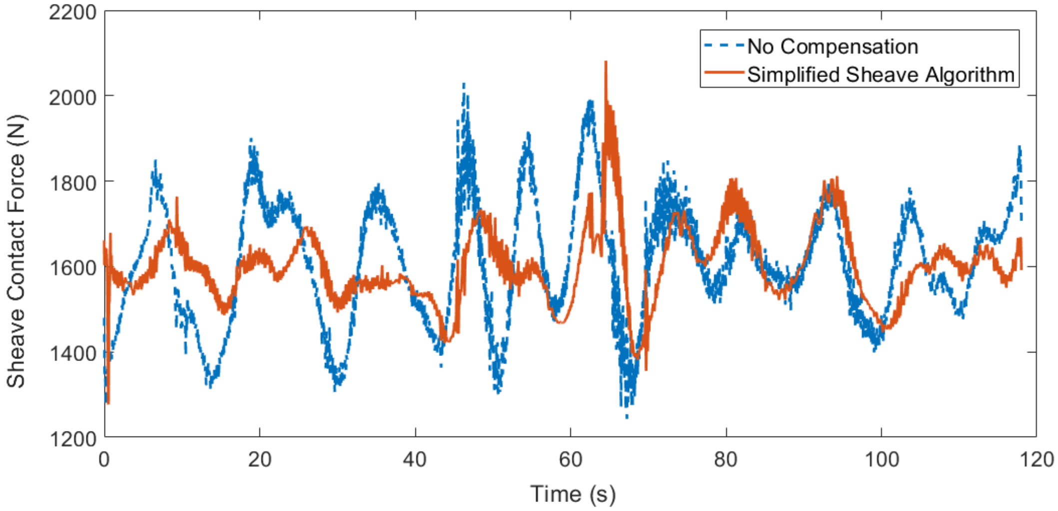

**Figure 49:** Total contact force between the cable and sheave for uncompensated and simplified sheave test cases.

vibration due to wind loading on a ship-board cable-sheave system. The study was published in a paper entitled "Vortex-Induced Vibrations of a Low-tension Cable-Sheave System Modeled using Nonlinear Finite Elements" by C. Westin and R.A Irani in the Proceedings of The Canadian Society for Mechanical Engineering International Congress 2018. Wind loading was found to have an insignificant effect on the cable dynamics. The complete study is given in Appendix A.

## 5.6 Summary

In this section, the full scale simulation of a towed cable system was demonstrated. The initialization of the model and the mesh convergence were outlined. Simulations were performed for three test cases consisting of no heave compensation, compensation using the simplified sheave algorithm and compensation using the rigorous sheave algorithm. The simulation demonstrated similar reductions in towbody motion as observed in the flume scale study in Section 4.3. Finally, the ability of the model to predict variations in cable tension and the contact force between the cable and the winch was demonstrated. In future work, the variations in the cable tension and contact forces predicted by the model can be used to examine cable detachment behavior during more severe towing conditions. The simulation could also be validated using experimental measurements of a full-scale system.

# 6 Conclusions

The key objectives of this thesis were:

1. To develop a three-dimensional finite element model of a flexible cable with winch and sheave surface interactions to simulate the cable dynamics of a towed-body system with active heave compensation.
2. To assess the performance of the model by comparing the simulated cable behavior with experimental measurements of small scale systems.
3. To demonstrate the capability of the simulation to exhibit dynamic contact behavior for a full scale system.

## 6.1 Objective One

In Chapter 3, the formulation of the cable model was described. The nonlinear absolute nodal coordinate formulation was used to model the cable dynamics. Existing formulations for the internal elastic forces, hydrodynamic loading and kinematic constraints were implemented. Also, an internal damping force model was developed using the Rayleigh dissipation function. *The main contributions of this thesis related to the first objective are the inclusion of winch and sheave contact in a towed-cable model and the development of a three-dimensional description of contact forces between the cable and the sheave and winch surfaces described in Section 3.4.* The model incorporates the three-dimensional geometry of the sheave, in order to accurately represent the contact forces as the ship undergoes motion along six degrees of freedom. A nonlinear contact penalty method was used to formulate the contact forces.

## 6.2 Objective Two

In Sections 4.1 and 4.2, the results of two experiments were presented and used to assess the accuracy of the simulation. In the first experiment, a cable-pulley system with a swinging load was used to verify the accuracy of the predicted cable tension and wrap angle of the cable around the pulley. In the second experiment, a system with a moving pulley simulating ship motion was used and the experimental and simulated cable tension were compared. The simulation demonstrated good agreement with the experimental wrap angle and tension measurements in the first experiment. The simulation demonstrated a significant level of error in predicting peak cable tension with a moving pulley, but the minimum tensions were predicted with good accuracy. In Section 4.3, existing experimental data of a small-scale towed body system with active heave compensation was used to further validate the model. The simulation demonstrated good agreement with the experimental towbody motion, predicting the volume of the enclosing ellipsoid volume to withing 2% for the un-compensated test case and within 27% for the cases with motion compensation. *The contribution of the thesis related to this objective is the validation of the cable model for systems where the contact wrap angle between the cable and the pulley undergoes large variations throughout the dynamic motion.* Peak-to-peak variations in the wrap angle up to 110 degrees were examined in Section 4.1.

## 6.3 Objective Three

In Chapter 5, the results of a case study of a full scale system were shown. The simulation was performed with and without heave compensation. The simulation demonstrated similar reductions in tow body motion using the active heave compensation algorithms as observed in the small scale experiments. The simulation was used to examine the variations in cable tension and contact between the cable and the winch during the motion of the ship. With compensation, the standard deviation in the tension was significantly reduced compared to the uncompensated case. *The contribution of the thesis related to this objective is the method outlined to examine the cable tension and contact forces during towing operations.* The method can be employed in future studies to examine detachment of the cable from the sheave during severe operating conditions.

## 6.4 Future Work

The following are suggestions for potential avenues of future work based on the work shown in this thesis:

1. Experimental quantification of the cable bending stiffness and elastic modulus can be used to improve the accuracy of the simulation.
2. Experimental measurements could be used to develop more accurate models for the hydrodynamic coefficients and loading functions for a given system and operating conditions.
3. A more accurate formulation of the internal elastic forces which captures complex behaviors of wire rope, such as shear deformation and nonlinear elasticity, could be implemented and compared to the current formulation.
4. In the current work the model is implemented in MATLAB using the built-in ODE solver *ode15s*. The numerical implementation of the model could be further developed by deriving the analytical Jacobian of the system and using alternative ODE solvers which can provide greater performance and numerical stability.
5. Full scale experiments could be performed to further validate the simulation.
6. A sensitivity analysis can be performed to assess the sensitivity of the model to various system parameters. The analysis can be used to identify which parame-

ters most significantly affect the simulation output. Further work can then also focus on the accurate determination of those parameters.

## 6.5 List of Publications

The following papers were published based on the work shown in this thesis:

1. Westin C., Irani R. A. (2018) “Vortex-Induced Vibrations of a Low-tension Cable-Sheave System Modeled using Nonlinear Finite Elements,” in *Proceedings of The Canadian Society for Mechanical Engineering International Congress 2018*, Toronto, Canada, May 27-30, 2018.
2. Westin C., Irani R. A. (2017) “Cable-Pulley Interaction with Dynamic Wrap Angle Using the Absolute Nodal Coordinate Formulation,” in *Proceedings of the 4th International Conference of Control, Dynamic Systems, And Robotics*, Toronto, Canada, August 21-23rd, 2017.

# References

[1] B. J. Buckham, “Dynamics modelling of low-tension tethers for submerged remotely operated vehicles,” PhD thesis, University of Victoria, 2003.

[2] C. Calnan, “Set-point algorithms for active heave compensation of towed bodies,” Master’s thesis, Dalhousie University, 2016.

[3] H. Sugiyama, A. M. Mikkola, and A. A. Shabana, “A non-incremental nonlinear finite element solution for cable problems,” in *ASME 2003 International Design Engineering Technical Conferences and Computers and Information in Engineering Conference*, American Society of Mechanical Engineers, 2003, pp. 171–181.

[4] G. Čepon, L. Manin, and M. Boltežar, “Introduction of damping into the flexible multibody belt-drive model: A numerical and experimental investigation,” *Journal of Sound and Vibration*, vol. 324, no. 1-2, pp. 283–296, 2009.

[5] G. Cepon, L. Manin, and M. Boltezar, “Validation of a flexible multibody belt-drive model,” *Strojniski Vestnik Journal of Mechanical Engineering*, vol. 57, pp. 539–546, 2011.

[6] J. Seo, S. Kim, I. Jung, *et al.*, “Dynamic analysis of a pantograph–catenary system using absolute nodal coordinates,” *Vehicle System Dynamics*, vol. 44, no. 8, pp. 615–630, 2006.

[7] U. Lugrís, J. Escalona, D. Dopico, and J. Cuadrado, “Efficient and accurate simulation of the cable-pulley interaction in weight-lifting machines,” in *Proceedings of the 1st Joint International Conference on Multibody System Dynamics, Lappeenranta, Finland*, 2010.

[8] S. Takehara, M. Kawarada, and K. Hase, “Dynamic contact between a wire rope and a pulley using absolute nodal coordinate formulation,” *Machines*, vol. 4, no. 1, p. 4, 2016.

[9] R. Bulín, M. Hajžman, and P. Polach, “Nonlinear dynamics of a cable-pulley system using the absolute nodal coordinate formulation,” *Mechanics Research Communications*, vol. 82, pp. 21–28, 2017.

[10] E. Imanishi, T. Nanjo, and T. Kobayashi, “Dynamic simulation of wire rope with contact,” *Journal of mechanical science and technology*, vol. 23, no. 4, pp. 1083–1088, 2009.

[11] P. Wriggers and G. Zavarise, “Computational contact mechanics,” in *Encyclopedia of Computational Mechanics*, Wiley Online Library, 2004.

[12] S. Takehara, Y. Terumichi, and K. Sogabe, “Motion of a submerged tether subject to large deformations and displacements,” *Journal of System Design and Dynamics*, vol. 5, no. 2, pp. 296–305, 2011.

[13] J. Park and N. Kim, “Dynamics modeling of a semi-submersible autonomous underwater vehicle with a towfish towed by a cable,” *International Journal of Naval Architecture and Ocean Engineering*, vol. 7, no. 2, pp. 409–425, 2015.

[14] C. Calnan, R. J. Bauer, and R. A. Irani, “Controller design and motion compensation for marine towed bodies,” in *OCEANS 2016 MTS/IEEE Monterey*, IEEE, 2016, pp. 1–9.

[15] C. Calnan, R. J. Bauer, and R. A. Irani, “Reference-point algorithms for active motion compensation of towed bodies,” *IEEE Journal of Oceanic Engineering*, (In Press).

[16] C. Ablow and S. Schechter, “Numerical simulation of undersea cable dynamics,” *Ocean Engineering*, vol. 10, no. 6, pp. 443–457, 1983.

[17] M. Triantafyllou and C. Howell, "Dynamic response of cables under negative tension: An ill-posed problem," *Journal of Sound and Vibration*, vol. 173, no. 4, pp. 433–447, 1994.

[18] J. Winget and R. Huston, "Cable dynamics – a finite segment approach," *Computers & Structures*, vol. 6, no. 6, pp. 475–480, 1976.

[19] E. Hinton, T. Rock, and O. Zienkiewicz, "A note on mass lumping and related processes in the finite element method," *Earthquake Engineering & Structural Dynamics*, vol. 4, no. 3, pp. 245–249, 1976.

[20] R. Driscoll and M. Nahon, "Mathematical modeling and simulation of a moored buoy system," in *OCEANS'96. MTS/IEEE Conference Proceedings. Prospects for the 21st Century.*, IEEE, vol. 1, 1996, pp. 517–523.

[21] J. W. Kamman and R. L. Huston, "Modelling of submerged cable dynamics," *Computers & Structures*, vol. 20, no. 1-3, pp. 623–629, 1985.

[22] J. W. Kamman and R. L. Huston, "Multibody dynamics modeling of variable length cable systems," *Multibody System Dynamics*, vol. 5, no. 3, pp. 211–221, 2001.

[23] A. A. Shabana, "Flexible multibody dynamics: Review of past and recent developments," *Multibody System Dynamics*, vol. 1, no. 2, pp. 189–222, 1997.

[24] J. S. Archer, "Consistent mass matrix for distributed mass systems," *Journal of the Structural Division*, vol. 89, no. 4, pp. 161–178, 1963.

[25] O. Dmitrochenko, "Finite elements using absolute nodal coordinates for large-deformation flexible multibody dynamics," *Journal of Computational and Applied Mathematics*, vol. 215, no. 2, pp. 368–377, 2008.

[26] K. Nachbagauer, "Development of shear and cross section deformable beam finite elements applied to large deformation and dynamics problems," in *2nd ECCOMAS Young Investigators Conference (YIC 2013)*, 2013.

[27] J. Gerstmayr, H. Sugiyama, and A. Mikkola, "Review on the absolute nodal coordinate formulation for large deformation analysis of multibody systems," *Journal of Computational and Nonlinear Dynamics*, vol. 8, no. 3, 2013.

[28] N. Karathanasopoulos, "On the analysis, simulation and structural design of helical constructions," PhD thesis, ETH Zurich, 2015.

[29] M. Berzeri and A. A. Shabana, "Development of simple models for the elastic forces in the absolute nodal co-ordinate formulation," *Journal of Sound and Vibration*, vol. 235, no. 4, pp. 539–565, 2000.

[30] B. M. Sumer and J. Fredsøe, *Hydrodynamics around Cylindrical Strucures.* Singapore: World Scientific, 2006.

[31] D. C. Cotter and S. K. Chakrabarti, "Wave force tests on vertical and inclined cylinders," *Journal of waterway, port, coastal, and ocean engineering*, vol. 110, no. 1, pp. 1–14, 1984.

[32] Y. Choo and M. J. Casarella, "Hydrodynamic resistance of towed cables," *Journal of Hydronautics*, vol. 5, no. 4, pp. 126–131, 1971.

[33] S. Goldstein, *Modern Developments in Fluid Dynamics.* London: Clarendon Press, 1938, vol. 2.

[34] A. Kozakiewicz, J. Fredsøe, B. M. Sumer, *et al.*, "Forces on pipelines in oblique attack: Steady current and waves," in *The Fifth international Offshore and Polar Engineering Conference*, International Society of Offshore and Polar Engineers, 1995.

[35] Y. Choo and M. J. Casarella, "Configuration of a towline attached to a vehicle moving in a circular path," *Journal of Hydronautics*, vol. 6, no. 1, pp. 51–57, 1972.

[36] B. Buckham, M. Nahon, M. Seto, X. Zhao, and C. Lambert, "Dynamics and control of a towed underwater vehicle system, part I: Model development," *Ocean Engineering*, vol. 30, no. 4, pp. 453–470, 2003.

[37] C. Lambert, M. Nahon, B. Buckham, and M. Seto, "Dynamics and control of towed underwater vehicle system, part II: Model validation and turn maneuver optimization," *Ocean engineering*, vol. 30, no. 4, pp. 471–485, 2003.

[38] F. Sun, Z. Zhu, and M. LaRosa, "Dynamic modeling of cable towed body using nodal position finite element method," *Ocean Engineering*, vol. 38, no. 4, pp. 529–540, 2011.

[39] S. Takehara, Y. Terumichi, and K. Sogabe, "Motion of a submerged tether subject to large deformations and displacements," *Journal of System Design and Dynamics*, vol. 5, no. 2, pp. 296–305, 2011.

[40] K. Kim, J. Lee, and W. Yoo, "The motion and deformation rate of a flexible hose connected to a mother ship," *Journal of Mechanical Science and Technology*, vol. 26, no. 3, pp. 703–710, 2012.

[41] J. Park and N. Kim, "Dynamics modeling of a semi-submersible autonomous underwater vehicle with a towfish towed by a cable," *International Journal of Naval Architecture and Ocean Engineering*, vol. 7, no. 2, pp. 409–425, 2015.

[42] M. Machado, P. Moreira, P. Flores, and H. M. Lankarani, "Compliant contact force models in multibody dynamics: Evolution of the hertz contact theory," *Mechanism and Machine Theory*, vol. 53, pp. 99–121, 2012.

[43] H. Hertz, "On the contact of solid elastic bodies and on hardness," *Journal of Math*, vol. 92, pp. 156–171, 1881.

[44] S. Kim, "Contact dynamics and force control of flexible multi-body systems," PhD thesis, McGill University Libraries, 1999.

[45] M. J. Leamy and T. M. Wasfy, “Transient and steady-state dynamic finite element modeling of belt-drives,” *Journal of Dynamic Systems, Measurement, and Control*, vol. 124, no. 4, pp. 575–581, 2002.

[46] T. M. Wasfy and M. Leamy, “Effect of bending stiffness on the dynamic and steady-state responses of belt-drives,” in *ASME 2002 International Design Engineering Technical Conferences and Computers and Information in Engineering Conference*, American Society of Mechanical Engineers, 2002, pp. 217–224.

[47] K. S. Kerkkänen, D. García-Vallejo, and A. M. Mikkola, “Modeling of belt-drives using a large deformation finite element formulation,” *Nonlinear Dynamics*, vol. 43, no. 3, pp. 239–256, 2006.

[48] F. Pfeiffer and C. Glocker, *Multibody dynamics with unilateral contacts.* John Wiley & Sons, 1996, vol. 9.

[49] J. G. De Jalon and E. Bayo, *Kinematic and dynamic simulation of multibody systems: the real-time challenge.* Springer Science & Business Media, 2012.

[50] J. Munoz, “Modelling unilateral frictionless contact using the null-space method and cubic b-spline interpolation,” *Computer Methods in Applied Mechanics and Engineering*, vol. 197, no. 9-12, pp. 979–993, 2008.

[51] Y. Peng, Y. Wei, and M. Zhou, “Efficient modeling of cable-pulley system with friction based on arbitrary-lagrangian-eulerian approach,” *Applied Mathematics and Mechanics*, vol. 38, no. 12, pp. 1785–1802, 2017.

[52] S. Takehara, M. Kawarada, and K. Hase, “Dynamic contact between a wire rope and a pulley using absolute nodal coordinate formulation,” *Machines*, vol. 4, no. 1, p. 4, 2016.

[53] N. N. Khude, “Efficient simulation of flexible body systems with frictional contact/impact,” PhD thesis, University of Wisconsin-Madison, 2015.

[54] Z. Yue, Z. Yang, *et al.*, "The strain coupling problem and model decoupling of ANCF cable/beam element," *Chinese Journal of Theoretical and Applied Mechanics*, vol. 48, no. 6, p. 1406, 2016.

[55] O. Aamo and T. Fossen, "Finite element modelling of moored vessels," *Mathematical and Computer Modelling of Dynamical Systems*, vol. 7, no. 1, pp. 47–75, 2001.

[56] M. Liu and D. G. Gorman, "Formulation of Rayleigh damping and its extensions," *Computers & Structures*, vol. 57, no. 2, pp. 277–285, 1995.

[57] D. Yoerger, M. Grosenbaugh, M. Triantafyllou, and J. Burgess, "Drag forces and flow-induced vibrations of a long vertical tow cable – part I: Steady-state towing conditions," *Journal of Offshore Mechanics and Arctic Engineering*, vol. 113, no. 2, pp. 117–127, 1991.

[58] J. K. Vandiver *et al.*, "Drag coefficients of long flexible cylinders," in *Offshore Technology Conference*, Offshore Technology Conference, 1983.

[59] K. H. Hunt and F. R. E. Crossley, "Coefficient of restitution interpreted as damping in vibroimpact," *Journal of Applied Mechanics*, vol. 42, no. 2, pp. 440–445, 1975.

[60] A. A. Shabana, *Dynamics of multibody systems*, 3rd ed. Cambridge, UK: Cambridge University Press, 2010.

[61] D. J. Braun and M. Goldfarb, "Eliminating constraint drift in the numerical simulation of constrained dynamical systems," *Computer Methods in Applied Mechanics and Engineering*, vol. 198, no. 37-40, pp. 3151–3160, 2009.

[62] M. Hajžman and P. Polach, "Application of stabilization techniques in the dynamic analysis of multibody systems," *Applied and Computational Mechanics*, vol. 1, no. 2, pp. 479–488, 2007.

[63] C. Westin and R. A. Irani, "Cable-pulley interaction with dynamic wrap angle using the absolute nodal coordinate formulation," in *Proceedings of the 4th International Conference on Control, Dynamic Systems, and Robotics, Toronto, Canada*, 2017.

[64] M. Jenkins and N. Mills, *Plastics: Microstructure and Engineering Applications.* Elsevier, 2005, p. 442.

[65] A. M. Arney, "FFG-7 ship motion and airwake trial. part II. removal of ship motion effects from measured airwake data.," Defence Science and Technology Organization, Melbourne, Australia, Tech. Rep., 1994.

[66] R. D. Blevins, *Formulas for Dynamics, Acoustics and Vibration.* John Wiley & Sons, 2015.

[67] MatWeb, *Overview of materials for nylon 66, unreinforced*, [Online] Available: `http://www.matweb.com/search/datasheet.aspx?matguid=a2e79a3451984d58a8a442c37a226107`, 2018.

[68] "U.S. Navy wire-rope handbook volume 1," Naval Sea Systems Command, Tech. Rep. ADA955305, 1976.

[69] K. Spak, G. Agnes, and D. Inman, "Cable parameters for homogenous cable-beam models for space structures," in *Dynamics of Civil Structures*, vol. 4, Springer, 2014, pp. 7–18.

[70] N. Barbieri, O. H. de Souza Junior, and R. Barbieri, "Dynamical analysis of transmission line cables. part 1 – linear theory," *Mechanical Systems and Signal Processing*, vol. 18, no. 3, pp. 659–669, 2004.

[71] Z. Zhu and S. Meguid, "Nonlinear fe-based investigation of flexural damping of slacking wire cables," *International Journal of Solids and Structures*, vol. 44, no. 16, pp. 5122–5132, 2007.

[72] R. Folb and J. Nelligan, “Investigation of the hydrodynamic loading on ribbon towcable,” Applied Research of Cambridge Ltd, Tech. Rep., 1982.

[73] S. F. Hoerner, *Fluid-Dynamic Drag: Theoretical, Experimental and Statistical information*. Hoerner Fluid Dynamics, 1965.

[74] J. D. Anderson Jr, *Fundamentals of Aerodynamics*. Tata McGraw-Hill Education, 2010.

[75] R. Skop, O. Griffin, and S. Ramberg, “Seacon II strumming predictions.,” Naval Research Laboratory, Washington, DC, Tech. Rep., 1976.

[76] R. Gabbai and H. Benaroya, “An overview of modeling and experiments of vortex-induced vibration of circular cylinders,” *Journal of Sound and Vibration*, vol. 282, no. 3, pp. 575–616, 2005.

[77] X. Bai and W. Qin, “Using vortex strength wake oscillator in modelling of vortex induced vibrations in two degrees of freedom,” *European Journal of Mechanics-B/Fluids*, vol. 48, pp. 165–173, 2014.

[78] M. Ciftci, “Flexible multibody analysis using absolute nodal coordinate formulation,” Master’s thesis, Middle East Technical University, Ankara, Turkey, 2014.

[79] L. Kübler, P. Eberhard, and J. Geisler, “Flexible multibody systems with large deformations and nonlinear structural damping using absolute nodal coordinates,” *Nonlinear Dynamics*, vol. 34, no. 1-2, pp. 31–52, 2003.

[80] I. Chowdhury and S. P. Dasgupta, “Computation of rayleigh damping coefficients for large systems,” *The Electronic Journal of Geotechnical Engineering*, vol. 8, no. 0, pp. 1–11, 2003.

[81] M. L. Facchinetti, E. De Langre, and F. Biolley, “Coupling of structure and wake oscillators in vortex-induced vibrations,” *Journal of Fluids and structures*, vol. 19, no. 2, pp. 123–140, 2004.

[82] N. Al-Raheimy, “Free vibration of simply supported beam subjected to axial force,” *J Babylon Univ Eng Sci*, vol. 20, no. 1, pp. 301–315, 2012.

# A Analysis of Vortex-Induced Vibrations

The following work was published in Proceedings of The Canadian Society for Mechanical Engineering International Congress 2018 as “Vortex-Induced Vibrations of a Low-tension Cable-Sheave System Modeled using Nonlinear Finite Elements,” by C. Westin and R.A. Irani.

## A.1 Introduction

Cable-sheave systems are commonly used in marine applications for towing and lifting. The cable is subjected to highly dynamic loading due to the ship motion, hydrodynamic forces and wind loading which can result in the cable falling off the sheave. Cables exposed to external fluid flow experience vortex induced vibrations (VIV) resulting from the periodic shedding of vortices in the cables wake. The vortex shedding produces oscillating lifting and drag forces on the cable, which can excite a resonance response in the cable if the shedding frequency matches the fundamental frequency of the cable. Excessive cable vibrations can result in wear of both the cable and the sheave and possible detachment of the cable from a sheave. It is thus useful to quantify the vibration amplitudes due to wind loading using a dynamic model and assess the potential for vortex shedding to lead to cable detachment.

Gabbai and Benaraoya [76] give an overview of the various modeling approaches used to predict the response of cylinders to the vortex shedding forces. One modelling approach known as a wake-oscillator model utilizes a second order differential equation, such as the Van der Pol equation, to represent the flow in the wake. The oscillator is coupled with the structural dynamics of the cable using forcing terms in both equations. This modelling approach does not require numerical modeling of the flow field and can be easily incorporated into existing dynamic cable models. Exiting studies of cable vibrations using wake oscillator models typically utilize continuous equations to represent the cable structural dynamics. The coupling of wake-oscillator models to finite element cable models has not been extensively studied. Additionally, the researchers have not found any studies incorporating both VIV and cable-sheave interactions.

This paper presents the construction of a finite element model using the absolute nodal coordinate formulation (ANCF). The model has been developed to include three dimension contact with the sheave grooves. Additionally, oscillating lift and drag forces using an existing wake-oscillator model [77] have been incorporated. Cases of low cable tension are considered as cable detachment is more likely to occur when the cable is slack. Section A.2 of the paper describes the cable model and the formulation of the external forces. Case studies examining the potential for VIV to lead to cable detachment are presented in Section A.3. The paper ends with concluding remarks in Section A.4.

## A.2 Finite Element and External Load Model

The finite element model is comprised of $N$ two node cable elements. Each node has 6 degrees of freedom consisting of a position vector and a vector tangent to the cable centerline. All degrees of freedom are defined in the absolute coordinate frame. An additional parameter $p \in [0, l]$ is used to interpolate between nodes. The absolute coordinates $\mathbf{r}$ of a point on the cable is defined using a vector of generalized coordinate $\mathbf{q}$ and a cubic shape function $\mathbf{S}(p)$ which interpolates between the nodes of each element:

$$\mathbf{r}(p) = \mathbf{S}(p)\mathbf{q} = [x \quad y \quad z]^T. \tag{A1}$$

For a fully parameterized ANCF beam element of unstretched length $l$, the generalized coordinates consist of the Cartesian coordinates $\mathbf{r}$ and the parametric slopes

$\partial \mathbf{r}/\partial p$ at each node:

$$\mathbf{q} = \begin{bmatrix} \mathbf{r}_1{}^T & (\partial \mathbf{r}/\partial p)_1{}^T & \mathbf{r}_2{}^T & (\partial \mathbf{r}/\partial p)_2{}^T \end{bmatrix}^T \tag{A2}$$

where subscripts 1 and 2 represent the respective nodes of the element or parameter values of $p = 0$ and $p = l$, respectively. The shape function representing a cubic spline is

$$\mathbf{S}(p) = \begin{bmatrix} (1 - 3(p/l)^2 + 2(p/l)^3)\,\mathbf{I} \\ ((p/l) - 2(p/l)^2 + (p/l)^3)\,\mathbf{I} \\ (3(p/l)^2 - 2(p/l)^3)\,\mathbf{I} \\ ((p/l)^2 - (p/l)^3)\,\mathbf{I} \end{bmatrix}^T \tag{A3}$$

where $\mathbf{I}$ is a 3x3 identity matrix.

The standard form of the Newton-Euler equations are given for a single element as

$$\mathbf{M}\ddot{\mathbf{q}} + \mathbf{K}\mathbf{q} + \mathbf{C}\dot{\mathbf{q}} - \mathbf{Q} = 0, \tag{A4}$$

where $\mathbf{M}$ is the mass matrix, $\mathbf{K}$ is the elastic stiffness matrix, $\mathbf{C}$ is the damping matrix, $\mathbf{Q}$ is an external force vector, and $\mathbf{q}$ is the vector of generalized coordinates defined in Equation A2. The equations of motion for the full system are formulated from Equation A4 using the embedding technique described in [60]. The Newton-Euler equations are solved using a numerical ODE integrator to determine the cable motion over time. The matrices $\mathbf{M}$, $\mathbf{K}$ and $\mathbf{C}$ and force vector $\mathbf{Q}$ will be defined in the following sections.

### Mass Matrix

Using a variational mass lumping approach the mass matrix is derived directly from the element kinetic energy [23] and is given by

$$\mathbf{M} = \frac{\partial^2 E_T}{\partial \dot{\mathbf{q}} \partial \dot{\mathbf{q}}} = \int_0^l \rho A \mathbf{S}(\mathbf{p})^T \mathbf{S}(\mathbf{p}) dp \tag{A5}$$

where $E_T$ is the kinetic energy of the element, $\rho$ is the cable density and $A$ is the cable cross-sectional area.

### Stiffness

Similarly, the stiffness matrix is derived from the strain energy $E_S$ of the element given by [29]:

$$E_S = \frac{1}{2} \int_0^l \left[ EA\epsilon_l^2(p) + EI\kappa^2(p) \right] dp \tag{A6}$$

where $E$ is the Young's modulus of the cable material, $A$ is the cross-sectional area, $I$ is the second moment of area, $\epsilon_l$ is the longitudinal strain, and $\kappa$ is the curvature of the element. The internal stiffness force is then given by the derivative of the strain energy with respect to the coordinate vector $\mathbf{q}$. The force vector can by separated into longitudinal and transverse components, $\mathbf{Q}_l$ and $\mathbf{Q}_t$. In order to simplify the computation of these forces it is assumed that the longitudinal strain $\epsilon_l$ is small and also constant throughout the element. The forces can then be derived as shown by Berzeri et al. [29]:

$$\mathbf{Q_l} = \left[ EA\epsilon_l \int_0^l \mathbf{S}'^T \mathbf{S}' dp \right] \mathbf{q} \tag{A7}$$

where $\mathbf{S}'$ is the derivative of $\mathbf{S}$ with respect to the parameter $p$. The longitudinal strain is determined from the arc length $s$ of the element [63]:

$$\epsilon_l(\mathbf{q}) = \frac{s(\mathbf{q}) - l}{l} \tag{A8}$$

where $s$ is the arc length and $l$ is the unstretched element length. The arc length is defined by integrating the norm of $\partial\mathbf{r}/\partial p$ with respect to $p$ over the length of the element [78]. The arc length $s$ is approximated using a numerical quadrature

$$s(\mathbf{q}) = \sum_{i=1}^{N_I} w_i \sqrt{\mathbf{r}'(p_i)^T \mathbf{r}'(p_i)} \frac{l}{N_I} \tag{A9}$$

where $i$ denotes the integration point, $N_I$ is the total number of integration points, $w_i$ is the quadrature weight. The trapezoidal rule is used with quadrature weights defined

$$w_i = \begin{cases} 0.5, & i = 1,\, N_I \\ 1, & i = 2,\, 3,\, \ldots,\, N_I - 1 \end{cases} \tag{A10}$$

The transverse stiffness force $\mathbf{Q}_t$ is defined [29]

$$\mathbf{Q}_t = \left[ \int_0^l EI\mathbf{S}''^T \mathbf{S}'' dp \right] \mathbf{q} \tag{A11}$$

where $I$ is the second moment of area. The general stiffness matrix $\mathbf{K}$ from Equation A4 is then given by

$$\mathbf{K} = \int_0^l EI\mathbf{S}''^T \mathbf{S}'' dp + \epsilon_l(\mathbf{q}) EA \int_0^l \mathbf{S}'^T \mathbf{S}' dp. \tag{A12}$$

### Damping

The damping matrix $\mathbf{C}$ from Equation A4 serves both to include energy dissipation and attenuate high frequency vibrational modes. The cable model uses the Rayleigh-damping approach [79], wherein the damping matrix is defined as a linear combination of the mass and stiffness matrices:

$$\mathbf{C} = \alpha\mathbf{M} + \beta\mathbf{K} \tag{A13}$$

where $\alpha$ and $\beta$ are scalar damping coefficients. The mass-proportional damping term represents external viscous damping while the stiffness-proportional damping term represents internal frictional damping. Since the external fluid damping can be incorporated into the aerodynamic drag force, the mass-proportional term will be neglected by setting $\alpha$ equal to zero.

Given a specified damping ratio $\xi$, the corresponding value of the remaining coefficient $\beta$ is given by [80]

$$\beta = 2\xi\frac{1}{\omega_n} \tag{A14}$$

where $\omega_n$ is the natural frequency of the cable.

### Contact Force

In order to model the cable-sheave interaction, a contact penalty is used. The cable is allowed to "penetrate" the sheave surface and the normal force os defined as a function of the of the relative penetration $\delta$. The normal force per unit length $\mathbf{f}_N$ acting at a single point on the element is defined using the Hunt-Crossley model [59], which represents the surface as a non-linear spring-damper:

$$\mathbf{f}_N = k_N\delta^n(1 + D\dot{\delta})\mathbf{u}_n \tag{A15}$$

where $\mathbf{u}_n$ is the unit vector normal to the sheave surface at the point of contact, $k_N$ is the contact stiffness, $\delta$ is the relative "penetration" of the node into the surface, $D$ is a damping coefficient and $n$ is a positive constant with a value between 1 and 1.5 from the Hertz contact theory [43]. In the present analysis, a contact stiffness of

$1.5{\times}10^7$ N/m and a value of $n$ of 1.5 is used based on the values used by Bulin et al [9] and the researchers' previous work [63].

The radius of curvature of the groove is assumed to be equal to the radius of the cable. Two surfaces are then defined that intersect at the center of curvature of the groove. In the cross-sections shown in Figure A1, the two surfaces can be considered straight lines (shown as solid lines) parallel to the straight walls of the groove (shown as dotted lines). If the cable lies below either of the lines, a penalty force is produced proportional to the penetration of the cable node into the surface. If the cable node lies above both lines, no normal force is applied. The contact penalty is illustrated in Figure A1. The normal force per unit length is evaluated at $N_I$ discrete points points per element. The generalized distributed force in the element coordinates is then calculated from the discrete force distribution.

### Drag Force

The drag force per unit length acting at a given point on the cable

$$\mathbf{f}_D = -\frac{1}{2}C_D\rho_w d|\mathbf{V}_n|\mathbf{V}_n \tag{A16}$$

where $C_D$ is the drag coefficient, $d$ is the cable diameter, $\mathbf{V}_n$ is the normal component of the relative velocity $V$, and $\mu$ is the dynamic viscosity of the fluid. The relative

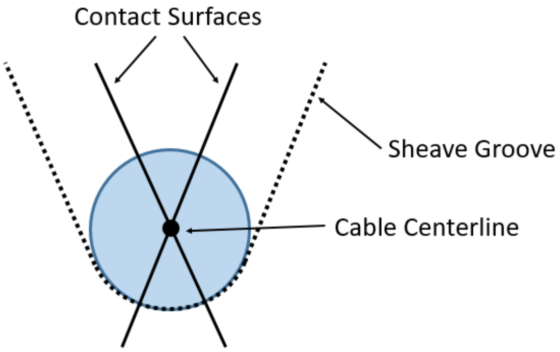

**Figure A1:** Sheave groove cross-section velocity and its normal component are calculated as follows:

$$\mathbf{V} = \dot{\mathbf{r}} - \mathbf{U} \tag{A17a}$$

$$\mathbf{V}_t = (\mathbf{V} \cdot \mathbf{u}_t)\mathbf{u}_t \tag{A17b}$$

$$\mathbf{V}_n = \mathbf{V} - \mathbf{V}_t \tag{A17c}$$

where $\mathbf{U}$ is the velocity of the free stream, $\dot{\mathbf{r}}$ is the velocity of the point on cable centerline. The unit vector tangent to the cable centerline $\mathbf{u}_t$ is equivalent to $\frac{\mathbf{r}'}{|\mathbf{r}'|}$. The drag coefficient $C_D$ is given by

$$C_D = 1.1 + 4Re^{0.8}, \quad 30 < Re < 10^5 \tag{A18}$$

where $Re$ is the Reynolds number.

### Wake Oscillator Model

A two-degree of freedom wake-oscillator developed by Bai and Qin [77] is used to describe the vortex shedding forces on the cable. The variable $w(t)$ is introduced, with the function $d^2\dot{w}(t)$, where $d$ is the cable diameter, corresponding to the vortex strength of the wake. The evolution of $w$ over time satisfies a van der Pol equation of the form

$$\ddot{w} + a_1\omega_{st}\left[1 - \frac{a_2(\dot{w})^2}{\omega_{st}^2}\right]\dot{w} + \omega_{st}w = \frac{a_3\omega_{st}}{d}\dot{Y} \tag{A19}$$

where $a_1, a_2$ and $a_3$ are empirical parameters, $\omega_{st}$ is the Strouhal frequency in rad/s, and $Y$ is the displacement of the cable in the cross-flow direction. Typical values for $a_1, a_2$ and $a_3$, proposed by Facchinetti [81] and Bai and Qin [77] are 0.3, 0.2 and 12, respectively.

The force acting on the structure due to the vortex shedding is then evaluated:

$$f_{SW} = -\frac{C_{D0}\rho d^4}{32\pi^3 St^3 U}\dot{w}\ddot{w} \tag{A20a}$$

$$f_{CF} = \frac{C_{L0}\rho U d^2}{8\pi St}\dot{w} \tag{A20b}$$

where $f_{SW}$ is the force per unit length acting in the stream-wise direction, $f_{CF}$ is the force per unit length acting in the cross-flow direction, $C_{D0}$ and $C_{L0}$ are the drag and lift coefficients associated with the vortex shedding, with assumed values of 0.2 and 0.3, respectively. In the absolute coordinate frame, the cross-flow direction corresponds to the y-axis, while the stream-wise direction corresponds to the z-axis.

For each node on the cable exposed to the wind as shown in Fig. A2, a degree of freedom representing the wake variable $w$ is added to the system equations of motion. The wake coefficients are interpolated linearly to provide the discrete force distributions along each element.

### Total Distributed Force

The force distributions determined for the normal contact, stationary drag and oscillating drag and lift are added together to give the total force distribution $\mathbf{f}$. The force acting on the element in the element coordinates $\mathbf{Q}$ is then found by integrating over the length of the cable element:

$$\mathbf{Q} = \int_0^l \mathbf{S}(p)^T \mathbf{f}\, dp. \tag{A21}$$

Again, a numerical quadrature is used to approximate the integral:

$$\mathbf{Q} = \sum_{i=1}^{N_I} w_i \mathbf{S}(p)^T \mathbf{f}_i \frac{l}{N_I} \tag{A22}$$

where $i$ denotes the integration point, $N_I$ is the total number of integration points and $w_i$ is the quadrature weight. Ten integration points per element were used for all simulations described in this report.

The gravitational body forces are defined similarly with $\mathbf{f} = \begin{bmatrix} 0 & -\rho A g & 0 \end{bmatrix}^T$ where $\rho$ is the cable density and $g$ is the acceleration due to gravity. Since the gravitational force is constant, the integration can be performed symbolically using Equation A21 prior to the simulation.

## A.3 Case Studies

### Model Parameters

The system consists of a cable suspended by two identical sheaves. Each cable end is attached to a point mass as shown in Fig. A2. The static drag and oscillating lift and drag are applied only to the portion of the cable suspended between the two sheaves. A number of case studies were performed. The system properties used for the simulations are listed in Table A1. The cable properties used are for a wire rope with 6x37 construction, commonly used for marine lifting and hoisting applications, given in [68]. The sheave diameters are calculated using the minimum recommended sheave-to-rope diameter ratio of 18 [68].

Values for the cable bending stiffness $EI$ and damping ratio $\xi$ are not readily available, thus conservative values were used. A minimum bending stiffness value can be calculated by neglecting the friction between individual wires and assuming the total bending stiffness is the sum of the bending stiffnesses of the individual wires [69]. Using the average diameter $d_{avg}$ and assuming the lay angle $\theta$ is small, the bending stiffness becomes

$$EI = E \sum \frac{\pi {d_w}^4}{64} cos\theta = E N_w \frac{\pi {d_{avg}}^4}{64} \tag{A23}$$

where $N_w$ is the number of wires. Based on the parameters listed in Table A1, the bending stiffness is estimated to be 0.73 Nm$^2$. Damping ratios for wire ropes

**Table A1:** Model parameters.

| | |
|---|---|
| Cable diameter, $d$ | 20 mm |
| Cable mass per unit length, $\mu$ | 1.38 kg/m |
| Damping ratio, $\xi$ | 0.10 |
| Cable tension, $T$ | 200 N |
| Cable elastic modulus, $E$ | 75.8 GPa |
| Cable bending stiffness, $EI$ | 0.73 Nm$^2$ |
| Cable metallic area, $A$ | $1.64 \times 10^{-4}$ m$^2$ |
| Sheave radius at root, $R$ | 0.18 m |
| Sheave groove angle | 30 degrees |

undergoing bending vary with cable tension and have been shown to be as high as 37% for slack cables [71]. A conservative damping ratio of 10% was used for the simulations.

The natural frequency of the catenary is estimated by treating the cable as a thin Euler-Bernoulli beam pinned at both ends and is given by [82]

$$\omega_n = \left(\frac{\pi}{L}\right)^2 \sqrt{\frac{EI}{m}\left[1 + \frac{T}{EI}\left(\frac{L}{\pi}\right)^2\right]} \tag{A24}$$

where $L$ is the beam length, $m$ is the mass per unit length, $T$ is the axial tension, and $EI$ is the bending stiffness. The vortex shedding frequency can be calculated using the Strouhal relation [77]:

$$f_{St} = \frac{StU}{d} = \frac{\omega_{St}}{2\pi} \tag{A25}$$

where $St$ is the Strouhal number, assumed to have a value of 0.2 [81], $U$ is the free stream velocity and $d$ is the cable diameter.

Simulations were performed for three cases; the model parameters specific to each case are given in Table A2. In each case, the wind velocity was chosen such that the

**Table A2:** VIV case study parameters.

| Case | 1 | 2 | 3 | 4 |
|---|---|---|---|---|
| Span length (m) | 2 | 5 | 5 | 5 |
| Cable Tension (N) | 200 | 200 | 500 | 1000 |
| Natural frequency (rad/s) | 19.9 | 7.57 | 12.0 | 16.9 |
| Wind velocity (m/s) | 0.302 | 0.121 | 0.190 | 0.269 |

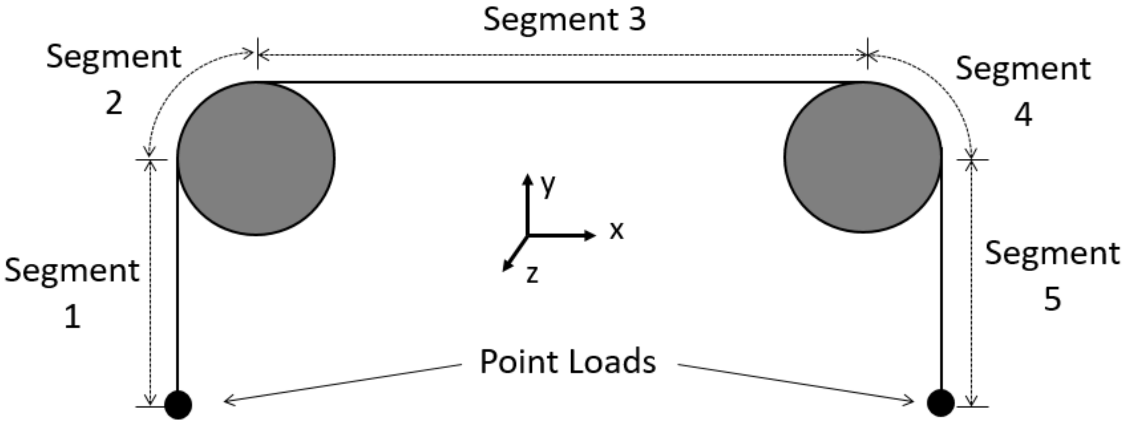

**Figure A2:** Diagram of cable-sheave system

shedding frequency matches the estimated natural frequency of the cable.

### Mesh Convergence

The cable was divided into five segments as shown in Fig. A2: the two free cable ends with point masses attached, the two segments in contact with the sheaves and the catenary suspended between the sheaves. The wind load is applied only to the catenary (segment 3). Each segment was further divided into elements. A smaller element length is desirable for the elements in contact with the sheave as the curvature is greater. A mesh convergence was performed by allowing the system to reach equilibrium with no wind load applied and iteratively reducing the length of the elements in the contact arc and comparing the contact force at the top of the sheave. The number of elements was found to have a minimal effect on the contact force.

For the segment 3, the convergence is determined by simulating 20 seconds of motion with the wind load applied. The maximum amplitudes of the motion at the mid-point of the span were compared. Convergence was considered to occur when the change in the output was less than 1%. The results are shown in Fig. A3. For the final simulations, 5 elements were used for each of the contact segments while 12 and 16 elements were used for the 2 and 5 m cable spans. The free cable ends were assumed not to undergo significant transverse motion, thus only 2 elements were used for each.

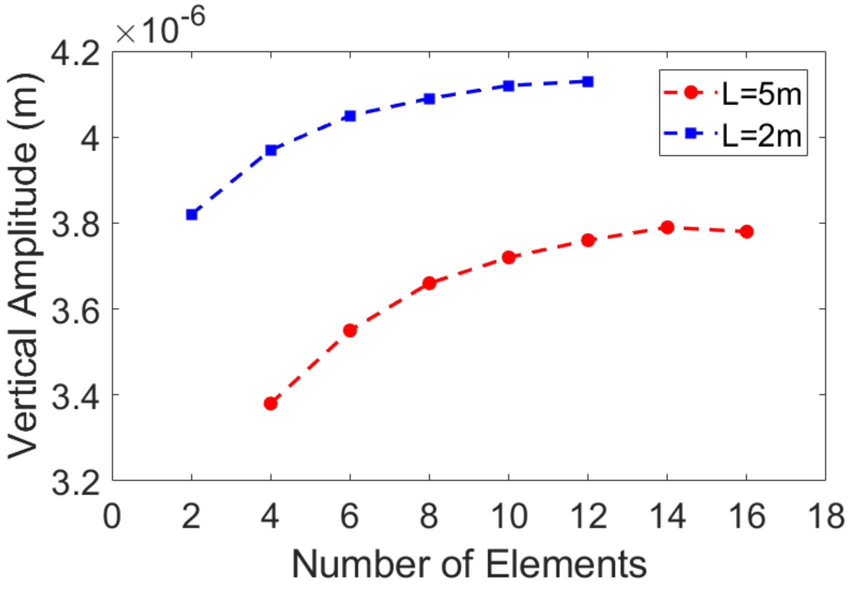

**Figure A3:** Convergence curves for segment 3

## Results

For each case in Table A2, the motion was simulated until a steady oscillation was obtained. Figure A4 displays the vertical motion at midpoint of the span the for Case 4. The results for each test case are shown in Table A3. The maximum amplitude at the midpoint of the span was $4.5 \times 10^{-6}$ for Case 4. At the sheave, the maximum amplitude was $3.3 \times 10^{-6}$.

**Table A3:** Simulated vibration amplitudes.

| Case | 1 | 2 | 3 | 4 |
|---|---|---|---|---|
| Vertical, Mid-span ($10^{-6}$ m) | 4.1 | 3.8 | 4.4 | 4.5 |
| Streamwise, Mid-span ($10^{-6}$ m) | 0.30 | 0.35 | 0.30 | 0.30 |
| Vertical, Sheave ($10^{-6}$ m) | 0.48 | 1.38 | 3.3 | 2.3 |

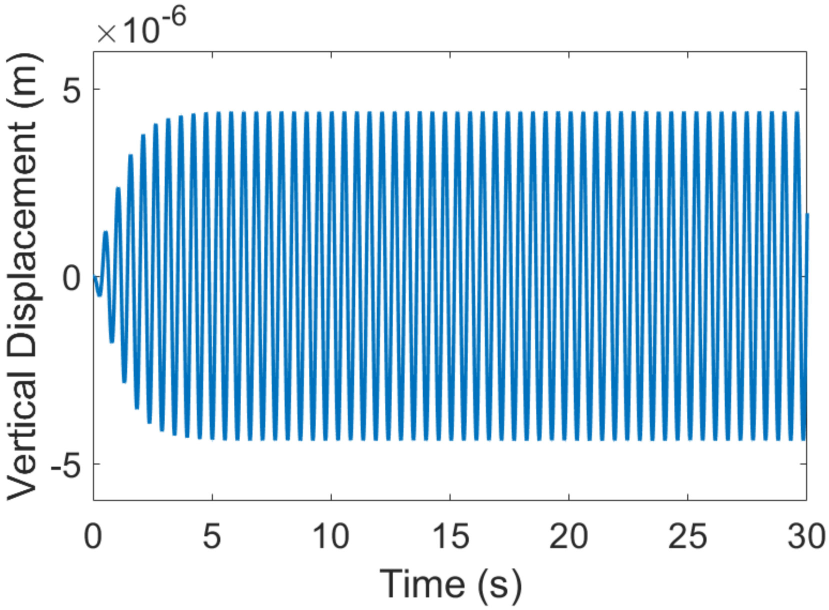

**Figure A4:** Mid-span vertical displacement for Case 4

## A.4 Conclusion

In this paper a dynamic finite element model of a low-tension cable sheave system was used to simulate the vortex-induced vibration of the cable due to wind loading and assess the potential for wind loading to lead to detachment of the cable from the sheave. The model, constructed using the absolute nodal coordinate formulation, utilized a wake-oscillator model to describe the vortex shedding forces. Also, three-dimensional contact with the sheave grooves was introduced. Several case studies were performed for systems of varying span length and cable tension with the wind velocity selected to excite the fundamental mode of the cable. The vibration amplitudes were determined to be small – the maximum amplitude observed at the sheave was only $3.3 \times 10^{-6}$ m – thus wind loading alone is unlikely to lead to cable detachment.

In future work, the wake-oscillator parameters can be tuned based on wind tunnel experiments. Scenarios where more severe vibrations are likely, such as cables with ice accretion, can also be examined in this manner. Also, the model could potentially be applied to a submerged cable system, in order to examine drag amplification effects due to VIV.